PATIENT-IMAGE REGISTRATION USING A-MODE ULTRASOUND LOCALIZATION OF FEATURES

By

Wayne Andrew Bass

Dissertation

Submitted to the Faculty of the
Graduate School of Vanderbilt University
in partial fulfillment of the requirements
for the degree of

DOCTOR OF PHILOSOPHY
in

Biomedical Engineering

May, 2003
Nashville, Tennessee

Approved By:

Professor Robert L. Galloway, Jr.

Professor J. Michael Fitzpatrick

Professor Benoit M. Dawant

Professor Cynthia B. Paschal

Professor Robert J. Maciunas

ACKNOWLEDGEMENTS

This dissertation could not have been completed without the generous assistance of many others. Chiefly among those is my adviser, Dr. Robert L. Galloway, Jr., who selflessly shared his time, knowledge, and resources. Dr. Bob's constant encouragement and support have been a source of strength throughout my tenure at Vanderbilt.

I sincerely thank Dr. J. Michael Fitzpatrick and Dr. Benoit M. Dawant for their assistance and suggestions that helped to improve the quality of this dissertation and Dr. Cynthia B. Paschal and Dr. Robert J. Maciunas for providing valuable advice and support. It was a privilege to learn from and work with each of my committee members.

The acquisition of clinical data would not have been possible without the support of the Departments of Neurological Surgery and Radiology and Radiological Sciences. In particular, Dr. Peter E. Konrad gave much of his limited free time and support. I thank Srikanth Gadamsetty for his help in the operating room and all the residents, nurses, and staff who graciously helped in so many ways.

It has been a pleasure to work with my fellow graduate students in the Snarl and Image Processing labs. Calvin Maurer, Georges Aboutanos, Jim Stefansic, Steve Hartmann, Dave Cash, Tuhin Sinha, and Mark Bray have all been gracious with their time and have each contributed to this dissertation.

TABLE OF CONTENTS

LIST OF TABLES

LIST OF FIGURES

CHAPTER 1

INTRODUCTION

Objective

Interactive, Image-Guided Surgery (IIGS) is the process by which tomographic images are used interactively to provide positional and guidance information to a surgeon in an effort to improve the surgical process without the use of a stereotactic frame. At the start of an operation three-dimensional images of the patient are mathematically overlaid onto the anatomy of the patient. Throughout the surgical procedure the surgeon uses a pointing device that transmits its position and orientation to the IIGS computer, which displays the pointing device's position on the tomographic images. The surgeon can then use the positional information displayed in the images combined with his/her direct visualization and anatomical knowledge to guide him/her to the surgical point(s) of interest.

The process of mathematically overlaying preoperative images onto the anatomy of the patient is also known as image space to physical space registration. The objective of this dissertation is to determine the accuracy with which point based and surface based image to physical space registration can be performed using a spatially tracked A-mode ultrasound transducer to localize features and the applicability of these techniques for general use in IIGS. For the case of point based registrations the ultrasound transducer will be used to localize subcutaneous bone-implanted fiducial markers. For the case of surface based registrations, ultrasound transducer will be used to localize the outer surface of the skull.

Specific Aims

The specific aims of this dissertation include:

To calibrate and test an A-mode ultrasound localization system. This localization system consists of a number of hardware components each with its own set of parameters and different modes of operation. The components will be integrated and configured to effectively and accurately localize registration features.

To develop signal processing algorithms for automatic detection and measurement of echoes arising from subcutaneous fiducial markers and echoes arising from the scalp/skull

interface in human subjects. There will be differences between the signal processing algorithms used to localize fiducial markers and the outer surface of the skull.

The comparison and analysis of differences in surface registration performance using two image segmentation algorithms. One of the algorithms is based on deformable models and the other based on voxel intensity. The effect of simplifying the surface generated from the intensity based algorithm will also be considered.

The determination of the effect, if any, that imaging resolution in the slice dimension has on the accuracy of the surface registration method. CT images used for neurosurgical procedures are generally acquired with 1 – 4 mm slice thicknesses. The difference in resolution may affect the resulting image model especially in areas of higher curvature.

The determination of the effect, if any, that different numbers of surface points have on surface registration accuracy.

CHAPTER II

BACKGROUND AND SIGNIFICANCE

Rigid Registration of Image Space and Physical Space

An important task in any image-guided surgery or image-guided therapy is to define a relationship between the patient and previously obtained images of the patient. In order to accomplish this task a coordinate system is assigned to the physical space occupied by the patient. Since the images of a patient have their own coordinate system, the task of aligning the images and the patient can be accomplished by determining a mathematical relationship between the image coordinate system and the patient coordinate system. This mathematical relationship between coordinate systems is referred to as a registration and the two coordinate systems are said to be registered with respect to each other. When the two coordinate systems both arise from images of the patient, the registration is referred to as an image-space to image-space registration, or more simply an image to image registration. When one of the coordinate systems represents the actual patient the registration is classified as an image space to physical space registration. Ideally a point defined in one coordinate system will map to the identical point defined in the other coordinate system, but in reality there is always some error associated with the relationship.

Registrations may be classified by the type of mathematical relationship, or coordinate transformation, used to map points from one coordinate system to the other. In general, coordinate transformations may be linear or non-linear. In this work the discussion of registrations is limited to image space to physical space registrations using a subset of linear coordinate transformations known as rigid body transformations. Non-rigid transformations have not been widely used in image space to physical space registration applications, but are valuable in some image to image registration applications. For an example of a non-rigid registration, the reader is referred to [1].

Numerous methods have been proposed to compute image space to physical space registrations (See [2-4] for good image registration review articles). In general all of the methods work by selecting one or more features that are visible in the image coordinate system and accessible on the patient. Once the features have been identified in both coordinate systems,

an algorithm is selected to match the features by minimizing a distance metric between corresponding features. The determination of feature correspondence, the exact definition of distance, and the distance metric itself are all dependent upon the individual algorithm. The goal of these algorithms is to find the best rigid body transformation approximation of the true registration. As an indication of the performance of the registration estimate most algorithms report a residual distance statistic or measurement. The meaning of this number in terms of actual registration accuracy varies from algorithm to algorithm, but if measurement error is similar across data sets on average lower residuals yield better registration estimates. In an effort to improve sharing of analysis across differing systems Jannin et al. [5] have encouraged the development and use of a common methodology and terminology for validation. A more thorough discussion of registration errors is given below.

The various features that have been proposed for use in image space to physical space registrations may be classified into two groups. One group uses point-like features that have exact corresponding pairs in image space and in physical space. This group will be referred to as the point-based methods group. The second group uses features that correspond in a global sense but do not reduce to pairs of points that are anatomically identical at a local level. This group will be referred to as the curve and surface methods group.

Point-based features may originate from either the specific anatomy of a patient or from external markers placed on the patient. Anatomic landmarks such as the nasion and the tragus have been used for registration [6]. And as long as the anatomic landmarks are visible in the diagnostic images no new images need to be acquired for registration purposes. However there are a number of disadvantages associated with this method. In general it is difficult to reduce anatomic structures into mathematical points consistently. Also, there are only a small number of anatomical structures that can be measured both precisely and non-invasively in the region of the head. Additionally, landmarks such as the tragi may move with respect to the areas of surgical interest when the patient is placed in a head holder during image acquisition resulting in increased registration error. These disadvantages have limited the use of anatomic landmarks in image space to physical space registration for neurosurgery.

Externally applied markers are an alternative to anatomic landmarks that overcome many of their disadvantages. These markers may have different shapes and sizes and can be attached to the patient by various methods. van den Elson [7] has designed V-shape markers which can

be applied to the skin of the patient. ISG technologies [8], and various others [9-29], have used radiopaque beads which are glued to the patient's scalp for image acquisition and marked with ink for physical space localization. Most external markers are designed so that they can be accurately localized in both physical space and image space. But skin attached markers still have the disadvantage of possible motion with respect to areas of surgical interest when the patient is placed in a head holder during image acquisition and during the surgical procedure. To avoid this unwanted motion Wang et al. [30] have used cylindrical markers that are attached to the outer tablature of the patient's skull. The disadvantage of this method is the requirement of a separate surgical procedure to attach the markers. A disadvantage of all external marker techniques that use non-permanent markers is the need for the markers to be applied prior to any image acquisition. This disadvantage would be largely reduced if permanently implanted subcutaneous markers [31] were utilized.

Point based registration algorithms may be applied to image to image registration applications and image space to physical space registration applications. The registration problem may be divided into translation and rotational components. The solution to the translation component is simply the vector between the centroids of the two point sets. The rotational component is the equivalent of the "Orthogonal Procrustes problem" [32, 33]. The earliest of these algorithms used in medical imaging were iterative in nature. They used multi-dimensional, nonlinear iterative techniques (e.g. steepest descent, Levenburg-Marquardt, Powell, etc.) [34] to minimize the Euclidean distances between corresponding points. Independently Schönemann [33] and Farrell and Stuelpnagel [35] published the first closed form solutions to this problem in 1966. In 1983 Golub and van Loan [36] rediscovered this solution and again in 1987 Arun et al. [37] rediscovered this solution. Both Golub and van Loan and Arun et al.'s solution uses an SVD-based approach. When the resulting transformation is applied to the first point set the mean squared Euclidean distance between the transformed points and the points in the second point set is minimized. This method has found wide use in the field of computer assisted surgery.

A second closed form registration method involving quaternions is attributed to Horn [38]. Although other methods for registering points sets using unit quaternions to represent rotations existed prior to Horn's work, they were either limited in the number of points they could match, or used an iterative technique to arrive at the solution. Similar to Schönemann,

Farrell and Stuelpnagel, Golub and van Loan, and Arun et al., Horn decomposes the transformation into rotation and translation and the solution for the translation component is the vector between the centroids of the two point sets. To calculate the rotation solution, Horn constructs a 4 x 4 matrix that contains arithmetic combinations of the sums of products of the two point sets. The rotational solution, in unit quaternion form, is given by the eigenvector corresponding to the most positive eigenvalue of this matrix. In 1991 Umeyama [39] rediscovered an improvement to Schönemann, Golub and van Loan, and Arun et al., and Horn's orthonormal matrix method [40] first published by Farell and Stuelpnagel that more robustly handles the situations where reflection matrices may arise.

The second group of features used for physical space registration is composed of curves and surfaces. Although continuous surfaces may be defined (for example with parametric equations), in the field of medical image registration surfaces they are predominantly constructed from discrete points. These points along with the interpolation method define the curve or surface. While the specific curve or surface (e.g. patient's scalp) may be the same in both image space and physical space, the underlying points that define the surface in image space are different than the points that define the surface in physical space. The differences in the points may arise from several conditions, including 1) one surface may be defined by a different number of points than the other, 2) one of the digitized surfaces may extend beyond the boundaries of the other digitized surface, or 3) one surface may have a greater point density than the other. Therefore, when the curves or surfaces are decomposed into points for purposes of registration these points do not have a one-to-one correspondence between image space and physical space. Curve and surface methods often use a large number of points to more accurately define the features. Additionally curves and surfaces with variations typically perform better than smooth surfaces or those with symmetrical or nearly symmetrical properties.

Whereas point-type landmarks are either anatomy based or externally applied, curve and surface features are almost always derived from the patient's anatomy. One surface commonly used for physical space registrations in neurosurgery is the surface of the patient's scalp. Unfortunately, this surface suffers from the same problem as skin attached markers. Namely, the patient's scalp is a deformable surface and will suffer local deformations when the patient is placed in a head holder during image acquisition or surgery.

Other anatomical structures used for surface based registrations include vertebral bodies and the femur and pelvis. Lavallee et al. [41] has used the outer surface of the vertebral body for physical space registration to guide pedical screw implantation in spinal neurosurgery. Simon et al. [42] has used the surfaces of the femur and pelvis for registration in total hip replacement surgery. Since all of these surfaces are rigid they are not susceptible to local deformations from fixation devices and the potential accuracy problems that accompany them.

Alternatively some research groups have used two- and three-dimensional curves for physical space registration. Balter et al. [43] has used curves and curve segments derived from projection images of the skull in order to perform registrations for radiation therapy. Two-dimensional curve segments are digitized on both portal and simulator films. Examples of curve segments include the inner table of the skull on lateral radiographs of the head, the apices of the lungs in an AP projection of the thorax, and a number of bony edges in the pelvis, shoulder and extremities [43]. The digitized curves are input into a curve fitting algorithm which computes a registration that is subsequently used to combine the simulator and portal images such that the radiation treatment plan and the isodensity contour(s) may be viewed in a common frame of reference.

Hamadeh et al. [44] has used curves of the vertebral bodies derived from projection radiography for registration in spinal surgery. After acquisition of CT images the vertebral bodies are segmented and, during surgery, a calibrated projection radiograph is taken. Curves and edges are automatically extracted from the radiograph and used with the segmented surface to compute the registration. The algorithm used to compute this registration is iterative and requires an accurate starting point which is typically supplied by first performing an anatomic point based registration.

Several algorithms are available to calculate the coordinate transformation between physical space and image space given the localized curve and surface features. In general these algorithms are equally applicable to image to image registrations, and in some cases the algorithms originated from image to image registration applications. Since surface-based registration applications often use a larger number of points than point based algorithms the number of distance computations can negatively affect the speed of the algorithm. Several methods exist for improving algorithm performance in this area including pre-computed distance maps and k-dimensional binary search trees. However, even with these additional methods,

surface based registration algorithms largely remain slower than point based algorithms. Additionally, all of the surface based algorithms commonly used are iterative in nature and require an initial transformation estimate to function.

Pelizarri and Chen [45] are credited with the first popular surface based image to image registration technique which they later applied to physical space registrations. The algorithm takes a set of points extracted from contours derived from a volumetric image (referred to as the "head" surface) and aligns these points with a second set of points (referred to as the "hat" points) acquired by sweeping a three dimensional localizer across the patient's scalp. Their algorithm seeks to minimize the mean squared distance between the hat points and the head surface. The distance between a hat point and the head surface is determined by projecting a ray from the hat point to the centroid of the head surface and calculating the distance between the hat point and the intersection of the ray and the head surface. The ray - head surface intersections are found using a derivation of the technique used by Siddon [46], and the transformation parameter search is based on Powell's [47] optimization algorithm.

Another surface fitting algorithm developed by Besl and McKay [48], the iterative closest point (ICP) algorithm, has gained popularity in the field of medical imaging. This algorithm takes a wide variety of input primitives including point sets, line segment sets, implicit curves, parametric curves, triangle sets, implicit surfaces, and parametric surfaces. Other representations may also be used provided that a procedure is available for evaluating the closest point on the surface to a given point. The algorithm requires that one of the surface representations be decomposed into a point set if it is not already in that form. This surface is hereafter referred to as the point set. The ICP algorithm is iterative in nature with each iteration of the algorithm proceeding as follows: Given an initial transformation, for each point in the point set the closet corresponding point on the surface model is found. A closed form point-based transformation is then applied between these closest points and the point set. In the final step of the iteration, the mean squared error is computed between the point set and the surface. The ICP algorithm may be terminated by various criteria including the number of iterations, if the change between iterations in the mean squared error is below a desired threshold, if the absolute error is below a desired threshold, etc.

An enhanced version of the ICP algorithm has been developed by Simon [49]. The enhancements are speed related and are designed to allow the algorithm to be used in a system

capable of tracking arbitrarily shaped objects at speeds of up to 10 Hz. The first of the four improvements is the use of k-dimensional binary search tree for calculating the closest triangle vertex on the surface representation to a given point in the data set. This improves the closest point search time from $O(N_P N_S)$ to $O(N_P \log N_S)$, where N_P is the number of points in the point set and N_S is the number of points in the surface representation. The second improvement involves caching of the N closest vertex points between iterations such that traversals of the k-dimensional binary search tree are not necessary for every iteration of the algorithm. The third speed improvement is a fast method for finding the surface point on the set of triangles that have a common vertex closest to a given point from the point set. And the fourth and final improvement is the decoupling of the algorithm acceleration. If the incremental transformations given by the algorithm are well aligned the current transformation may be scaled to improve convergence of the algorithm. While Besl and McKay [48] use a single scale factor, Simon decouples the transformation into separate translation and rotation components and uses separate scaling factors.

Lavallee's surface registration algorithm [41] starts with a 3D segmented surface from an image volume and uses either multiple 2D x-ray projection contours or 3D point data. To improve the speed of distance calculations Lavallee uses an octree-spline distance map. This representation increases memory space efficiency but still maintains detailed information near the surface. Starting with a standard octree based distance map they use a spline based interpolation technique to construct "a continuous 3D function that approximates the signed Euclidean distance to the surface"[41]. They define the signed Euclidean distance of a point as the minimum Euclidean distance between that point and the surface if the point is on the outside of the surface and the negative of that distance if the point lies on the inside of the surface. The registration algorithm makes use of the Levenburg-Marquardt [34] algorithm for the optimization of multidimensional nonlinear equations to drive the search for the transformational parameters. This search is terminated when the error is lower than a fixed threshold, when the difference between successive transformational parameters is below a fixed threshold, or when a maximum number of iterations have been reached. The only difference between using 3D point data and 2D projection contour data lies in the formulation of the error function.

Other registration algorithms can use both explicit point correspondences and surface representations for registration. Algorithms that use both types of features may either use them

simultaneously, or sequentially. Maurer et al. [50] described a method for the simultaneous use of surfaces and points. A weighting factor is used to control the contribution of each type of feature to the overall registration and an optimal weighting factor is derived based on clinical data. Their results suggest that point-like features should only contribute a small percentage of weight to the overall transformation to yield optimal results. The Elekta, formerly ISG Technologies, surgical navigation system has been described by a number of authors. And although different authors have reported different registration techniques with this device, frequently a two step registration algorithm is used. First, a point based registration is performed using externally applied skin markers. Then the system provides the option of refining this registration with additional surface points. If this option is selected the operator may then digitize a number of surface points. After the points have been acquired they are used in a surface fitting algorithm which refines the result of the point based registration.

In order to use any of the registration algorithms presented above the registration features need to be measured in both physical space and in image space. In physical space the measurement of features may be divided into two categories: direct digitization and measurement via a calibrated imaging device. Direct digitization methods use a mechanical, optical, electromagnetic, or sonic device capable of measuring the pose of a probe in three-dimensional space. Examples of such devices include the Faro articulated arm manufactured by Faro Inc., Orlando, Florida, the Optotrak 3020, Aurora, and Polaris systems manufactured by Nothern Digital Inc., Waterloo, Ontario, Canada, the 3SPACE Isotrak manufactured by Polhemus Navigation Sciences, Colchester, Vermont, and the Sonic Digitizing Wand by Striker Leibinger, Portage Michigan (formerly Picker International, Highland Hts., Ohio). For point based features direct digitization is often the simplest method of physical localization. For anatomical landmarks the probe is placed as close as possible to the landmark and the 3D location is recorded. For externally applied markers, the probe is placed at a specific point on or near the marker and the location is recorded. In some cases multiple measurements may be recorded to decrease the measurement error associated with the localizing device. Care must be taken to ensure that the point being digitized is exactly the same anatomical point that will be used in the image based measurement.

Direct digitization can also be used to collect surface information in order to perform surface based registrations. Typically this type of data collection is performed by sweeping the

digitizing probe across the surface of interest in a random fashion. The surgical software may provide visual or auditory feedback to indicate sampled point density and/or the degree of surface coverage or the user may have to estimate these quantities. The number of points to be collected depends on numerous factors including the speed of the digitization process, the complexity of the surface, and the requirements and performance of the registration algorithm. An alternative to random digitization is to follow a digitization plan. Simon [49] uses a constraint analysis algorithm which takes the image derived surface model and a hypothetical set of data collection points and generates a case specific sensitivity measure. Using this measure, a constraint synthesis algorithm generates a data collection plan which optimizes the accuracy of the registration.

One of the major disadvantages of direct digitization methods is the requirement that the point or surface feature used for registration be accessible to the digitization probe. This limits the number of anatomic points and surfaces that can be used for registration in neurosurgical applications. Direct digitization of large surfaces may also take a prohibitive amount of time. To circumvent these and other limitations, several research groups have proposed techniques using calibrated imaging devices to measure the location of registration features. In general, an imaging device is first internally calibrated to provide spatially accurate information. Then the device is modified so that the position and orientation of the device may be tracked in 3D space with a spatial digitizer. Finally the tracked imaging device is calibrated so that coordinates in the image may be related to the digitizer's 3D coordinate system.

Calibrated video cameras have been used by some research groups to acquire physical surface models. The VISLAN system [51] uses stereo video cameras combined with a structured light projector to localize the scalp and face of a patient. Corresponding points in the paired video images are automatically segmented, matched, and used to generate a series of 3D points on the surface of the patient's scalp and face. Gleason et al. [52] use a single video camera pointed at the patient from the surgeon's perspective. A video mixer then merges images from the video camera and a 3D reconstruction of the patient from a volumetric image. Both the patient's position and the relative position and orientation of the 3D reconstruction are adjusted until the images on the video monitor match.

Laser range scanners have also been used to directly acquire physical surface models for use in registration [53]. The scanner is used to collect a textured surface of the cortex which is

registered to a surface derived from MRI using a combination of shape-based methods [48] and intensity based methods [54].

Roberts et al. [55] and Pillay [20] have both used a calibrated operating microscope in order to localize fiducial markers. The position and orientation of the microscope are tracked by a sonic digitizer. The microscope has a fixed field of view and a very small depth of focus. A miniature CRT is attached to a modified beam splitter which allows an imaging computer to overlay graphics onto the video image. Fiducial markers are localized by positioning the microscope such that a marker is located at the center of computer generated cross hairs and in focus. Roberts et al. has discontinued the use of the operating microscope for fiducial marker localization in favor of a direct digitization method using a optical digitizer, although the graphic overlay in the microscope remains an integral part of their system.

Lavallee et al. [41] has used calibrated x-rays to localize vertebral bodies for spinal surgery. The x-ray imagers are carefully calibrated for distortion using an N-planes bicubic spline (NPBS) algorithm. A calibration cage is then used to determine the position and orientation of the x-ray units with respect to the digitizer's coordinate system. Points lying on the contours of the vertebrae shadows are interactively segmented in the x-ray images. These points are then used in a 3D/2D surface registration algorithm.

Schreiner et al. [56] have proposed to use a calibrated biplane x-ray system to localize implanted fiducial markers for delivery of radioactive pellets in liver cancer procedures. Radiopaque fiducial markers are implanted near the liver under ultrasound guidance. CT images are acquired with the markers in place. The biplane system is then used to localize the fiducials at the start of the procedure.

Lavallee et al. [41] has attached a digitization probe to a B-mode ultrasound transducer for percutaneous vertebral body surface localization. First the ultrasound images are acquired and stored. Afterwards the images are edited and interactively segmented to yield a set of 2D points. The digitization probe data are then used to convert the two dimensional points into a set of 3D points in the localizer's field of view suitable for registration.

Herring and Dawant [57] use a B-mode ultrasound transducer to acquire surface points from patches on vertebral bodies for use in an ICP surface registration algorithm. Their technique is capable of identifying the correct vertebrae based on surface registration results.

Maurer et al. [58] have independently pursued the use of a spatially tracked A-mode ultrasound transducer to localize the outer surface of the skull. The collected data points are registered to a CT derived surface using an ICP algorithm.

Segmentation is often a significant part of the measurement of registration features in image space. Segmentation algorithms may be manual or computer assisted and may be automatic or interactive. Research groups that have designed externally applied markers typically use either interactive or automatic segmentation algorithms designed specifically to localize their external markers. Wang et al. [30] has designed an automatic segmentation algorithm used to localize externally applied fiducial markers, and van den Elsen et al. [7] have designed an interactive segmentation algorithm to localize their externally applied fiducial markers. There is a large body of work in the field of anatomic feature segmentation. The reader is referred to Ayache et al. [59] for a review of segmentation as it applies to computer assisted surgery, and Aboutanos [60] for a detailed description of a deformable model segmentation method.

Interactive, Image-Guided Neurosurgery at Vanderbilt

For a typical Interactive, Image-Guided Surgery (IIGS) case at Vanderbilt, CT, MRI, and positron emission tomography (PET) images (if available) of the patient are acquired. These three imaging modalities each contain complementary information. The CT images provide superior information about the skull and bony structures, but have poor soft tissue specificity. The MR images have superior soft tissue specificity, but lack the spatial resolution of the CT images and suffer from intensity and geometric distortions caused by magnetic field inhomogeneities. PET images provide information about the metabolic activity of tissue but have lower spatial and intensity resolution. The IIGS system can correct image distortions in some types of MRI images caused by magnetic field inhomogeneities using an algorithm described in [61].

The Vanderbilt IIGS system currently uses rigid body transformations as mapping functions and implantable fiducial markers [30] as landmarks to calculate registrations. A fiducial marker unit consists of two parts and is pictured in Figure 2.1. The base, shown in the middle, is 13 mm in length and 3 mm in diameter. The bottom 3 mm of the base is threaded for anchoring into the outer table of the patient's skull. The top of the base is fitted with a machined

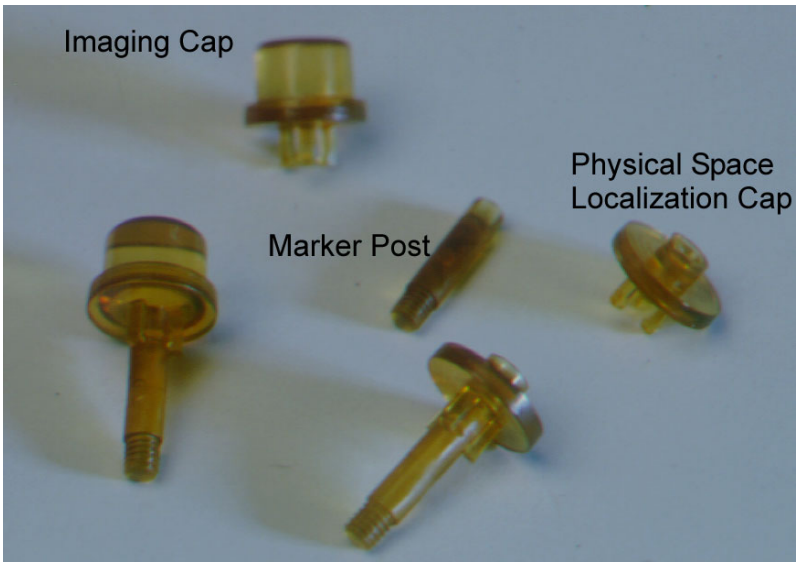

Figure 2.1 Fiducial Marker Components

keyhole with grooves to accept the mating portion of the other components. There are several types of markers that fit onto the base.

The tomographic imaging markers, in the upper left of the figure, are hollow plastic cylinders with an inside diameter of 7 mm and an inside height of 5 mm. For CT and MR imaging, they are filled with an aqueous solution of 165 mg/ml iothalamate meglumine and 0.5 mM gadopentetate dimeglumine and sealed. This solution is designed to be visible in CT and T1, T2, and proton density MR imaging [30]. Additional imaging markers are filled with a germanium solution for imaging in PET scanners. The imaging markers are snapped onto the bases (shown in the center portion of Figure 2.1) before imaging and can be removed afterwards. Fiducial markers can be used with almost any tomographic imaging modality provided that they are both visible and distinct.

In a typical IIGS case at Vanderbilt, after the tomographic images of a patient have been acquired they are transferred to the IIGS computer. The computer operator then interactively identifies the fiducial markers in the image volumes by placing a cursor within the interior of each marker and clicking a mouse button. The computer uses these seed points to identify the extents of the fiducial markers and calculate their geometric centers. The geometric center of a fiducial marker is called a fiducial point, or simply a fiducial and the process of calculating a fiducial from its marker is called fiducial localization. The fiducial localization algorithm used

by the IIGS system uses knowledge of the marker geometry and a dynamic threshold technique to segment the fiducial markers from the images. The centroids of the segmented markers are calculated using an intensity weighted algorithm and returned as the fiducial points [30]. Because of noise in the imaging system and the finite size of the image voxels, the fiducial points identified by the fiducial localization algorithm are subject to measurement error. We call the distance between the true location of the fiducials and the location given by the algorithm the fiducial localization error (FLE).

After image localization the computer operator interactively identifies the fiducial correspondences. The fiducial points and correspondences are input into the registration algorithm, which is based on the closed form, singular value decomposition (SVD)-based, point fitting routine described in [37]. As previously stated, this algorithm returns the rigid body transformation that minimizes the squared Euclidean distance between the first set of fiducials and the transformed second set of fiducials.

The Vanderbilt IIGS system currently uses the Optotrak/3020^{TM} real time three dimensional digitizer manufactured by Northern Digital Inc. [62]. The Optotrak uses 3 one dimensional CCD sensors to track the position of infra-red emitting diodes (IRED) in three dimensional space. Each of its sensors are mounted behind optical lenses that compress the two dimensional field of view into a one dimensional line focused on the respective CCDs. Therefore each of the sensors can independently localize an IRED to a plane in space. The three dimensional position of the IRED is then solved by computing the intersection of these three planes. Figure 2.2 shows a schematic representation of the Optotrak system.

In addition to tracking single IREDs the Optotrak system can also determine the position and orientation of objects constructed with multiple IREDs. Typically 6, 24, or 25 IREDs are attached to a rigid structure to build an object called a rigid body (two are shown in Figure 2.3). To determine the position and orientation of the rigid body the Optotrak first loads a table containing the position and orientation (measured in the rigid body's local coordinate system) of each of the IREDs. This step is performed only once as the system is being setup for operation. During the localization process the Optotrak sequentially activates the IREDs on the rigid body. Not all of the IREDs will be visible to the sensors every time for various reasons including: some of the IREDs will be oriented away from the sensors, some of the IREDs may be oriented towards the sensor, but out of one or more of the sensors' field of view, and some of the IREDs

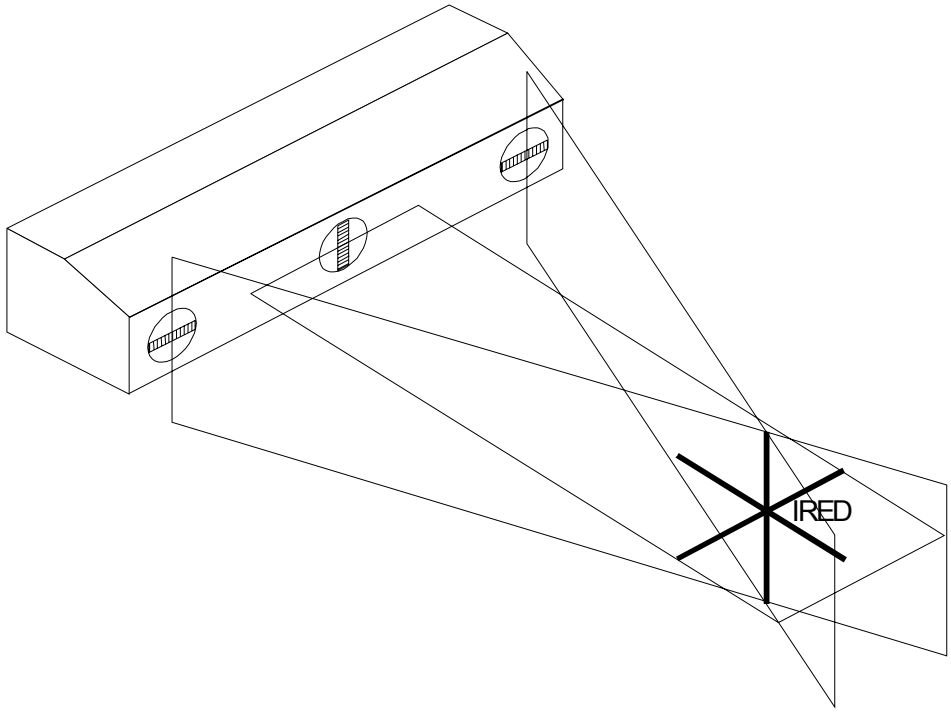

Figure 2.2 Optotrak Schematic

may be blocked by another object between the rigid body and sensors. Those IREDs that are successfully localized are matched against the table of rigid body IRED locations using a unit quaternion based registration algorithm. The result of this algorithm is the position and orientation of the rigid body in the Optotrak's coordinate system.

During surgery a rigid body is attached to the head fixation device. Hereafter this rigid body is referred to as the reference emitter. In addition to the reference emitter, the Optotrak may track one or more rigid bodies configured as surgical probes. The Optotrak reports the position and orientation (with respect to the sensor unit) of all of the surgical probe(s) and the reference emitter to the IIGS computer, updating the information 30 times per second. The computer transforms the location of the surgical probes into the reference emitter's frame of reference freeing the IIGS system from any dependency on the position of the Optotrak sensor unit. The sensor unit can therefore be moved around the operating room during the surgery as necessary. The Optotrak will continue to report information about the rigid bodies as long as the sensor unit maintains a line of sight with the reference emitter and the surgical probe(s).

Prior to the start of the surgical procedure, physical space markers, referred to as localization caps and seen in the left portion of Figure 2.1, are attached to the marker bases.

These "markers" are constructed from a solid plastic cylinder with a precision drilled hemispherical divot in the center. The divot is aligned such that its centroid is coincident with the centroid of the tomographic imaging marker. An Optotrak surgical probe with a precision machined spherical tip is placed in the divots to localize the fiducials as seen in Figure 2.3. An image to physical space registration is then calculated in the same manner as the image to image registrations. Just as the FLE in image space depends on the fiducial localization algorithm, the FLE in physical space depends on the performance of the Optotrak.

Analysis and Validation of IIGS Performance

The quality of the IIGS system is dependent on ease of use, the responsiveness of the system, the accuracy of the system, and the ability of the system to estimate its accuracy on a case by case basis. The responsiveness and ease of use of the system are achieved through careful integration of high performance hardware and software engineering. The accuracy of the system is determined in large part by the quality of the image to image and image to physical space registrations and the accuracy of the Optotrak.

The accuracy of a registration depends on the number of corresponding points used in its calculation and the FLE in both spaces. For the IIGS system fiducial localization algorithm the FLE is assumed to have a zero mean and the standard deviation has been experimentally determined to be 0.3 ~ 0.4 mm for the standard imaging protocols used at Vanderbilt [30]. The localization accuracy of the Optotrak for a single IRED aligned with the sensors is approximately 0.267 mm [63], however when these IREDs are configured as a rigid body the positional accuracy of localizing the rigid body has been experimentally determined to be 0.4 ~ 0.5 mm.

The fiducial registration error (FRE) is the root-mean square (RMS) statistic of the distance between the fiducials in one space and the fiducials in the second space transformed by the registration matrix. This number is a measure of the residual of the registration and is only an estimate of the registration performance. A true measure of the registration accuracy is the target registration error (TRE). This is the RMS statistic of the distance between the target points of the first space and the target points of the second space transformed by the registration matrix. If the FLE is uncorrelated, as the number of fiducials used to compute the registration increases, the FRE will approach the FLE and the TRE will decrease to zero [64]. Details on the distribution of TRE and its mathematical derivation can be found in Fitzpatrick and West [65].

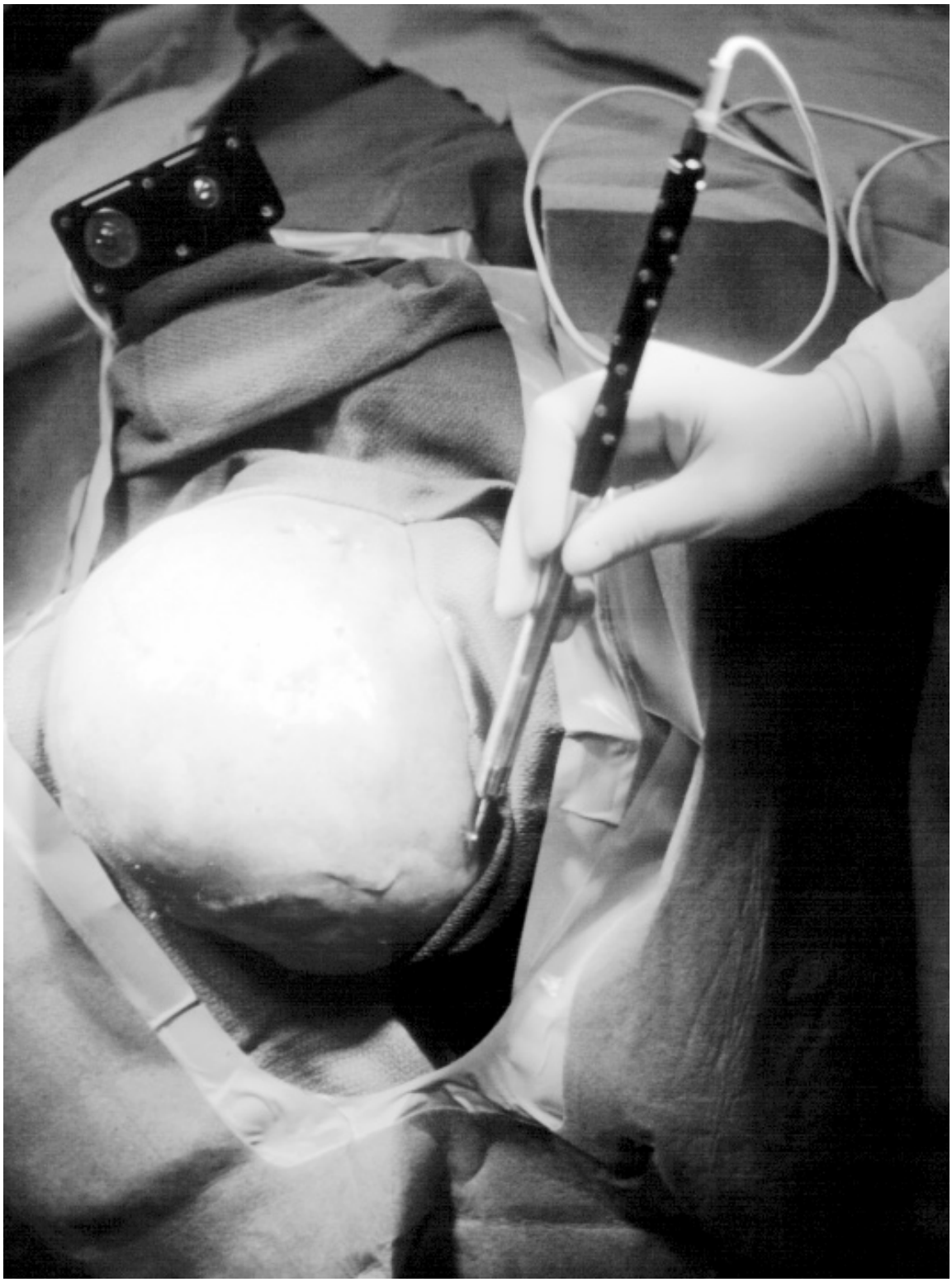

Figure 2.3 Fiducial Localization in the OR

The Vanderbilt IIGS system returns a FRE for every registration it performs. With an estimate of the FLE in both imaging and physical spaces and the number of fiducials used in the registration known, the FRE can be used as an indication of TRE and system accuracy. However it is not a true accuracy measure.

Significance of A-Mode Ultrasound Localization for Vanderbilt IIGS

There are a number of disadvantages associated with the use of fiducial markers. Fiducial markers require a separate surgical procedure to implant the marker posts in the patient's skull. This procedure must be performed prior to image acquisition. Therefore any images which were acquired prior to marker implantation cannot be incorporated into the system. Further, fiducial markers must be removed within 28 days of implantation limiting their use for tracking the progression of disease or courses of treatment longer than 28 days.

Permanently implantable fiducial markers [31] can minimize some of the disadvantages associated with the current fiducial markers. While they still require a separate surgical procedure to implant, after that procedure there is no pre-imaging preparation required for their use in any subsequent imaging study. Since these markers are subcutaneous and noninvasive direct digitization is not possible, A-mode ultrasound localization of these markers is required for integration into the IIGS system.

Further, localization of the outer surface of the skull with A-mode ultrasound for use in surface registration algorithms can alleviate some of the disadvantages associated with the use of any fiducial markers. A-mode ultrasound localization does not require a separate surgical procedure or any special setup procedures prior to image acquisition. Therefore any images that have been previously acquired, as long as they contain an overlapping field of view with the preoperative CT image, may be integrated into the system with an image to image registration algorithm. A-mode ultrasound localization may therefore provide an alternative to the fiducial marker system when the situation does not require the extreme level of accuracy provided by the current fiducial marker system.

References

[1] J. M. Galvin, K. Han, M. E. Noz, T. Vaccaro, J. Cooper, D. P. Reddy, and G. Q. Maguire, Jr., "Warping CT scans from nontreatment to treatment position," *Radiat Oncol Investig*, vol. 5, pp. 206-12, 1997.

[2] J. M. Fitzpatrick, D. L. G. Hill, and C. R. Maurer, Jr.. Image Registration. In: *Handbook of Medical Imaging, Volume 2: Medical Image Processing and Analysis*, eds. M Sonka and JM Fitzpatrick. Bellingham WA: SPIE Press, 2000. pp. 447-513.

[3] J. V. Hajnal, D. L. G Hill, and D. J. Hawkes. *Medical Image Registration*, CRC Press: 2001.

[4] J. B. A. Maintz and M. A. Viergever, "A survey of medical image registration", *Medical Image Analysis*, vol. 2, pp1-36, 1998.

[5] P. Jannin, J. M. Fitzpatrick, D. J. Hawkws, X. Pennec, R. Shahidl, M. W. Vannier, "Validation of medical image processing in image-guided therapy", *IEEE Transactions on Medical Imaging*, vol. 21, pp. 1445-1449, 2002.

[6] E. Watanabe, T. Watanabe, S. Manaka, Y. Mayanagi, and K. Takakura, "Three dimensional digitizer (neuronavigator): new equipment for computed tomography-guided stereotaxic surgery," *Surgical Neurology*, vol. 27, pp. 543-547, 1987.

[7] P. A. van den Elsen, "Multimodality Matching of Brain Images," in *Department of Radiology and Nuclear Medicine*. Utrecht, the Netherlands: Utrecht University, 1993, pp. 168.

[8] R. L. Carrau, C. H. Snyderman, H. B. Curtin, and J. L. Weissman, "Computer assisted frontal sinusotomy," *Otolaryngology*, vol. 111, pp. 727-732, 1994.

[9] B. K. Brodwater, D. W. Roberts, T. Nakajima, E. M. Friets, and J. W. Strohbehn, "Extracranial application of the frameless stereotactic operating microscope: experience with lumbar spine," *Neurosurgery*, vol. 32, pp. 209-213, 1993.

[10] R. D. Bucholz and K. R. Smith, "A comparison of Sonic Digitizers Versus Light Emitting Diode-Based Localization," in *Interactive Image-Guided Neurosurgery*, R. J. Maciunas, Ed.: AANS, 1993, pp. 179-200.

[11] W. Freysinger, A. R. Gunkel, A. Martin, R. J. Bale, M. Vogele, and W. F. Thumfart, "Advancing ear, nose, and throat computer-assisted surgery with the arm-based ISG viewing wand: the stereotactic suction tube," *Laryngoscope*, vol. 107, pp. 690-693, 1997.

[12] E. M. Friets, J. W. Strohbehn, J. F. Hatch, and D. W. Roberts, "A frameless stereotactic microscope for neurosurgery," *IEEE Transactions on Biomedical Engineering*, vol. 36, pp. 608-617, 1989.

[13] R. L. Galloway, Jr., R. J. Maciunas, and C. A. Edwards, "Interactive Image-Guided Neurosurgery," *IEEE Transactions on Biomedical Engineering*, vol. 39, pp. 1226-1231, 1992.

[14] J. G. Golfinos, B. C. Fitzpatrick, L. R. Smith, and R. F. Spetzler, "Clinical use of a frameless stereotactic arm: results of 325 cases," *Journal of Neurosurgery*, vol. 83, pp. 197-205, 1995.

[15] B. L. Guthrie and J. R. Adler, Jr., "Computer assisted preoperative planning, interactive surgery, and frameless stereotaxy," *Clinical Neurosurgery*, vol. 38, pp. 112-131, 1992.

[16] D. Haynor, A. W. Borning, B. A. Griffin, J. P. Jacky, I. J. Kalet, and W. P. Shuman, "Radiotherapy Planning: Direct Tumor Location on Simulation and Port Films Using CT," *Radiology*, vol. 158, pp. 537-540, 1986.

[17] M. P. Heilbrun, S. Koehler, P. McDonald, W. Peters, V. Sieminov, and C. Wiker, "Implementation of a machine vision method for stereotactic localization and guidance," in *Interactive Image-Guided Neurosurgery*, R. J. Maciunas, Ed.: AANS, 1993, pp. 169-177.

[18] H. Hirschberg, "Implementation of a stereotactic microscope using an optically coupled tracking system," *Stereotactic & Functional Neurosurgery*, vol. 66, pp. 96-101, 1996.

[19] A. Kato, T. Yoshimine, T. Hayakawa, Y. Tomita, T. Ikeda, M. Mitomo, K. Harada, and H. Mogami, "A frameless, armless navigation system for computer-assisted neurosurgery," *Journal of Neurosurgery*, vol. 74, pp. 845-849, 1991.

[20] J. Koivukangas, Y. Louhisalmi, J. Alakuijala, and J. Oikarinen, "Ultrasound controlled neuronavigator-guided brain surgery," *Journal of Neurosurgery*, vol. 79, pp. 36-42, 1993.

[21] Y. Kosugi, E. Watanabe, J. Goto, T. Watanabe, S. Yoshimoto, K. Takakura, and J. Ikebe, "An articulated neurosurgical navigation system using MRI and CT images," *IEEE Transactions on Biomedical Engineering*, vol. 35, pp. 147-152, 1988.

[22] S. Lavallee, "A New System for Computer Assisted Neurosurgery," *Proceedings of the Annual International Conference of the IEEE Engineering and Biology Society*, vol. 3, pp. 926-927, 1989.

[23] J. Oikarinen, J. Alakuijala, Y. Louhialmi, S. Sallinie, H. Helminen, and J. Koivukangas, "The Oulu Neuronavigator System: Intraoperative Ultrasonography in the Verification of Neurosurgical Localization and Visualization," in *Interactive Image-Guided Neurosurgery*, R. J. Maciunas, Ed.: AANS, 1993, pp. 233-246.

[24] P. K. Pillay, "Image-guided stereotactic neurosurgery with the multicoordinate manipulator microscope," *Surgical Neurology*, vol. 47, pp. 171-177, 1997.

[25] D. W. Roberts, J. W. Strohbehn, J. F. Hatch, W. Murray, and H. Kettenberger, "A frameless stereotaxic integration of computerized tomographic imaging and the operating microscope," *Journal of Neurosurgery*, vol. 65, pp. 545-549, 1986.

[26] G. Schlondorff, R. Moesges, and L. Klimek, “An articulated Localizing Arm for Otolaryngology,” in *Interactive Image-Guided Neurosurgery*, R. J. Maciunas, Ed.: AANS, 1993, pp. 149-157.

[27] T. Takizawa, S. Soto, A. Sanou, and Y. Murakami, “Frameless isocentric stereotactic laser beam guide for image-directed microsurgery,” *Acta Neurochirurgica*, vol. 125, pp. 177-180, 1993.

[28] A. Wagner, O. Ploder, G. Enislidis, M. Truppe, and R. Ewers, “Image-guided surgery,” *International Journal of Oral & Maxillofacial Surgery*, vol. 25, pp. 147-151, 1996.

[29] E. Watanabe, “The neuronavigator: A potentiometer-based localizing arm system,” in *Interactive Image-Guided Neurosurgery*, R. J. Maciunas, Ed.: AANS, 1993, pp. 135-147.

[30] M. Y. Wang, C. R. Maurer, Jr., J. M. Fitzpatrick, and R. J. Maciunas, “An Automatic Technique for Finding and Localizing Externally Attached Markers in CT and MR Volume Images of the Head,” *IEEE Transactions on Biomedical Engineering*, vol. 43, pp. 627-637, 1996.

[31] J. T. Lewis, R. L. Galloway, Jr., and S. Schreiner, "An Ultrasonic Approach to Localization of Fiducial Markers for Interactive, Image-Guided Neurosurgery--Part I: Principles," *IEEE Transactions on Biomedical Engineering*, vol. 45, pp. 620-630, 1998.

[32] J. R. Hurley and R. B. Cattell, “The procrustes program: Producing direct rotation to test a hypothesized factor structure,” *Behavioral Science*, vol. 7, pp. 258–262, 1962.

[33] P. H. Schönemann, “A generalized solution of the orthogonal procrustes problem,” *Psychometrika*, vol. 31, pp. 1–10, 1966.

[34] W. H. Press, B. P. Flannery, S. A. Teukolsky, and W. T. Vetterling, *Numerical Recipes in C: The Art of Scientific Computing*, Second Edition ed. New York, NY: Cambridge University Press, 1992.

[35] J. L. Farrell and J. C. Stuelpnagel, "Problem 65-1: A least squares estimate of satellite attitude," SIAM Reviews, vol. 8, pp. 384-386, 1966.

[36] G. Golub and C. van Loan, *Matrix Computations*. Baltimore, MD: Johns Hopkins Univ. Press, 1983.

[37] K. S. Arun, T. S. Huang, and S. D. Blostein, “Least-Squares Fitting of Two 3-D Point Sets,” *IEEE Transactions on Pattern Analysis and Machine Intelligence*, vol. 9, pp. 698-700, 1987.

[38] B. K. P. Horn, “Closed-form solution of absolute orientation using unit quaternions,” *Journal of the Optical Society of America. A.*, vol. 4, pp. 629-642, 1987.

[39] S. Umeyama, "Least-Squares Estimation of Transformation Parameters Between Two Point Patterns," *IEEE Transactions on Pattern Analysis and Machine Intelligence*, vol. 13, pp. 376-380, 1991.

[40] B. K. P. Horn, "Closed-form solution of absolute orientation using orthonormal matrices," *Journal of the Optical Society of America A.*, vol. 5, pp. 1127-1135, 1987.

[41] S. Lavallee, J. Troccaz, P. Sautot, B. Mazier, P. Cinquin, P. Merloz, and J. P. Chirossel, "Computer-Assisted Spinal Surgery Using Anatomy-Based Registration," in *Computer-Integrated Surgery: Technology and Clinical Applications*, R. H. Taylor, S. Lavallee, G. C. Burdea, and R. Mosges, Eds. Cambridge, Massachusetts: The MIT Press, 1996, pp. 425-449.

[42] D. A. Simon, B. Jaramaz, M. Blackwell, F. Morgan, A. M. DiGioia, E. Kischell, B. Colgan, and T. Kanade, "Development and Validation of a Navigational Guidance System for Acetabular Implant Placement," presented at CVRMed-MRCAS, Grenoble, France, 1997.

[43] J. M. Balter, C. A. Pelizzari, and G. T. Y. Chen, "Correlation of projection radiographs in radiation therapy using open curve segments and points," *Medical Physics*, vol. 19, pp. 329-334, 1992.

[44] A. Hamadeh, P. Sautot, S. Lavallee, and P. Cinquin, "Towards automatic registration between CT and X-ray images: cooperation between 3D/2D registration and 2D edge detection," presented at Medical Robotics and Computer Assisted Surgery, Baltimore, MD, 1995.

[45] C. Pelizzari, D. N. Levin, G. T. C. Chen, and C. T. Chen, "Image Registration Based on Anatomic Surface Matching," in *Interactive Image-Guided Neurosurgery*, R. J. Maciunas, Ed.: AANS, 1993, pp. 47-62.

[46] R. L. Siddon, "Prism representation: a 3D ray-tracing algorithm for radiotherapy applications," *Physics in Medicine and Biology*, vol. 30, pp. 817-824, 1985.

[47] M. J. D. Powell, "An efficient method for finding the minimum of a function of several variables without calculating derivatives," *The Computer Journal*, vol. 7, pp. 155-162, 1964.

[48] P. J. Besl and N. D. McKay, "A method for registration of 3D shapes," *IEEE Transactions on Pattern Analysis and Machine Intelligence*, vol. 14, pp. 239-256, 1992.

[49] D. A. Simon, "Fast and Accurate Shape-Based Registration," in *Robotics*. Pittsburgh, Pennslyvania: Carnegie Mellon University, 1996, pp. 196.

[50] C. R. Maurer, Jr. , G. B. Aboutanos, B. M. Dawant, R. J. Maciunas, and J. M. Fitzpatrick, "Registration of 3-D Images Using Weighted Geometrical Features," *IEEE Transactions on Medical Imaging*, vol. 15, pp. 836-849, 1996.

[51] A. C. F. Colchester, J. Zhao, N. Dorward, G. Subsol, and D. G. T. Thomas, "Comparison of Phantom Target Localisation by Frame-Based Stereotaxy and by the VISLAN System," presented at CVRMed-MRCAS, Grenoble, France, 1997.

[52] P. L. Gleason, R. Kikinis, D. Altobelli, W. Wells, E. Alexander, III, P. M. Black, and F. Jolesz, "Video registration virtual reality for nonlinkage stereotactic surgery," *Stereotactic & Functional Neurosurgery*, vol. 63, pp. 139-143, 1994.

[53] T. K. Sinha, D. M. Cash, R. J. Weil, R. L. Galloway, Jr., and M. I. Miga, "Cortical Surface Registration Using Texture Mapped Point Clouds and Mutual Information", *MICCAI 2002*, pp. 533-540, 2002.

[54] C. Studholme, D. L. G. Hill, and D. J. Hawkes, "An overlap invariant entropy measure of 3d medical image alignment," *Pattern Recognition*, vol. 32, pp. 71-86, 1999.

[55] D. W. Roberts, E. M. Friets, J. W. Strohbehn, and T. Nakajima, "The sonic digitizing microscope," in *Interactive Image-Guided Neurosurgery*, R. J. Maciunas, Ed.: AANS, 1993, pp. 105-111.

[56] S. Schreiner, J. H. Anderson, R. H. Taylor, J. Funda, A. Bzostek, and A. C. Barnes, "A System for Percutaneous Delivery of Treatment with a Fluoroscopically-Guided Robot," presented at CVRMed-MRCAS, Grenoble, France, 1997.

[57] J. L. Herring and B. M. Dawant, "Automatic Lumbar Vertebral Identification Using Surface-Based Registration," *Journal of Biomedical Informatics*, vol. 34, pp. 74-84, 2001.

[58] C. R. Maurer, Jr., R. P. Gaston, D. L. G. Hill, M. .J. Gleeson, M. G. Taylor, M. R. Fenlon, P. J. Edwards and D. J. Hawkes, "AcouStick: A Tracked A-Mode Ultrasonography System for Registration in Image-Guided Surgery", *MICCAI 1999*, pp. 953-962, 1999.

[59] N. Ayache, P. Cinquin, I. Cohen, L. Cohen, F. Leitner, and O. Monga, "Segmentation of Complex Three-Dimensional Medical Objects: A Challenge and a Requirement for Computer-Assisted Surgery Planning and Performance," in *Computer-Integrated Surgery: Technology and Clinical Applications*, R. H. Taylor, S. Lavallee, G. Burdea, C., and R. Mosges, Eds. Cambridge, Massachusetts: The MIT Press, 1996, pp. 59-74.

[60] G. B. Aboutanos, "Image-Based Deformable Models for 3-D Automatic Segmentation of the Brain," in *Department of Electrical Engineering*. Nashville, TN: Vanderbilt University, 1996, pp. 88.

[61] H. Chang and J. M. Fitzpatrick, "A Technique for Accurate Magnetic Resonance Imaging in the Presence of Field Inhomogeneities," *IEEE Transactions on Medical Imaging*, vol. 11, pp. 319-329, 1992.

[62] R. L. Galloway, Jr., R. J. Maciunas, W. A. Bass, and W. J. Carpini, "Optical localization for interactive, image-guided neurosurgery," *Medical Imaging*, vol. 2164, pp. 137-145, 1994.

[63] Quantum Inspection and Testing Limited, "Calibration Certificate," , Burlington, Ontario, Canada 1994.

[64] C. R. Maurer, Jr., J. M. Fitzpatrick, M. Y. Wang, and R. J. Maciunas, "Estimation of Localization Accuracy for Markers in Multimodal Volume Images," *Proceedings of the 15th Annual International Conference of the IEEE Engineering in Medicine and Biology Society*, pp. 124-125, 1993.

[65] J. M. Fitzpatrick and J. B. West, "The distribution of Target Registration Error in Rigid-Body Point-Based Registration," *IEEE Transactions on Medical Imaging*, vol. 20, pp. 917-927, 2001.

CHAPTER III

AN ULTRASONIC APPROACH TO LOCALIZATION OF FIDUCIAL MARKERS FOR INTERACTIVE, IMAGE-GUIDED NEUROSURGERY—PART II: IMPLEMENTATION AND AUTOMATION

Steven Schreiner[1], Robert L. Galloway, Jr.[2,3], Judith Thomas Lewis, Wayne Andrew Bass[2], and Diane M. Muratore[1]

[1]Department of Biomedical Engineering, Western New England College
[2]Department of Biomedical Engineering, Vanderbilt University
[3]Department of Neurological Surgery, Vanderbilt University

IEEE Transactions on Biomedical Engineering,
Vol. 45, No. 5, pp.631-641, May 1998.

Abstract

Registration of image space and physical space lies at the heart of any interactive, image-guided neurosurgery system. This paper, in conjunction with the previous companion paper [1], describes a localization technique that enables bone-implanted fiducial markers to be used for the registration of these spaces. The nature of these subcutaneous markers allows for their long-term use for registration which is desirable for surgical follow-up, monitoring of therapy efficacy, and performing fractionated stereotactic radiosurgery. The major challenge to using implanted markers is determining the location of the markers in physical space after implantation. The A-mode ultrasonic technique described here is capable of determining the three-dimensional (3-D) location of implanted cylindrical markers with diameter of 3.7 mm and 3 mm length.

Accuracy tests were conducted on a phantom representing a human head. The accuracy of the system was characterized by comparing the location of a marker analogue as determined with an optically tracked pointer and the location as determined with the ultrasonic localization. Analyzing the phantom in several orientations revealed a mean system accuracy of 0.5 mm with a +/- 0.1-mm 95% confidence interval. These tests indicate that transcutaneous localization of implanted fiducial markers is possible with a high degree of accuracy.

Index Terms—A-mode ultrasound, computer-assisted surgery, detection and localization, fiducial markers, image-guided surgery, registration, stereotactic neurosurgery, ultrasound.

Introduction

A companion paper [1] describes earlier work on an ultrasonic detection and localization scheme used for finding small, skull-implanted fiducial markers for frame-less, stereotactic neurosurgery. The companion paper reports promising experimental results indicating that A-mode ultrasound is capable of providing robust detection and localization with a high degree of accuracy. A detailed discussion of the neurosurgical application is presented there as well as the motivation for using implanted fiducial markers.

This paper describes how we extended these initial results into an automatic, clinically relevant system. Additionally, this paper discusses recent advances in the interactive, image-guided (IIG) neurosurgical system under development at Vanderbilt University (Nashville, TN).

As described in the companion paper, interactive, image-guided (IIG) neurosurgery [1]–[5] uses a rigid-body transformation to bring the physical space of the patient during surgery into registration with previously obtained medical images of that patient. The IIG system under development at Vanderbilt University displays the position of a pointer on images acquired preoperatively [computed tomography (CT), magnetic resonance imaging (MRI), magnetic resonance angiography (MRA) or positron emission tomography (PET)] or acquired in real-time (intraoperative ultrasound or video endoscopy) [2], [5]–[9]. The pointer can be attached to either an articulated arm [10], [11] or to an optically tracked probe [OPTOTRAK® System (Northern Digital Inc., Waterloo, Ont., Canada)]. This guidance information greatly enhances the surgeon's ability to navigate during surgical procedures, to preoperatively plan trajectories, and to minimize the craniotomy size.

Corresponding points in the preoperative images and on the patient are used to register physical space and image space. The key to point-based space registration methods is that the points are visible in the images and in physical space. Normally, point matching methods of registration [12], [13] rely either on intrinsic points [3], [9], which can be part of the patient's anatomy, or on extrinsic points [14], [15], which consist of markers introduced into the image and physical spaces (e.g., points on a stereotactic frame [16]).

Currently, the IIG system at Vanderbilt University uses temporary extrinsic fiducial markers that are rigidly attached to the patient's skull by threaded posts [17]. The markers snap onto the posts and are exterior to the patient. By attaching the markers in this way, the need for a stereotactic frame is alleviated and possible errors from motion of the markers between the time of the preoperative scans and the operation are minimized. Once a patient is positioned for surgery, the markers are touched by the pointing device while the location of the pointer's tip is recorded. The positions of the fiducial markers in physical space (e.g., relative to the pointer's coordinate system) are then known. Preoperatively, the location of these image-visible markers in the digitized image sets is found. Using the corresponding points in the images and in physical space, a rigid transformation is then calculated which brings the images into registration with the patient's current position. The surgeon may then use the pointer to touch sites of interest in the surgical field of the patient and to view the corresponding location of the pointer on the medical images.

Significant advantages associated with the long-term use of fiducial markers include using registration for surgical follow-up, monitoring of therapy efficacy, and performing fractionated stereotactic radiosurgery. All the registration techniques to date use temporary markers and assume a short duration between the acquisition of the images and the surgical process. Long-term use of intrinsic fiducials is not desirable because physical changes in the patient's anatomy due to a disease process, therapy, or aging may occur and affect the accuracy of the registration over time. Moreover, currently used extrinsic fiducials are also not desirable for long-term use because they are usually attached to the patient in such a way that they are not comfortable for the patient (e.g., stereotactic frames) or can be lost (e.g., detached from the patient's scalp).

In order to achieve and maintain accurate registration over longer periods of time, we propose a system of extrinsic fiducial markers that are implanted into the skull under the scalp. It is a nontrivial problem to locate such markers in physical space because they cannot be touched with the pointing device. An ultrasonic detection and localization scheme for accurate transcutaneous marker localization has been described previously [1], [18]–[20]. However, challenges remain in order to provide three-dimensional (3-D) localization under minimal constraints, including: providing complete automation of the localization algorithms, lifting constraints imposed upon the ultrasonic probe's orientation relative to the orientation of the marker, and ensuring a robustness that will enable the system to be used in a clinical environment.

This paper describes accuracy and precision studies of an automatic, clinically applicable, ultrasonic detection and localization system. The objective of these studies is to compare the accuracy of the ultrasonic localization system to the accuracy of the currently used OPTOTRAK pointer. The physical system and the automatic computer algorithm is discussed, followed by a description of accuracy and precision experiments.

Materials and Methods

A. Ultrasonic Transducer

The data presented in this paper were obtained using a Panametrics (model V312) 10-MHz, 6.35-mm diameter, single-crystal transducer with a 13 mm focal length in water; this

transducer was spherically focused and was highly damped to improve the axial resolution. The ultrasonic pulse was initiated and received by a KB-AEROTECH multiscanner which was connected to a 486, 33-MHz computer. The ultrasonic signal was sampled at 100 MHz using a high-speed, analog-to-digital conversion board (CS250, Gage Applied Sciences, Inc., Montreal, P.Q., Canada). The duration of each acquired signal was approximately 41μs (4096 samples).

B. OPTOTRAK Localization Device

The OPTOTRAK system (model 3020) is a localization system consisting of three infrared sensors that track the position of many infrared, light-emitting diodes (IRED's). The system is capable of finding the location of a single IRED in space with an rms accuracy of 0.1 mm. Each sensor consists of a cylindrical lens that focuses the incoming infrared light onto a linear array of 2048 charge-coupled devices (CCD's). The IRED's are strobed such that the sensors only detect one active IRED in the field of view at any given instant. Triangulation is used to find the 3-D location of each IRED relative to the sensor unit's position.

An object with several IRED's attached is termed a *rigid body*. Once a rigid body is known by the system (i.e., the relative positions of the IRED's are known), it can be tracked as a single entity and can itself serve as a reference coordinate system. Typically, in the neurosurgical application, there is a reference rigid body attached to a Mayfield head clamp (Ohio Medical Instruments, Cincinnati, OH.) that is firmly attached to the patient's head. This reference rigid body contains six IRED's arranged in a plane and serves as the "world" coordinate system. If any motion of the head occurs, the reference rigid body also moves and registration is preserved. Additional rigid bodies used in a surgery include several instruments that are fitted with handles. Each handle typically contains a set of 24 or more IRED's that make up a rigid body. The IRED's are distributed around the handle to increase the visibility of the probe to the sensors. Mathematically, three of the IRED's need to be visible to the sensors for identification of the rigid body's position in space. However, to increase robustness of the system, this application requires that a minimum of four IRED's on each rigid body are visible to the sensors. The surgical instruments are localized relative to the reference rigid body. The position of any point on or proximal to the handled instrument can be tracked. In addition, the pitch and roll of the handle are determined.

In this study, three rigid bodies (55 IRED's) were tracked at a rate of 40 Hz. The rigid bodies included the reference rigid body, a pointer attached to a handle, and an ultrasonic transducer attached to another handle. The pointer tip had a 1-mm sphere attached, the center of which served as the origin of the pointer rigid body and its position was reported by the OPTOTRAK system. The pointer's handle contained 24 IRED's while the ultrasonic probe's handle contained 25 IRED's. The number of IRED's was determined by the handle design; no functional difference existed between the two handles.

C. Calibration

The OPTOTRAK pointer probes were calibrated to find the position of the probe tip relative to the IRED's. The spherical tip of the probe was placed into a divot that exactly fits the tip and the probe was "pivoted" so that the infrared sensors could see the probe in many orientations while the center of the spherical tip of the probe remained stationary [Figure 3.1(a)]. After pivoting, the position of the probe tip relative to the IRED's in the handle was determined by the OPTOTRAK software [21]. Every time a probe tip was changed a new calibration was performed so that the new relationship between the probe tip and the IRED's could be found. The calibration of the ultrasonic probe was more complicated than the calibration of the pointer because there was no spherical tip on the ultrasonic probe for pivoting.

The aim of the ultrasonic probe calibration procedure was twofold: 1) to provide a pivot-point for a normal OPTOTRAK calibration of the probe and 2) to provide an origin of the ultrasonic signal that corresponded to this pivot-point. The pivot-point was provided by replacing the ultrasonic transducer with an adjustable length pointer with a spherical tip similar to that used in a normal OPTOTRAK calibration. With the aid of a custom fixture with a built-in micrometer, the pivot-point was carefully positioned so that it lay at the center of the ultrasonic probe face prior to its removal. With this fixture, it was possible to repeatedly exchange a pointer tip for the ultrasonic transducer so that a normal OPTOTRAK calibration could be performed. The calibration proceeded as follows [see Figure 3.1(b)]: The ultrasonic probe was held firmly in the fixture. The micrometer was moved so that it was flush with the probe-face plane. The micrometer was then backed-off by the radius of the spherical tip of the pointer probe (0.5 mm). The ultrasonic transducer was removed from the probe handle and replaced by an adjustable length pointer tip. This tip was positioned so that it touched the micrometer; this

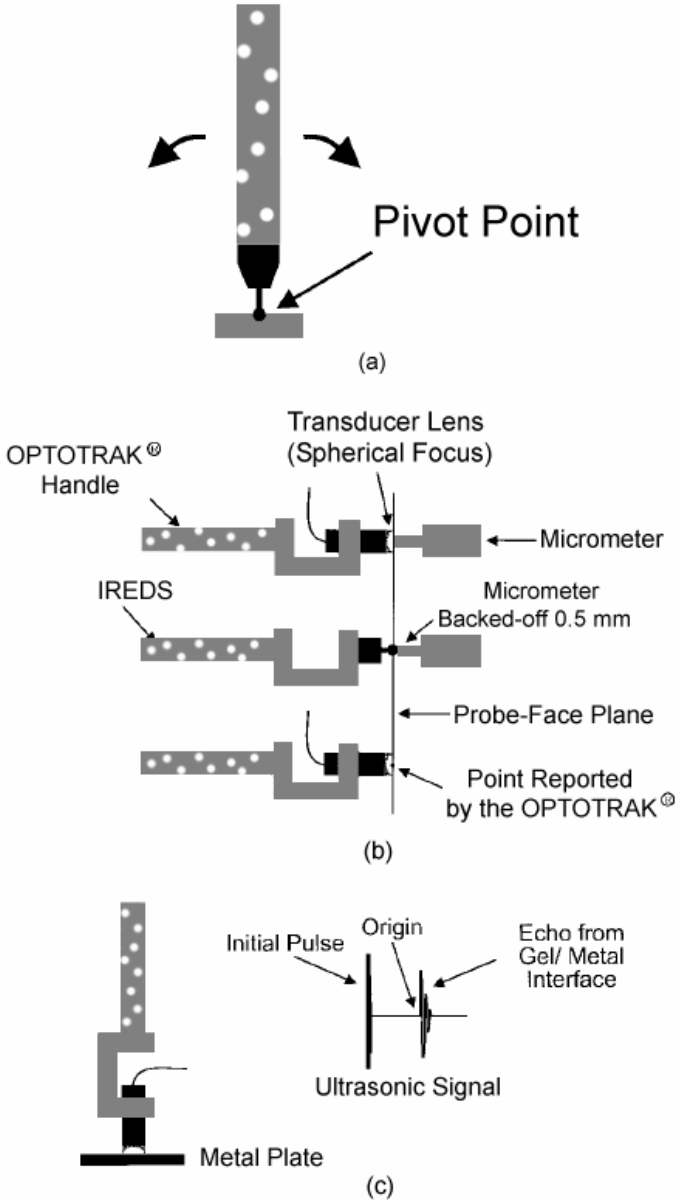

Figure. 3.1. The procedures used to calibrate the pointer probe and the ultrasonic probe. (a) The normal OPTOTRAK calibration procedure in which a pointer probe is "pivoted" while the center of the spherical pointer tip does not move. This allows the OPTOTRAK to determine the pointer tip location relative to the IRED's. During normal operation, the center of the pointer tip is reported as the probe position. (b) The ultrasonic probe alignment procedure. While the probe is firmly held in a fixture, the micrometer is moved to be flush with the probe-face plane. The ultrasonic transducer is then replaced by a pointer probe. The center of the spherical pointer tip is aligned with the probe-face plane by backing-off the micrometer by the radius of the sphere. The probe can then be calibrated using a normal OPTOTRAK calibration as in (a). (c) The procedure for determining the ultrasonic signal origin relative to the probe-face plane. The large gel/metal echo occurs at the probe-face plane; the beginning of this echo serves as the origin of the ultrasonic signal for calculating the physical position of echoes relative to the position of the probe.

aligned the center of the spherical tip with the probe-face plane. The modified ultrasonic probe was then "pivoted" as with a normal OPTOTRAK calibration. The pointer tip was then replaced with the ultrasonic transducer and the fixture was used to verify that the transducer was in its original position. The first part of the calibration procedure was completed and the OPTOTRAK was then capable of reporting the position ultrasonic probe (the center of the face of the probe).

The position of the ultrasonic probe reported by the OPTOTRAK was correlated with the ultrasonic signal so that we could calculate the physical depth of echoes relative to the probe position. Recall that the ultrasonic transducer was spherically focused; this resulted in a concave surface for the probe face. This concave space was filled ultrasonic coupling gel and the probe was placed flush against a metal surface. A large echo was returned from the coupling-gel/metal-surface interface [Figure 3.1(c)]. The position of this echo served as the origin of the ultrasonic signal for depth calculations because this interface was coincident with the probe-face plane and thus the OPTOTRAK calibration point. The ultrasonic probe calibration was then complete.

D. Phantom Design

Accuracy tests were performed using a phantom representing a human head. The phantom consisted of two components: the skull and the scalp (Figure 3.2). Each component

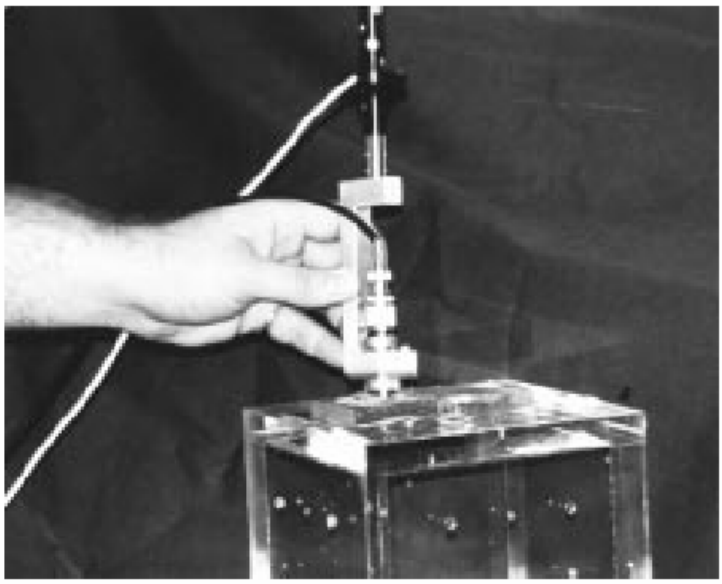

Figure 3.2. The ultrasonic probe and head phantom are shown.

was chosen for its acoustic characteristics. The skull was represented by a hard acrylic cube that had high acoustic impedance. The cube was hollow and was constructed from six acrylic plates. The scalp was made from a fat-mimicking layer of polyethylene; the speed of sound in this material was approximately 1490 m/s. Informal studies using healthy volunteers indicate that human scalp thickness ranges from a minimum of 2 mm to a maximum of 10 mm between people depending upon a person's weight and build. A 10-mm-thick layer of polyethylene was chosen for these studies and represented the maximum expected thicknesses.

E. Marker Analogue Design

Currently under development, the final design of the markers will be determined in part by the detection system described here. Ultrasonic principles state that the power reflected at the interface between two materials is dependent on the difference between the characteristic acoustic impedances of the two materials [22]. The final marker will be a fluid-filled cylinder; this fluid will be visible in CT and MRI images. The top of the marker casing will have a characteristic acoustic impedance closely matched with that of skin or fat (approximately 1.38 X 10^6 Rayls) [22] and the rest of the marker casing (including the bottom) will have a higher characteristic acoustic impedance than that of the skull (e.g., greater than about 5.4 X 10^6 Rayls) [22] (Figure 3.3). With this design, most of the power in the ultrasonic signal will pass through the top of the marker and reach the bottom at which point most of the power will be reflected back toward the ultrasonic transducer where it will be detected. An alternate design where both the top and bottom of the marker casing contained large acoustical impedance differences at their interfaces was considered, however, it was rejected due to the potential for reverberation artifacts in the ultrasound signal and the desire to maximize the power of the echo resulting from the bottom casing.

For the system accuracy studies described in this paper, the fiducial markers were modeled with gel-filled divots drilled into the acrylic "skull" phantom; these divots are termed *marker analogues* throughout this paper. Ultrasonic transmission gel was used to fill the divots. The divots were cylindrical with a diameter of 3.7 mm and a depth of 3.0 mm. The bottom surface of each divot was carefully machined and was considered to be flat; this surface is termed *marker-bottom* throughout this paper. The machining tolerance is 0.05 mm.

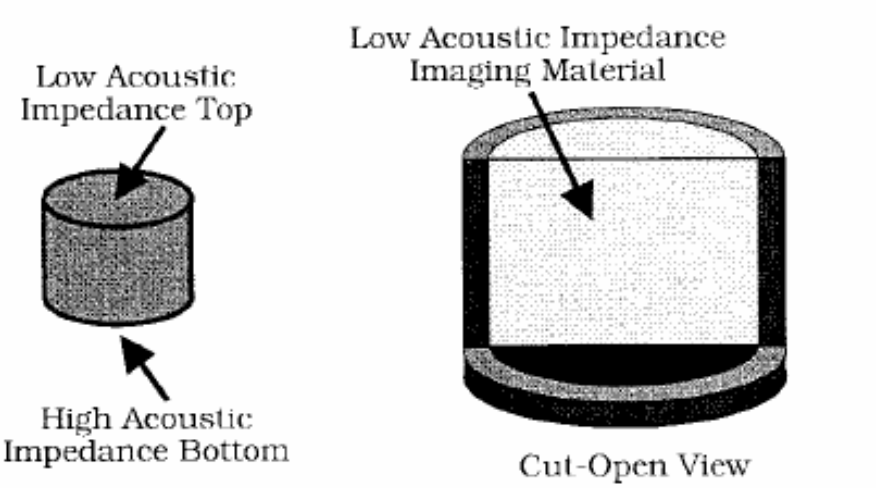

Figure 3.3. The ultrasonic localization system finds fiducial markers of this design. The top surface and interior imaging material have a similar acoustic impedance as the scalp. The bottom of the marker has an acoustic impedance more like bone.

Figure 3.4 shows three ultrasonic signals acquired with the transducer in contact with: a normal, healthy human head, the head phantom, and the head phantom over a marker analogue. Notice that the scalp/skull echo obtained from the human head [Figure 3.4(a)] is similar (by visual inspection in terms of duration and amplitude) to the polyethylene/acrylic (poly/acrylic) echo returned from the phantom [Figure 3.4(b)]. The polyethylene layer is thicker than the scalp, causing the poly/acrylic echo to occur later than the scalp/skull echo. Notice a small acrylic/air echo beyond the poly/acrylic echo in Figure 3.4(b); this echo results from the interface of the underside of the acrylic plate with the hollow interior of the cube. This acrylic/air echo has little power and is ignored by the detection algorithm. When the ultrasonic transducer is over the marker analogue [Figure 3.4(c)], a large echo is received from the ultrasonic-coupling-gel/marker-bottom (gel/bottom) interface. A small echo is present in this signal at the interface of the polyethylene layer and the gel inside the marker analogue (poly/gel). The poly/acrylic interface may also contribute to this echo due to the intersection of the ultrasonic beam with the edge of the marker analogue.

The objective of these studies was to compare the accuracy of the described ultrasonic detection system to that of the OPTOTRAK pointer. Additional features were added to the head phantom to enable accurate and precise localization of the marker analogue with the

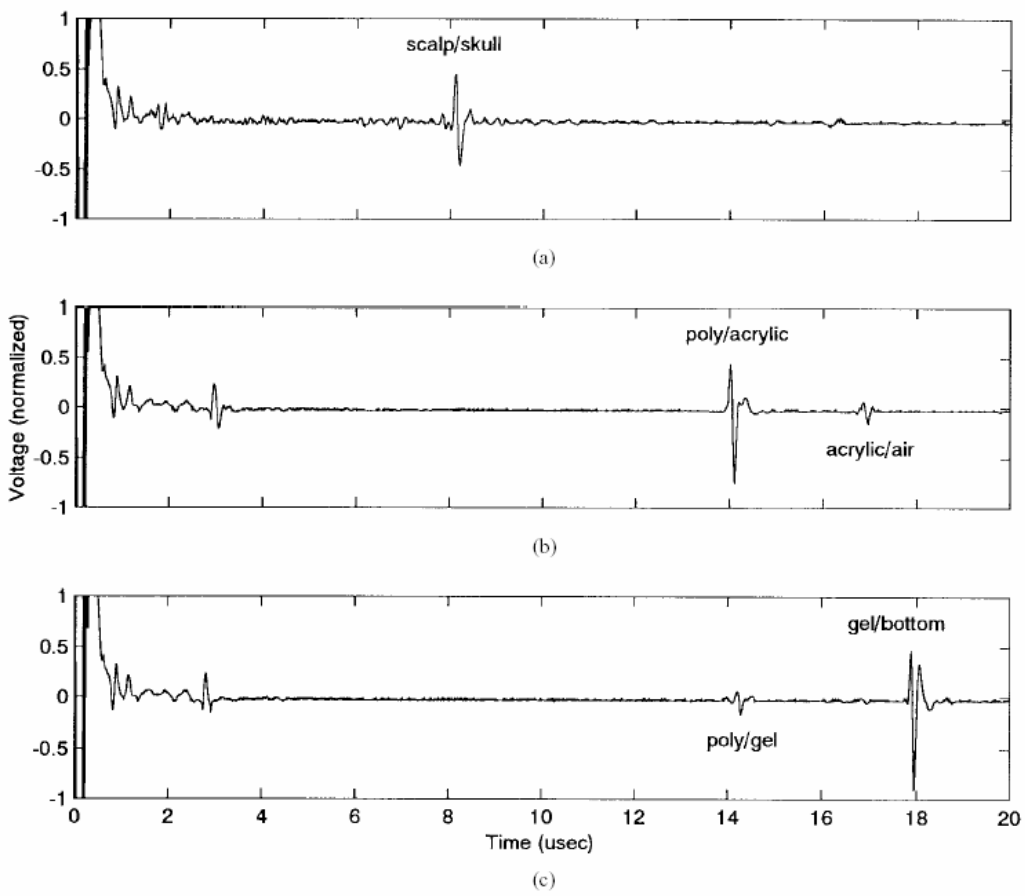

Figure 3.4. Three ultrasonic signals, (a) the signal returned when the ultrasonic probe is placed in contact with the author's head, (b) the signal returned from the phantom, and (c) the lower plot shows the signal returned from the phantom when the ultrasonic probe is held over a marker analogue.

OPTOTRAK pointer. Each marker analogue was straddled by a pair of "localization cups" containing spherical divots. The two hemispherical divots and the center of the marker analogue were collinear (Figure 3.5). The pointing probe used with the OPTOTRAK system had a 1-mm diameter spherical ball on its end that exactly fit into these divots. By inserting the probe into the spherical divots on either side of the marker, their locations relative to the reference rigid body were found. The center of the marker then lay on the center of the line segment joining these two spherical divots. This indirect method of localization was then compared with the localization provided by the ultrasonic system. Notice that this scheme can be applied to any type of marker as it is developed and tested; this scheme is desirable because the center of a closed, fluid-filled marker cannot be "touched."

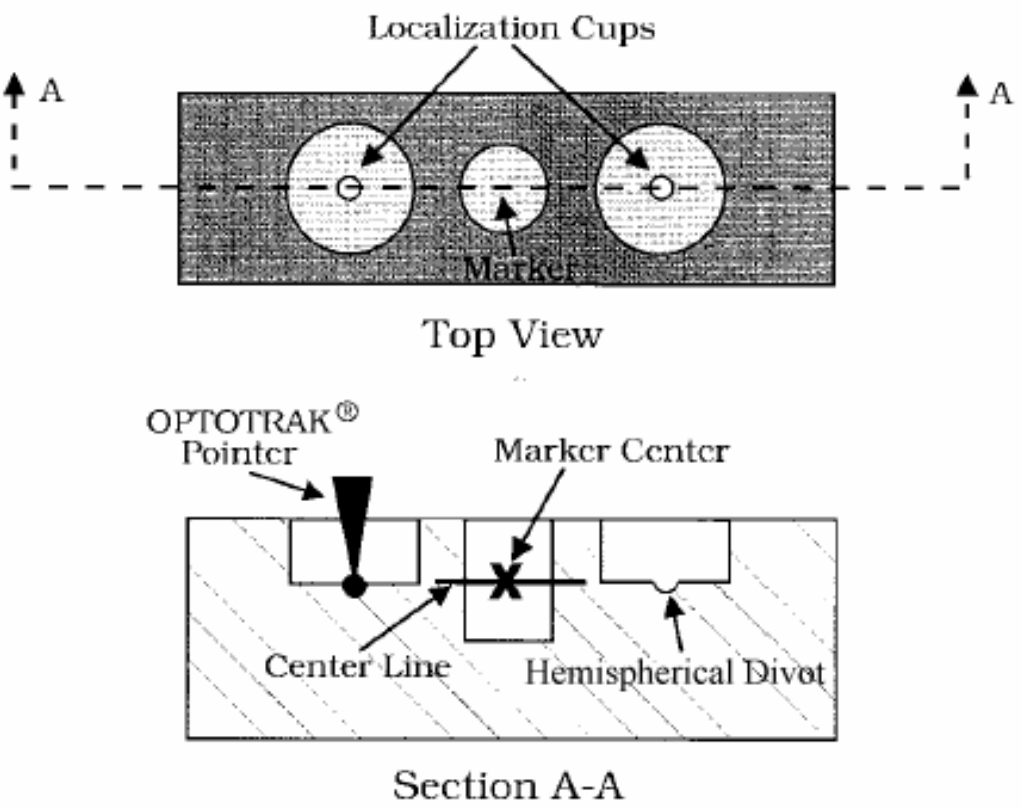

Figure 3.5. Since the OPTOTRAK pointer cannot "touch" the center of the marker analogue, "localization cups" straddle the marker. The pointer fits exactly into the hemispherical divots that are collinear with and equally spaced from the center of the marker analogue.

Automatic Detection and Localization Algorithm

A. Overview

An algorithm for automatic detection and localization of fiducial markers has been developed based on previous work described in the companion paper in which A-mode ultrasound was demonstrated to be appropriate for accurate transcutaneous marker localization [1]. Such an algorithm is required for practical use of the ultrasonic system in a clinical setting. The algorithm finds the center of a cylindrical fiducial marker in physical space, so that its position can be matched to the corresponding fiducial marker center found in image space. While passing the ultrasonic probe over the implanted fiducial marker, the algorithm automatically locates the plane of the bottom of the marker relative to the world coordinate

system. Then, capitalizing on the regular geometry of the marker, the algorithm calculates the coordinates of the center of the marker.

B. Surgical Scenario

When the detection system and markers are completely developed, the following surgical scenario will be possible. The fiducial markers will be implanted in the skull and tomographic scans will be acquired prior to surgery. In the operating room, the patient will be positioned in a Mayfield clamp for surgery. Then, detection and localization of the implanted markers with this new approach will proceed as follows: Ultrasonic transmission gel will be applied to the probe and the patient's scalp to enable ultrasonic coupling. The hand-held ultrasonic probe will be first positioned over an area that does *not* contain a marker in order to sample the particular patient's scalp thickness; this thickness is termed the *skin offset*. The probe will then be positioned over the area where the marker should be located. The probe will be moved back and forth in contact with the scalp while the computer system gathers signals. A determination will be made in real-time whether a particular echo is generated by the marker-bottom. The signals that contain these marker-bottom echoes are called *candidate signal*s. As each candidate signal is detected, a tone will be sounded to make the person operating the system aware of the probe's proximity to the marker. Once ten candidate signals are acquired, a second distinct tone will be sounded indicating that the computer has acquired enough signals for an accurate localization. The computer will then automatically calculate the location of the fiducial marker. The procedure will be repeated for the other fiducial markers implanted in the skull.

C. Determination of a Candidate Signal

The algorithm automatically classifies an ultrasonic signal as a candidate signal based upon analysis of the echoes contained within the ultrasonic signal. Figure 3.6 illustrates that progressively larger echoes are returned from the echogenic interface at the bottom of the marker as the ultrasonic transducer is passed over the marker. Notice that the scalp/skull interface echo occurs before the imaging-material/marker-bottom interface echo. This time differential is exploited to find candidate signals by setting a temporal threshold based on the skin offset; the scalp/skull echo occurs before this threshold and the imaging-material/marker-bottom echo occurs after this threshold. For these experiments, the threshold is set to be 3 μs beyond the skin

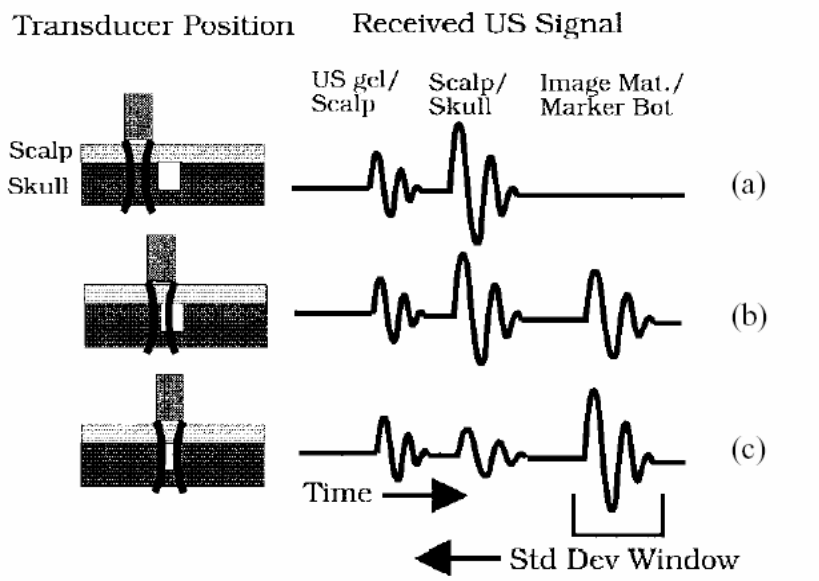

Figure 3.6. (a) When the ultrasonic transducer is not over the marker, there are only two principal echoes. (b) and (c) As the transducer moves over the marker, the imaging-material/marker-bottom interface begins to return an echo, and the echo from the scalp/skull begins to lose power. In order to detect the bottom of the marker, the standard-deviation window is moved from the end of the signal to the beginning.

offset (approximately 2-mm deeper than the scalp/skull interface, assuming a composite 1490 m/s). Any large echo arriving later than this threshold is considered a candidate signal.

Large echoes are defined by a standard-deviation threshold [18], [19]. As illustrated in Figure 3.6, the power in the windowed imaging-material/marker-bottom echo increases as the ultrasonic probe passes over the marker. The signal power is equal to the signal amplitude variance for zero-mean, time-domain signals such as A-mode ultrasound. Therefore, a high standard deviation (square root of the variance) in windowed segments of the signal indicates that the ultrasonic probe is over the marker. Each received signal is analyzed by moving a rectangular window from the end of the signal to the beginning (from the last sample taken to the first) (see Figure 3.6). Evaluating the signal in this direction is desirable because the first significant echo (large standard deviation) encountered can be classified as either the scalp/skull interface, or the imaging-material/marker-bottom interface depending upon the time-of-flight of the signal. Analyzing the signal in the other direction forces the classification of other interfaces that are not important to the localization process (e.g., the gel/scalp interface). The standard

deviation of signal samples within the rectangular window are calculated for each position of the window. This window is termed the *standard-deviation windo*w.

Since the standard deviation of the amplitude of the signal is related to the power of the signal, a constant standard-deviation threshold is set so that only large echoes are detected. This threshold may also be developed into a dynamic threshold that can change the system's sensitivity to marker echoes. One could imagine the threshold starting out high and automatically lowering if no candidates are found. Once a signal is determined to be a candidate signal, the location and orientation of the probe are stored along with that signal for later processing. The location of the probe is recorded as the 3-D coordinates of the probe tip and the orientation of the probe is recorded as the yaw, pitch, and roll angles of the probe shaft.

Figure 3.7 shows a signal returned from the probe when it is positioned over a marker in the phantom. The result of passing the standard-deviation window of the signal is also shown. Notice that choosing the window size to match the duration of the imaging-material/marker-

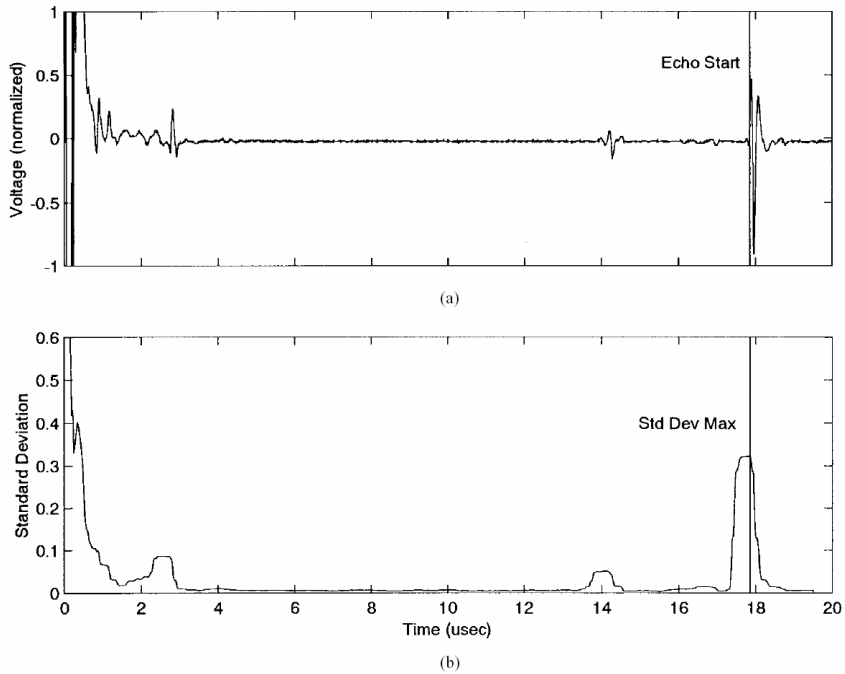

Figure 3.7. (a) A signal with a marker-bottom echo present and (b) the result of passing a 0.5-μs-wide standard-deviation window over (a). Notice that a prudent choice of the window size allows for the maximum standard deviation to occur when the leading edge of the window is aligned with the beginning of the echo. Recall that the standard-deviation window is moving from right to left; if a tie for maximum occurs, then the first occurrence of the maximum is taken as the echo position.

bottom echo causes the leading edge of the window to align with the beginning of the echo at a maximum standard deviation. The window size used currently is 0.5 μs (approximately 0.37 mm, assuming v = 1490 m/s). Since the imaging-material/marker-bottom interface causing this echo does not change between patients, this window size remains constant. A multiresolution search can speed the process of finding the initial maximum; however, the algorithm acquires signals and determines whether each signal is a candidate signal at a rate of about 4 Hz, which has been found acceptable in our experiments. In these experiments, the signal length was truncated so that echoes occurring beyond a depth of about 20 mm into the phantom (approximately 29 μs) were ignored. Note that this also sped the processing of the returned signal.

D. Location of the Marker Center

Once the candidate signals are captured, the localization calculations can begin. The algorithm calculates where the imaging-material/marker-bottom echo occurred in the world coordinate system using the probe position and orientation that were recorded for each candidate signal. The coordinates of the ultrasonic probe position are extrapolated in the direction of the probe (toward the marker-bottom). The length of the displacement vector is calculated by multiplying the time-of-flight of the ultrasonic pulse to the imaging-material/marker-bottom interface and the speed of sound through the scalp. The extrapolated imaging-material/marker-bottom position in world coordinates is termed a *candidate point* (see Figure. 3.8) and ideally is coincident with the marker-bottom. For this calculation, the v is assumed to be 1490 m/s in all materials. This composite v results from the 10 mm fat phantom and the ultrasonic coupling gel, both of which have a v = 1490 m/s. The speed of sound in the fat phantom was experimentally determined, while the speed of sound in the coupling gel is specified by the manufacturer [23]. Errors in the estimate of the v will result in localization errors. Lewis has calculated that an error of 1 m/s in v results in 0.67 μm axial distance error for each 1.0 mm of material thickness [18]. By combining our knowledge of the measured scalp thickness (skin offset) with average values for v in the scalp, this error can be minimized across patients.

Once all ten candidate signals have been processed, the position of the bottom of the marker is characterized by these candidate points which, ideally, lie in a plane. The plane through these points is determined analytically using an *eigenvector fit*. Duda and Hart [24] give

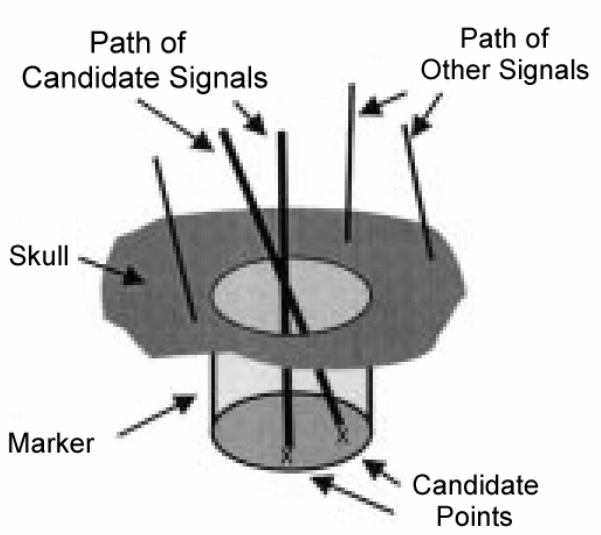

Figure 3.8. A candidate signal is found if there is enough power in the echo received from the imaging-material/marker-bottom interface. A candidate point is the location of the origin of the echo that produced the candidate signal. The candidate points will define the marker-bottom.

an excellent description of this technique in two dimensions; the technique is extended to three dimensions for the purposes of this algorithm. Unlike classic minimum-squared-error line fitting which minimizes the squared distances of points to a line relative to a coordinate axis, an eigenvector fit minimizes the perpendicular squared distance of the data points to a line. Thus, the resulting line from a best eigenvector fit is independent of any particular coordinate axis, which is important for this application.

Duda and Hart show that the line that minimizes the squared distance to the data is in the direction of the principal eigenvector of the scatter matrix of the data and passes through the mean of the data [24]. They define the scatter matrix, S, as

$$(1) \qquad S = \sum_{x \in X} (x - m)(x - m)^t$$

where x is an individual n-dimensional data vector in the sample space, X, and m is the arithmetic mean of the samples. Notice that the scatter matrix is proportional to the covariance matrix of the pooled data vectors, x.

In the case of 3-D data, the eigenvector fit delivers the plane that minimizes the squared perpendicular distance of each data point to that plane. This plane has a normal vector N in the

direction of the eigenvector associated with the minimum eigenvalue. Therefore, for the purposes of this algorithm, the best fit plane is described by N and a "weighted" centroid of the data.

The weighted centroid of the data is calculated using the information in the power of the echo returning from the bottom of the marker [1]

$$c = \frac{\sum_{x \in X} x\sigma_x}{\sum_{x \in X} \sigma_x} \qquad (2)$$

where c is the weighted centroid vector, σ_x is the power of the echo associated with the bottom of the marker for each signal. The signals returning from the probe when it is held over the center of the marker return the largest echoes and, therefore, have the largest standard deviation (see Figure 3.7). This method is robust and tends to "pull" the centroid to the true center of the bottom of the marker, even in the case of uneven sampling. Since the weight is related to the power in the echo returned from the bottom of the marker, signals returning from the center of the bottom have the most weight and those echoes near the edge of the bottom have the least weight.

Finally, the algorithm has all the information necessary to locate the center of the marker. The center of the marker is found by translating c through a distance of one-half the fiducial marker height (1.5 mm in the case of the phantom) in the direction of N. The direction of N is forced to be pointing toward the center of the marker by comparing the probe direction to the normal vector. If N is pointing away from the center of the marker, then N's direction is reversed. The result is the 3-D coordinates of the center of the marker in physical space.

Experimental Methods

A. Number of Candidates Signals

The number of candidate signals needed to locate the center of the marker analogue was determined experimentally. Several factors affect the number of candidate signals including the size of the marker and how evenly the marker-bottom is sampled. A larger fiducial marker

undoubtedly requires more candidate signals than a smaller fiducial marker in order to achieve equivalent localization accuracy for both markers. The localization accuracy of the marker hinges on how well the signals describe the bottom surface of the marker. In the interest of keeping the acquisition and calculation time low, the minimum number of candidate signals that yield an "acceptable" accuracy should be acquired.

An experiment was conducted to find an appropriate number of candidate signals. First, one marker analogue was localized with the pointer by touching the localization cups on either side as previously described. Since the pointer itself was not ideal, the position of each localization cup was an average of 50 individual localizations, allowing time to "pivot" the pointer in the localization cup. This yielded mean coordinates of the marker found with the pointer; these coordinates served as the "gold standard" location of the marker. Any difference between the ultrasonic system and the pointer was considered to be error in localization relative to the pointer. The Euclidean distance between each ultrasonic system localization and the mean pointer localization was calculated. The mean of 20 distances is reported here as the accuracy of the ultrasonic system. In this study, localizations using 5, 10, 15, and 20 candidate signals were investigated.

B. Comparison with OPTOTRAK Pointer

Additional studies further validated the accuracy of the ultrasonic localization system with direct comparisons to OPTOTRAK pointer positions. Four marker analogues on the phantom were localized with the pointer and the ultrasonic system. The 3-D position of the center of each marker analogue was determined. In addition, the ultrasonic localization was compared to the machined distances between the marker analogues. Since it is not practical to average several ultrasonic localizations in the operating theater, single ultrasonic localizations need to be compared with mean pointer localizations.

Results

The results center around the comparison of the performance of the OPTOTRAK pointer and the ultrasonic system. Figure 3.9 shows the comparison of the pointer localization and the ultrasonic probe for various numbers of candidate signals accepted. The plot presents the mean Euclidean distance between the ultrasonic probe localization and the pointer localization (x). In

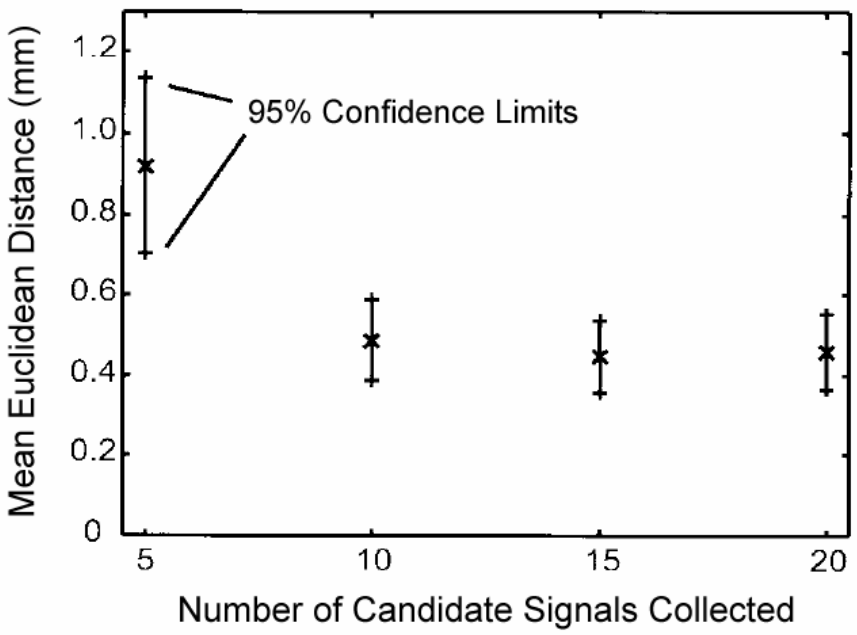

Figure 3.9. This plot shows the mean (x) Euclidean distance of the ultrasonic localization from the mean pointer localization for various numbers of candidate signals accepted. Also shown is the 95% confidence interval for the mean (+). Each mean was found with 20 localizations.

addition, the 95% confidence interval is shown for the mean (+). Table 3.1 shows the standard deviation and the maximum Euclidean distance found with each candidate signal trial.

In the operating room, each fiducial will be localized only one time by the ultrasonic probe. Therefore, Tables 3.2 and 3.3 contain fiducial positions found with only a single ultrasonic localization. Table 3.2 shows the direct comparison of the coordinates of the marker analogue as determined by the mean of the pointer localization and a single ultrasonic probe localization. Table 3.3 compares the ideal distance (as machined) between points on the head phantom with the distance measured by the ultrasonic system.

Table 3.1 Standard deviation and maximum Euclidean distances found in the determination of the number of candidate signals.

Number of Candidate Signals	**5**	**10**	**15**	**20**
Standard Deviation (mm)	0.5	0.2	0.2	0.2
Max Euclidean Distance (mm)	2.2	1.1	0.7	0.9

Table 3.2 Localization of marker analogues: ultrasound versus pointer.

Trial Number	Mean Pointer Loc. (n=20) X Y Z (mm from reference)	Single Ultrasonic Loc. X Y Z (mm from reference)	Euclidean Distance (mm)
Trial 1 Marker 1	-177.5 -196.6 338.6	-177.7 -196.7 338.9	0.2
Marker 2	-129.6 -236.3 382.7	-130.1 -236.4 382.9	0.5
Marker 3	-124.9 -208.6 336.6	-124.6 -208.9 336.9	0.3
Marker 4	-182.0 -224.3 384.6	-182.3 -224.1 384.4	0.3
Trial 2 Marker 1	-270.9 274.9 6.8	-271.1 275.0 6.9	0.2
Marker 2	-225.1 324.6 -28.5	-224.8 324.7 -28.5	0.4
Marker 3	-217.8 278.3 -1.8	-217.9 278.6 -1.9	0.1
Marker 4	-278.3 321.1 -20.0	-278.8 321.5 -20.1	0.5
Trial 3 Marker 1	-66.7 -73.9 -141.9	-66.8 -73.7 -141.9	0.1
Marker 2	-136.1 -60.6 -170.6	-136.5 -60.5 -170.9	0.4
Marker 3	-109.1 -44.3 -126.7	-109.9 -43.9 -126.7	0.7
Marker 4	-93.7 -90.2 -185.6	-94.1 -89.7 -185.6	0.4
		Mean	0.3
		Std. Dev.	0.2

Table 3.3 Localization of marker analogues: comparison to machined distances (accurate to 0.05 mm).

.

Trial Number	Distance Between Markers	Ultrasound Measured (mm)	Machined Distance (mm)	Absolute Difference (mm)
Trial 1	1 – 2	76.0	76.2	0.2
	3 – 4	76.2	76.2	0.0
	1 – 3	54.5	53.9	0.6
	2 – 4	53.7	53.9	0.2
Trial 2	1 – 2	76.6	76.2	0.4
	3 – 4	76.7	76.2	0.5
	1 – 3	54.0	53.9	0.1
	2 – 4	54.8	53.9	0.9
Trial 3	1 – 2	76.7	76.2	0.5
	3 – 4	76.2	76.2	0.0
	1 – 3	54.4	53.9	0.6
	2 – 4	53.6	53.9	0.3
		Mean		0.4
		Std. Dev.		0.3

Discussion

A. Accuracy and Precision

The accuracy of the system is a measure of how well the ultrasonic probe can find a point in space. The precision of the system is a measure of how well the ultrasonic probe can repeatedly measure the same location in space. In Figure 3.9, the mean Euclidean distance between the ultrasonic probe and the OPTOTRAK pointer serves as the measure of accuracy, while the standard deviation and confidence interval of the mean estimate serve as a measure of the precision.

The data in Figure 3.9 indicate that the mean localization accuracy of the ultrasonic probe is near 1.0 mm when using five candidate signals. This accuracy improves to near 0.5 mm when ten candidate signals are used. The 95% confidence interval of +/- 0.1 mm is derived from a standard deviation of approximately 0.2 mm for the 20 samples; the maximum distance was 1.1 mm (see Table 3.1). No profound improvement in localization is noticeable with either 15 or 20 candidate signals; therefore, ten candidate signals appear adequate to locate marker analogues. The number of candidate signals depends mainly upon the size of the marker used. If the marker were to increase in size, more candidates would most likely be needed to achieve a better characterization of the position and orientation of the marker-bottom. Smaller markers may require fewer candidate signals.

Table 3.2 shows the 3-D coordinates of four marker analogues. Each trial represents a change in the reference coordinate system by moving the reference rigid body. This result demonstrates that the accuracy does not depend upon the particular orientation of the phantom with respect to the OPTOTRAK coordinate system. The ultrasonic probe localization differed from the mean of the pointer localization by a mean Euclidean distance of 0.3 mm (0.2-mm standard deviation).

Table 3.3 shows the difference between the measured distance between points for the ultrasonic system and the machined distances. These distance differences serve as a measure of *relative* accuracy and are provided here as an indication of the accuracy of the ultrasonic system independent of the OPTOTRAK pointer. The ultrasonic system measured these distances with a mean absolute difference of 0.4 mm (0.3-mm standard deviation).

B. Metrics for Testing the Goodness of Localization

One of the strengths of this ultrasonic localization system is its ability to test for errors during the localization process. Error detection is accomplished by testing the variance in the data. For example, the spread of candidate points should not exceed a circular area defined by the bottom of the marker. If an exceptionally large distance is detected, those offending points, or the entire set of points can be discarded. Additionally, the candidate points can be tested to insure that they lie in plane. By projecting the data points onto N, a measure of the out-of-plane variance can be obtained. This information can be exploited to reject sets of points that are not sufficiently coplanar. Candidate points may not lie in a plane if the ultrasonic probe is lifted from the scalp during the localization process. If the operator lifts the probe, the signal will be misclassified as a candidate signal because the echo from the skull moves out further in time, beyond the skin-offset threshold. These metrics can be compared against acceptable values and a determination can be made very quickly, before the operator of the system moves to the next fiducial marker.

C. System Performance

These initial tests indicate that a reliable and robust method of localizing implanted fiducials is possible. The system's robustness can be attributed to several inherent features. The weighted centroid calculation tends to "pull" the center of the bottom of the marker in the correct direction, even in those instances in which the sampling is clustered away from the center of the bottom of the marker. Another advantage of the algorithm lies in finding the best-fit plane; this can help account for any tilt in the marker when inserted into the skull. No assumption is necessary about the orientation of the marker relative to the skull or to the ultrasonic probe.

Learning to use the detection system described here is easy. The main restriction on probe motion is that during the acquisition of candidate signals, the ultrasonic probe must maintain contact with the scalp for correct signal classification (candidate or noncandidate signal). Even if an incorrect classification is not detected, one of the localization metrics will show that this false candidate signal causes a greater variance in the candidate points than expected for the particular marker geometry. Poor localization can be rejected automatically or by the operator. The total time needed to acquire the ten candidate signals and to calculate the

position of one marker analogue is approximately 20 s. The total localization time for one patient with four or five fiducial markers implanted is less than two minutes.

Conclusion

Bone-implanted extrinsic fiducial markers represent a potential long-term mechanism for image to physical space registration and are desirable for patient comfort as well as for application to surgical follow-up, monitoring of therapy efficacy, and performing fractionated stereotactic radiosurgery. The major challenge to using implanted markers is the accurate localization of the markers in physical space after implantation.

A clinically useful A-mode ultrasonic technique for determining the location of fiducial markers implanted in the skull has been developed. The system was evaluated using fiducial marker analogues (3.7 mm in diameter, 3 mm in height) in a human-head phantom. The system is easy to use and finds each implanted fiducial marker in approximately 20 s. The prototype system compares well to the current method of exterior fiducial localization with an OPTOTRAK pointing device. The ultrasonic system differed from the pointing system by a mean of 0.5 mm with a 95% confidence interval of 0.1 mm when localizing the same point in space. This indicates that transcutaneous ultrasonic detection of implanted fiducial markers is possible with a high degree of accuracy. As the error in fiducial marker localization increases the application accuracy of the image-guided neurosurgical system decreases, so a high degree of localization accuracy is desirable. However, the application accuracy can also be increased by increasing the number of fiducials used in the registration process [17].

Acknowledgement

This work was supported in part by the National Institutes of Health (NIH) NINDS, under Grant NS28602 and in part by Johnson and Johnson Professional, Inc. The work of S. Schreiner was supported by the NIH under Research Training Grant T32 HL07712. The authors would like to thank H. Senel, M. Zink, Dr. G. Allen, and Dr. R. Maciunas for their contributions to this work.

References

[1] J. T. Lewis, R. L. Galloway, and S. Schreiner, "An ultrasonic approach to localization of fiducial markers for interactive, image-guided neurosurgery—Part I: Principles," *IEEE Trans. Biomed. Eng*., vol. 45, pp. 620-630, 1998.

[2] R. L. Galloway, R. J. Maciunas, and C. A. Edwards, "Interactive, image-guided surgery," *IEEE Trans. Biomed. Eng*., vol. 39, 1992.

[3] E. Wantanabe, J. Mayanagi, Y. Kosugi, S. Manaka, and K. Takakura, "Open surgery by the neuronavigator, a stereotactic, articulated, sensitive arm," *Neurosurg*., vol. 28, pp. 792–799, 1991.

[4] Y. Kosugi, E. Wantanabe, J. Goto, T. Wantanabe, S. Yoshimoto, K. Takakura, and J. Ikebe, "An articulated neurosurgical navigation system using MRI and CT images," *IEEE Trans. Biomed. Eng*., vol. 35, pp. 147–152, 1988.

[5] R. Mosges and G. Schlondorff, "A new imaging method for intraoperative therapy control in skull-base surgery," *Neurosurg. Rev*., vol. 11, pp. 245–247, 1988.

[6] R. L. Galloway, W. A. Bass, J. D. Stefansic, and R. J. Maciunas, "Incorporation of vascular information into interactive, image-guided surgery," in *Proc. SPIE Medical Imaging 199*6, vol. 2707, Feb. 1996.

[7] W. A. Bass, "Integration of angiographic data into an interactive, image-guided neurosurgical system," M.S. thesis, Vanderbilt Univ., Nashville, TN, 1996.

[8] C. A. Edwards, "A real-time, interactive stereotactic system," Ph.D. dissertation, Vanderbilt Univ., Nashville, TN, 1991.

[9] R. L. Galloway, C. A. Edwards, J. G. Thomas, and R. J. Maciunas, "Image display and surgical visualization in interactive, image-guided neurosurgery," *Optical Engineerin*g, vol. 32, pp. 1955–1962, 1993.

[10] R. L. Galloway, J. T. Lewis, S. Schreiner, T. Stanley, and R. Maciunas, "A new interactive image-guided surgical device," in *Proc. Annu. Conf. BME*S, Oct. 1992.

[11] R. L. Galloway, C. A. Edwards, J. G. Thomas, S. Schreiner, and R.J. Maciunas, "A new device for interactive, image-guided surgery," in *Proc. SPIE Medical Imaging* V, vol. 1444, Feb. 1991, pp. 9–18.

[12] O. D. Faugeras and M. Hebert, "The representation, recognition, and locating of 3D objects," *Int. J. Robot. Res*., vol. 5, pp. 27–52, 1986.

[13] K. S. Arun, T. S. Huang, and S. D. Blostein, "Least-squares fitting of two 3-D point sets," *IEEE Trans. Pattern Anal. Machine Intell*., vol. PAMI-9, pp. 698–700, 1987.

[14] J. West, J. M. Fitzpatrick, B. M. Dawant, Kessler, R. Maciunas, Ayache, Pennec, Barillot, Lemoine, Collignon, V. D. Elsen, Hemler, Napel, Sumanaweera, Evans, Fahey, Harkness, Hill, Kapouleas, Maintz, Noz, Rusinek, Pelizzari, Robb, and Woods, "Comparison and evaluation of retrospective intermodality," in *Proc. SPIE Medical Imaging 199*6, vol. 2710, Feb. 1996.

[15] V. R. Mandava, J. M. Fitzpatrick, C. R. Maurer, R. J. Maciunas, and G. S. Allen, "Registration of multimodal volume head images via attached fiducials," in *Proc. SPIE Medical Imaging V*I, vol. 1652, Feb. 1992.

[16] T. M. Peters, J. A. Clark, G. B. Pike, and C. J. Henri, "Stereotactic neurosurgery planning on a PC-based workstation," *J. Digital Imag*., vol. 2, 1991.

[17] C. R. Maurer, J. M. Fitzpatrick, M. Y. Wang, R. L. Galloway, R. J. Maciunas, and G. S. Allen, "Registration of head volume images using implantable fiducial markers," in *Image Processin*g, K. M. Hanson, Ed., SPIE 3034, pp. 561–579, 1997.

[18] J. T. Lewis, "Ultrasonic detection of subcutaneous fiducial markers for interactive, image-guided neurosurgery," Ph.D. dissertation, Vanderbilt Univ., Nashville, TN, 1992.

[19] J. T. Lewis and R. L. Galloway, "A-mode ultrasonic detection of subcutaneous fiducial markers for image-physical space registration," presented at *14th Annu. Int. Conf. IEEE EMB*S, Paris, France, 1992.

[20] J. T. Lewis and R. L. Galloway, "Three-dimensional localization of implanted fiducial markers for interactive, image-guided surgery," presented at *15th IEEE EMB*S, 1993.

[21] OPTOTRAK®. Rigmaker Guide, Northern Digital Inc., Waterloo, Ont., Canada, 1994.

[22] C. R. Hill, *Physical Principles of Medical Ultrasonic*s. New York: Wiley, 1986.

[23] Specification sheet for Acquasonic Ultrasonic Transmission Gel, Parker Laboratories, Orange, NJ.

[24] R. O. Duda and P. E. Hart, *Pattern Classification and Scene Analysi*s. New York: Wiley, 1973.

CHAPTER IV

SURFACE-BASED REGISTRATION OF PHYSICAL SPACE WITH CT IMAGES USING A-MODE ULTRASOUND LOCALIZATION OF THE SKULL

W. Andrew Bass[a], Robert L. Galloway, Jr.[a,b], Calvin R. Maurer, Jr.[c]

[a]Department of Biomedical Engineering, Vanderbilt University, Nashville, TN.
[b]Department of Neurologic Surgery, Vanderbilt University Medical Center, Nashville, TN.
[c]Department of Neurosurgery, Stanford University, Stanford, CA.

Portions of this manuscript have been published in:

Medical Imaging 1998: Image Display,
Proceedings of SPIE Vol. 3335, pp. 228-238, 1998.

Abstract

A method is described for computing the registration of computed tomography (CT) images of the head with physical space using the outer surface of the skull for registration and demonstrated with a phantom. The phantom is constructed by placing a latex swim cap over a plastic skull and pouring a gelatin mixture into the space between skull and cap. A Panametrics 10.0 MHz immersion type ultrasound transducer has been rigidly attached to an optically tracked probe [1]. This device is swept across the phantom while optical and ultrasound data are collected. A standard deviation sliding filter [2] is applied to the ultrasound signals to detect echoes arising from the skull. Echo data are transformed by the optical data to form a cloud of points representing the outer surface of the skull. CT derived models of the surface of the skull are generated from two separate algorithms. The first algorithm uses contours obtained from a deformable model-based segmentation algorithm [3] and the second creates an isointensity surface based on tetrahedral decomposition [7]. The isointensity surfaces are optionally simplified using an iterative edge removal algorithm [7]. The CT and ultrasound surfaces are registered using a modified iterative closest point (ICP) algorithm [4]. The effect of the simplification algorithm and the effect of doubling the CT slice thickness are examined. Registration results, validated with the Vanderbilt fiducial marker system [5], show it is possible to achieve target registration errors less than 3 mm which is an acceptable level of error for certain clinical uses.

Keywords: registration, physical space, ultrasound, surfaces, neurosurgery

Introduction

An important task in any image-guided surgery or image-guided therapy is to define a relationship between the patient and previously obtained images of the patient. In order to assist this task a coordinate system is assigned to the physical space occupied by the patient. Since the images of a patient contain their own coordinate system, the task of relating the images and the patient can be accomplished by determining a mathematical relationship between the image coordinate system and the patient coordinate system. This mathematical relationship between coordinate systems is referred to as a registration and the two coordinate systems are said to be registered with respect to each other. When the two coordinate systems both arise from images

of the patient, the registration is referred to as an image-space to image-space registration, or more simply an image to image registration. When one of the coordinate systems represents the actual patient the registration is classified as an image space to physical space registration. Ideally a point defined in one coordinate system will map to the identical point defined in the other coordinate system, but in reality there is always some error associated with these relationships.

This study tested the feasibility of performing image space to physical space surface based registrations using A-mode ultrasound. A specially constructed skull phantom was used to test the ability of a spatially tracked A-mode ultrasound transducer to localize the outer surface of the skull.

Methods

A. Data collection apparatus

The phantom was based on a plastic skull filled with caulk. Previously a large area of the skull had been removed on the skull's right side to simulate a craniotomy. For validation purposes five fiducial marker posts were attached to the outer surface of the skull at random locations. A latex swim cap was placed over the skull and the apparatus was suspended upside down. Gelatin was dissolved in water and the mixture was carefully poured into the area between the swim cap and the skull. The excess gelatin was used to fill a small 1" diameter cylindrical vial used to measure the speed of sound in the gelatin. The gelatin in both the phantom and the vial was allowed to solidify overnight. The next day a small hole was drilled in the right temple region of the skull and an eye screw was driven into the phantom. A 6 IRED Optotrak rigid body, referred to as the reference emitter, was securely attached to this screw to create a local coordinate system for all physical space measurements.

A Panametrics 10.0 MHz immersion type ultrasound transducer (Part No. V312) was used in the experiment. The crystal has a 0.25" diameter and is spherically focused to a depth of 0.52". This transducer was attached to a 25 IRED rigid body through the use of a custom made attachment (see Figure 4.1). The attachment is designed to place the transducer along the major mechanical axis of the rigid body (within machining tolerances). Early calibration experiments concluded that the deviation between the mathematical axis of the rigid body and the mechanical axis of the ultrasound beam was negligible.

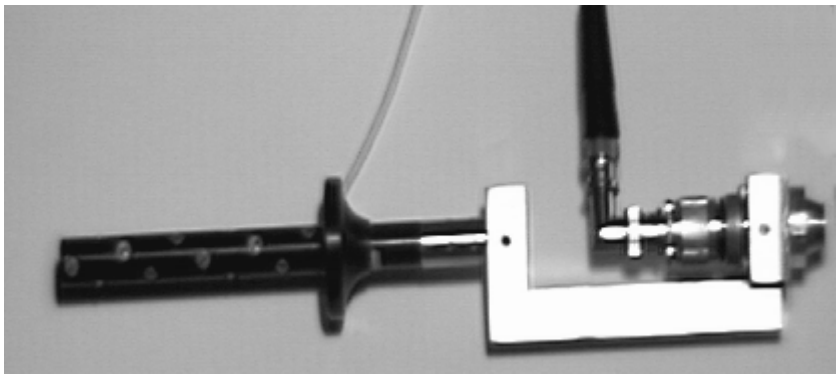

Figure 4.1 Ultrasound acquisition device

Calibration of the ultrasound acquisition device consisted of removing the ultrasound transducer from the rigid body attachment and placing a 1 mm spherical pivoting extension in its place. The attachment is then pivoted around a fixed point for approximately 30 seconds while position and orientation information is collected. The pivot data is used by the calibration software to translate the origin of the rigid body's mathematical coordinate system to the pivot point. After successfully calibrating the rigid body, the distance between the edge of the 1 mm pivoting ball and the edge of the rigid body attachment is carefully measured and the pivoting extension is removed. The transducer is then inserted back into the attachment and positioned such that the face of the transducer housing is at the center of the 1 mm pivoting ball as illustrated in Figure 4.2 (copied from Schreiner et al. [2]). This allows the spatial localizer to track the position and orientation of the face of the ultrasound transducer.

The transducer pulses are initiated, received, and amplified by a KB-AEROTECH^{TM} multiscanner. For this experiment, the multiscanner amplifier gain was set at its maximum (13 dB) and the dampening was set at its minimum (33 Ohms). The multiscanner output is connected to an analog to digital (A/D) conversion card (Gage Compuscope 250) in the PC. The A/D card is setup in single channel capture mode with a sampling frequency of 100 MHz. The input voltage range is +/- 100 mV and the signal is AC coupled. The A/D card is programmed to continuously capture the input signal into a circular buffer until a specified amount of time after a triggering event is received. The triggering level is set at -10mV with a positive trigger slope which enables the card to trigger on the first wave of the multiscanner's pulse. Since the card is set to continuously capture data prior to the triggering event, data for times both before and after the actual triggering event can be recorded. This allows the visualization and analysis of the

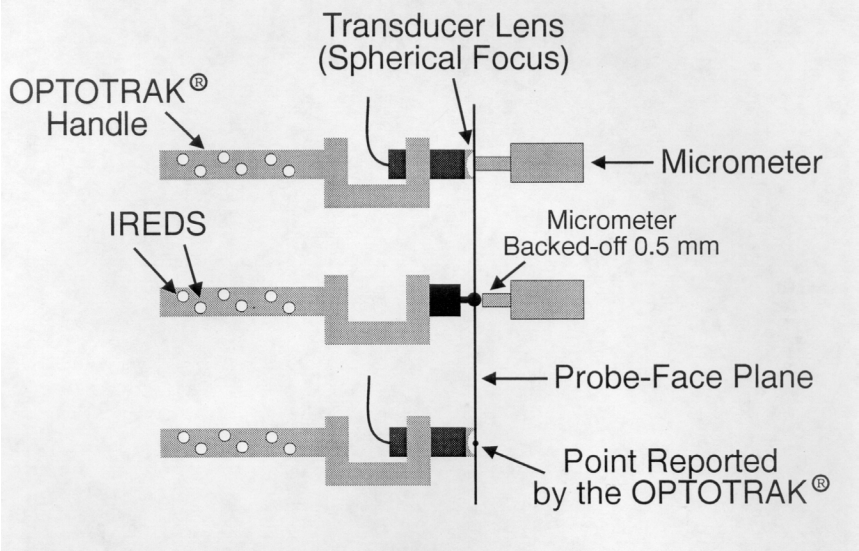

Figure 4.2. Alignment of transducer and probe

entire transducer pulse and corresponding echo. Additionally, the multiscanner's external pulse trigger input is connected to a serial port on the PC. This allows the PC to control the initiation of transducer pulses and therefore control the entire ultrasound signal acquisition process.

The pivoting procedure described above has placed the origin of the rigid body's coordinate system at the face of the transducer housing. However, because of the design of the transducer there is an unknown distance between the face of the piezoelectric crystal and the transducer housing. The transducer lens is filled with Aquasonic ultrasound transmission gel and positioned normal to a flat surface so that this distance can be measured using a time of flight technique. Ten pulses are sent to the transducer and the resulting ultrasound signals are stored for processing.

To measure the speed of sound in the gelatin mixture, the ultrasound transducer lens is again filled with Aquasonic ultrasound transmission gel. The length of the cylindrical vial of gelatin is carefully measured with a micrometer and the vial is placed on a flat table. The transducer is carefully placed on the upper surface of the gelatin and held normal to the table. Three ultrasound signals are acquired and stored for the speed of sound computation.

Aquasonic ultrasound transmission gel was applied liberally to the outer surface of the phantom and ultrasound signal collection was initiated. The PC was programmed to continuously pulse and receive signals from the transducer and record the spatial position and

orientation of the ultrasound rigid body. After each signal was received a simple threshold was applied to determine if the signal contained a likely skull echo. If the signal contained any points greater in magnitude than +/- 35 mV in a time window of 3 - 30 microseconds after the triggering event the signal was saved for later analysis and an audible beep was sounded by the PC. In addition to ultrasound signals and Optotrak position and orientation information, the residual errors from fitting the Optotrak rigid body IREDs to the mathematical rigid body models from both the reference emitter (providing the frame of reference for the phantom) and the rigid body attached to the ultrasound probe were recorded.

After the ultrasound signals were collected, the latex swim cap on the phantom was cut open without disturbing the reference emitter. The excess gelatin was removed and localization caps were attached to the marker posts. At this point it was noted that one of the marker posts was loose. All five markers were localized with a third, independent Optotrak probe. A total of 99 Optotrak acquisitions were captured for each marker and their average position was used as the location of the fiducial. After all of the physical fiducial localization had been concluded, the reference rigid body and eye screw were removed from the phantom. The next day imaging markers were snapped onto the marker posts and a CT scan of the phantom was acquired. (Siemens Somatom Plus, FOV: 231.5 mm, 512x512 matrix, Slice thickness 2 mm, gantry angle 0 degrees).

B. Generation of the Ultrasound data point sets

The voltage threshold filter described above was not sufficient to isolate the ultrasound signals containing strong skull reflections from all of the other signals acquired. For example, the filter allowed signals containing reverberation effects to be recorded. The start of the time window (3 microseconds) was early enough to allow signals containing aperture effects to be recorded. These signals were manually identified and removed from the pool of 299 signals recorded from the phantom. Additionally signals with above normal optical localization errors were eliminated. Specifically, optical localizations where the combined error from the rigid body attached to the ultrasonic transducer and the reference emitter was greater than 0.3 mm were removed. The remaining 238 signals were considered valid ultrasound signals with good quality positional and orientation information.

In order to measure the speed of sound in the gelatin and localize the skull of the phantom the location of the face of the ultrasound transducer housing within the ultrasound signals needed to be determined. A close examination of the 10 table signals collected for this purpose revealed that the triggering hardware on the A/D board is subject to about 50 ns of jitter. To account for this variation and improve measurement consistency a specific point during the piezoelectric crystal's response to the excitation pulse, hereafter referred to as the base point, was defined. The base point was chosen as the first zero point after the first transition from 255 to 0 (A/D units). Because this point is a feature of the transducer's response to the multiscanner pulse, it could be located in all of the ultrasound signals and used to align all of the signals with respect to each other.

A standard deviation sliding filter (510 ns width) similar to Schreiner et al. [2] was used to locate echoes within the ultrasound signals. The occurrence of an echo in an ultrasound signal is due to the reflection of the non-instantaneous excitation waveform from a surface boundary and therefore the echo is itself a non-instantaneous waveform. In order to compute distances with the time of flight equation, the time between the emergence of the excitation waveform from the face of the transducer housing and the return of the reflected waveform across the face of the transducer housing needs to be known. If these waveforms can be reduced into single points, the elapsed time between waveforms may then be computed as the time difference between the two points. The transducer response waveform was collapsed into a base point as described above. The reflected waveform was reduced into a single point, hereafter referred to as the echo point, by applying the standard deviation filter and selecting the maximum point in the filtered signal beyond the transducer's excitation waveform (1.5 microseconds). Figure 4.3 shows one of the ultrasound signals with a table echo on the top and the filtered signal and the echo point on the bottom. The average time between the base point and the echo point in the ten table signals was 2261 ns. When this time was multiplied by the speed of sound in Aquasonic transmission gel (1490 m/s) it yielded 3.37 mm which agreed well with a visual inspection of the transducer. The echo from the face of the transducer housing (when the transducer is filled with transmission gel) is therefore located 2261 ns beyond the base point in the ultrasound signals. This point in time will hereafter be referred to as the face point.

The speed of sound in gelatin was computed using the time of flight equation. First the base point and face point were found as described above. Next the echo point arising from the

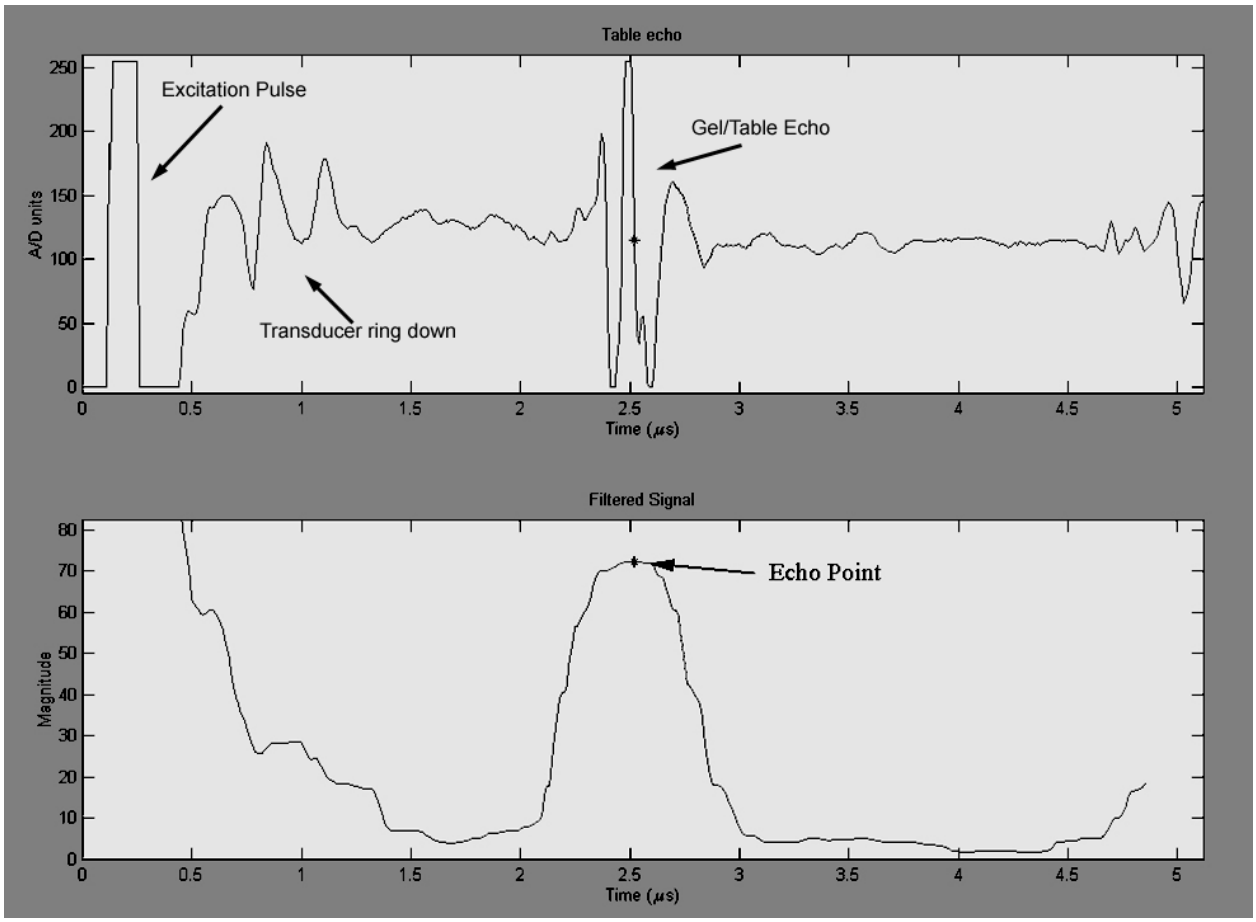

Figure 4.3 Sample ultrasound signal with a table echo (top) and windowed standard deviation filter output (bottom). Features visible in the ultrasound signal include the excitation pulse generated by the multiscanner, the transducer recovery or ring down period, and the echo arising from the transmission gel/table interface.

interface between the bottom of a 1" diameter gelatin filled vial and the table was calculated. Once all of the echo points were known the average elapsed time between the echo points and the face points determined. Note that both the echo points and the face points were computed using the same waveform decomposition algorithm. Since the base point location does not enter into the elapsed time measurement, the algorithm used to reduce the transducer response waveform into the base point may be different than the algorithm used to reduce the echo points and face points without affecting the accuracy of the elapsed time measurement. The elapsed time between the face point and the echo point for the first gelatin signal was 25,800 ns over a distance of 18.0 mm measured by micrometer. From this signal, the speed of sound in gelatin is estimated to be 1400 m/s. However, it was observed that the surface of the gelatin vial was

gouged by the transducer. So the length of the gelatin vial was reduced and a second measurement was taken. Three signals were acquired at the new vial length. The average elapsed time for the signals was 18,300 ns. Although the length of the vial was measured by micrometer to be 16.5 mm, a slight compression of the vial was observed during the ultrasound signal acquisition. Using this distance the speed of sound in gelatin is estimated to be 1810 m/s, however, the quality of this estimate is limited by the distance measurement inaccuracies.

Since the exact speed of sound will not be known for human experiments and given the questionable quality of the speed of sound measurement in the phantom experiment, ultrasound data point sets will be computed for varying values of the speed of sound between 1400 m/s and 1750 m/s.

Finally the base points, face points and echo points were identified in the 238 ultrasound signals of the phantom. For each signal the elapsed time between the face point and the echo point was multiplied by the speed of sound in gelatin resulting in the distance from the face of the transducer housing to the skull of the phantom. The top of figure 4.4 shows a typical

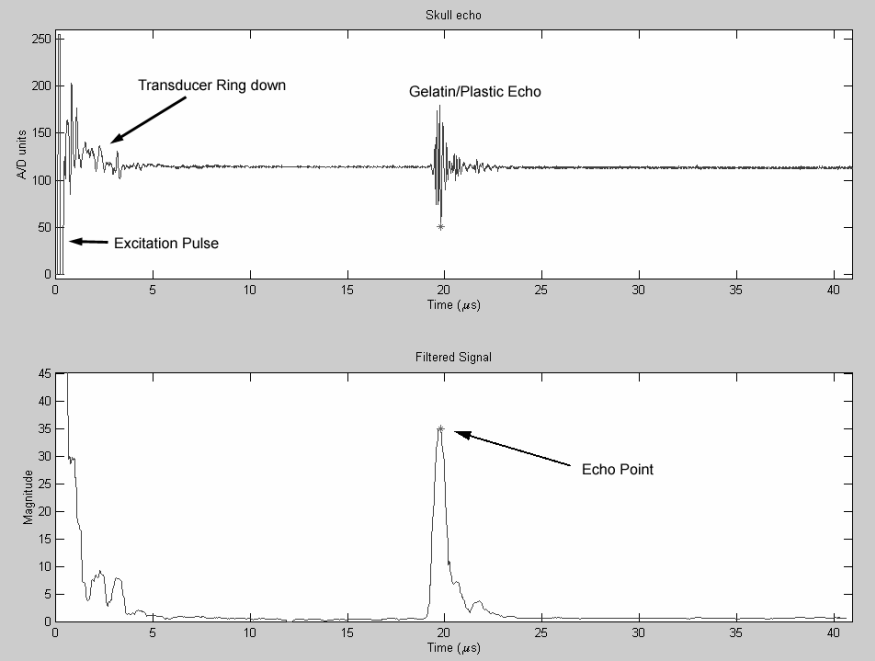

Figure 4.4 Sample ultrasound signal from the phantom (top) and windowed standard deviation filter output (bottom). Features visible in the ultrasound signal include the excitation pulse generated by the multiscanner, the transducer recovery or ring down period, and the echo arising from the interface of the gelatin and the outer surface of the plastic skull.

ultrasound signal from the phantom and the bottom shows the signal filtered with the standard deviation filter. Using the Optotrak position and orientation information recorded along with the signal, the location of the ultrasound transducer was transformed by the transducer's orientation and the distance to the skull to yield a point on the surface of the skull. Figure 4.5 shows the surface defined by the 238 points from the skull phantom.

Looking at Figure 4.5, it is obvious that at least one of the signals in the set of 238 is an outlier, so further identification of outliers may be necessary and the set of signals may need to be reduced below 238.

C. Generation of CT models of the skull

The CT images were transferred to a Sun workstation where the image fiducials were localized using a semi-automatic algorithm [5]. To create the first surface model, approximate contours were interactively drawn around the outer surface of the phantom's skull. No effort was made to include the jaw in the contours because this area was not localized during the

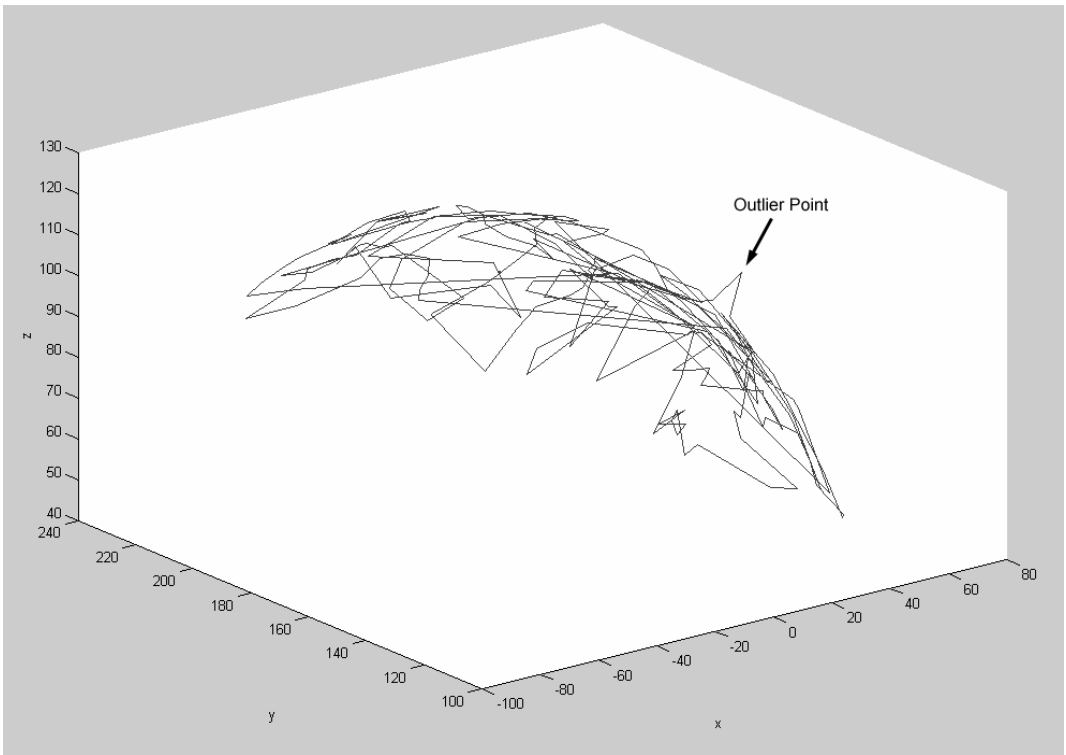

Figure 4.5 Surface defined by the ultrasound point set. Visible in this plot is a point that is not on the surface of the skull and is labeled as an outlier.

ultrasound acquisition process. The initial contours were refined using the approximate perpendicular contour algorithm of Aboutanos [3] and the resulting contour points were converted from pixel and slice coordinates to distances (with the origin of the coordinate system in the upper left corner of the first voxel). Finally a mesh generation program [6] was applied to the contours creating the triangle mesh. This surface will be referred to hereafter as model A. Figure 4.6 shows this mesh from a point of view looking down on the top of the skull with the face of the skull pointing down and slightly to the right.

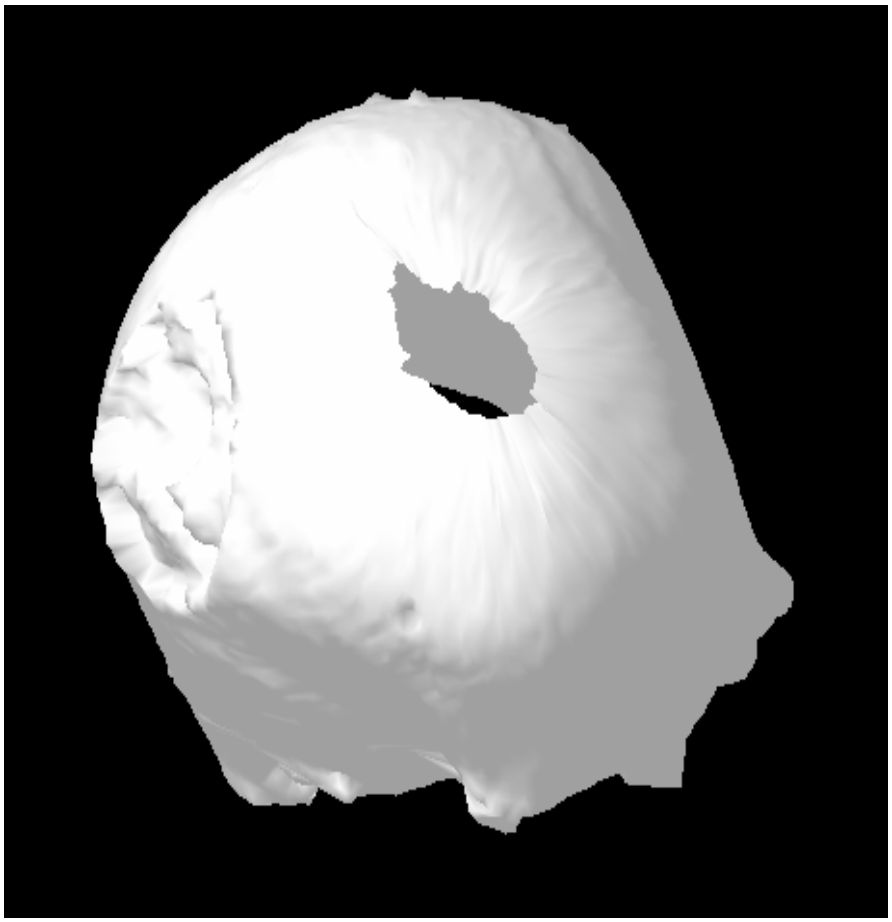

Figure 4.6 Contour-derived surface of the skull. Visible on the left of this image is the simulated craniotomy in the plastic skull. Since the mesh generation algorithm did not triangulate the upper and lower contours a hole is visible in the top of the mesh.

The tetrahedral decomposition algorithm of Gueziec and Hummel [7] is used to create isointensity surfaces and requires an intensity parameter. To help determine the value of this

parameter a histogram of the volume was constructed and relevant peaks and valleys were identified as seen in Figure 4.7. Based on the peak values for the surgical towels (used to support the phantom during the imaging) and the plastic skull, an intensity range of 300 to 1000 CT numbers was chosen for the isovalue parameter in the surface generation algorithm. The lower limit of this range is high enough to avoid surface contributions from the surgical towels and upper limit is low enough to eliminate contributions from the caulk in the interior of the phantom. However after rendering isosurfaces using the Marching Cubes algorithm in vtk 2.0 (Kitware, Inc., Clifton Park, NY.) it became obvious that the higher intensity thresholds produced poor surfaces particularly near the top of the phantom. See Figure 4.8, which shows a rendering of a surface defined by an intensity value of 900. Notice the pronounced stair step artifact and indentations that appear at the CT slice boundaries near the top of the skull. Since these artifacts exist in areas for which US data was collected and could negatively influence registration performance, it was decided to reduce the intensity range to 300-800. Visual inspection reveals that surface models in this range of intensities have far fewer of the artifacts previously mentioned. These surfaces will be referred to as model B.

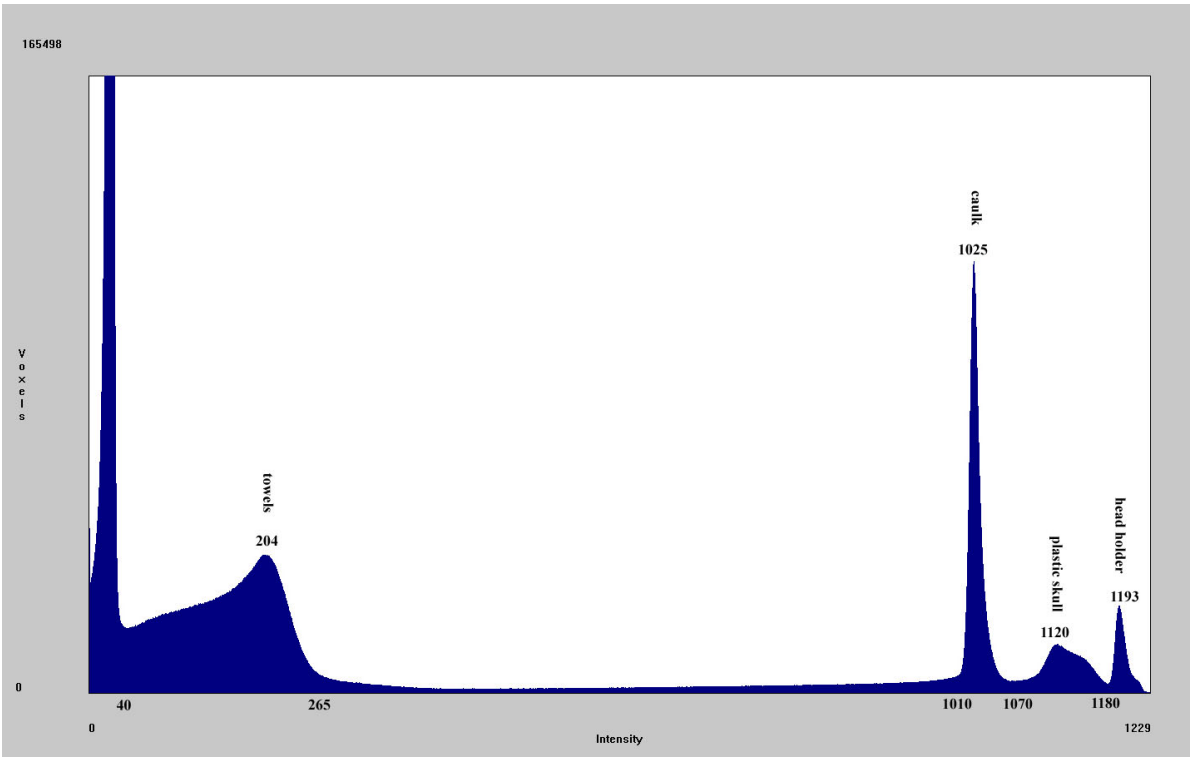

Figure 4.7 Histogram of CT image of the plastic skull phantom

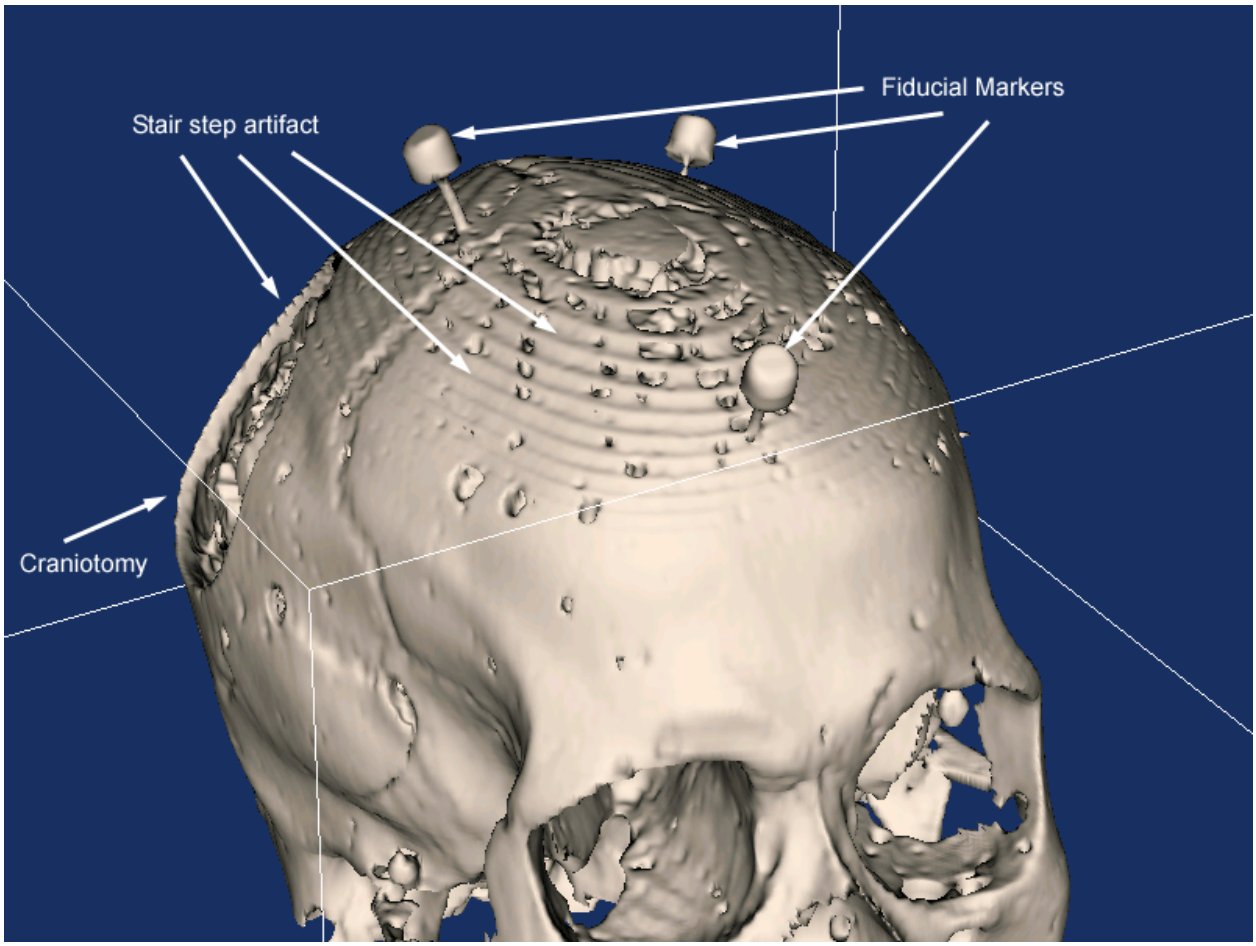

Figure 4.8 Rendering of the isointensity surface of the plastic skull phantom at intensity value equal to 900. The stair step artifacts, simulated craniotomy and three of the five fiducial markers are visible in this rendering.

One of the characteristics of the isointensity surface generation algorithm used is the large number of triangles in the resulting surface. Several steps were taken to reduce the total number of triangles in the surface for the purpose of decreasing the amount of computation time required to compute the registrations. First the CT images towards the bottom of the volume where no US data was collected were replaced with 0 filled slices. Second, the interior of the skull was manually segmented and masked out to prevent the air bubbles in the caulk from adding to the resulting surface. Third, a connected component algorithm was used to isolate the phantom surface from any background structures (such as the head holder). However, the resulting surfaces are still composed of a large number of triangles (e.g. 3,370,956 triangles for isovalue 700). Therefore an independent implementation [9] of an iterative triangle decimation algorithm [7] was used to simplify the surfaces. 50 iterations of the simplification algorithm

were used to reduce the triangle count for all isovalue surfaces and these simplified surfaces will be referred to as model C. In the case of isovalue 700 the number of triangles was reduced by over 90% to 224,344. The effect of this algorithm on the average number of triangles contained in the surfaces is shown in Figure 4.9.

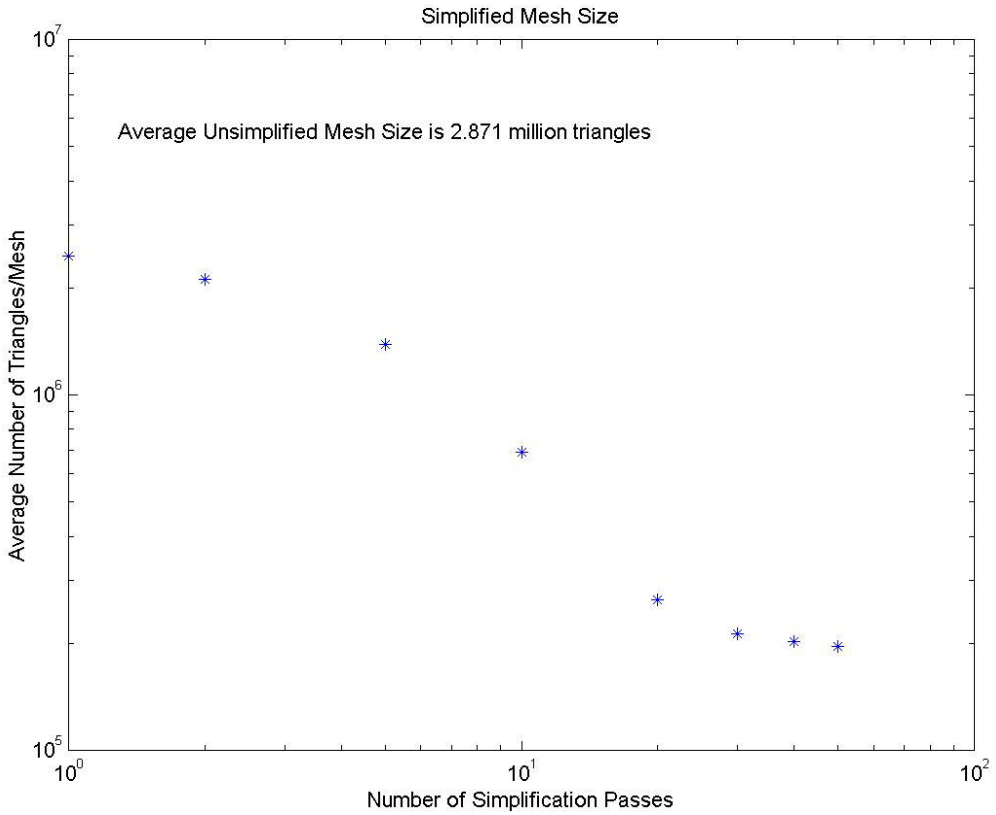

Figure 4.9 Average triangle count of simplified surfaces (original CT volume)

In order to determine the effect of a larger slice thickness on the registration errors, the CT volume was modified by averaging adjacent slices. This produces a CT volume, hereafter referred to as CT4, identical in extent of coverage but with 4 mm slices. This volume differs slightly from a natively acquired CT volume since the averaging technique does not take into account the non-rectangular slice profile of the CT scanner. All of the contour-derived and isointensity surfaces described above were generated from this volume; however, the isovalue

parameter range was reduced to 300-650 to reduce the amount of artifacts near the top of the phantom. These surfaces will be referred to as models D, E, and F.

Table 4.1 lists the segmentation algorithm, simplification level, and CT slice thickness for the six image models used in this study.

Table 4.1 Image models of the outer surface of the skull

Model	Algorithm	Simplification	CT thickness
A	Aboutanos	0	2
B	Gueziec & Hummel	0	2
C	Gueziec & Hummel	50	2
D	Aboutanos	0	4
E	Gueziec & Hummel	0	4
F	Gueziec & Hummel	50	4

D. Registration of the Ultrasound Point sets to the image models

One of the first things that must be chosen in the ICP registration process is an initializing transformation. In this experiment the transformation chosen is the fiducial marker registration. Using this initial transformation should allow us to see how close or far the surface data (i.e. the surface residual error) pulls the registration away from its ideal value (minimum of TRE). Note that the registration solution in these cases will be a local minimum of SRE but may not be the global SRE minimum.

Each iteration of the ICP algorithm computes the distance from the ultrasound points to the surface model of the skull. To identify potential outliers, the mean m, and standard deviation σ, of these distances are calculated. The points that are greater than $m + 3\sigma$ away from the model are discarded from future iterations of the algorithm.

E. Validation

In order to validate the registrations, a set of target points was constructed by sampling the volume inside the skull. First the inner surface of the skull was segmented (roughly) on the

CT images of the phantom. Then to reduce the total number of target points and taking account of the voxel dimensions only every fourth point in the in-plane dimensions of each segmented area was used to create the final set of 215,934 target points. The registration error at each of these points is computed by transforming the image point into physical space using the inverse transformation of the marker registration and then transforming that point back to image space using the surface based registration. The Euclidean distance between the original image space point and the final image space point is computed and the statistics may be computed over the distances corresponding to each target point in the set.

Results

After discarding the loose fiducial a "correct" point-based registration was computed using Arun et al.'s algorithm [8]. The output of this registration program is shown in Table 4.2. The top of the table shows the position of all four image fiducials used in the registration

Table 4.2 Fiducial registration results

REGISTRATION RESULTS

	Fiducials 2			Fiducials 1->2			Fid reg error (2 - 1->2)			
Fid.	X	Y	Z	X	Y	Z	X	Y	Z	TOTAL
1	167.91	67.34	94.83	167.78	67.67	94.76	0.14	-0.33	0.06	0.36
2	81.91	121.15	140.32	81.98	121.06	140.34	-0.07	0.09	-0.01	0.12
3	158.36	166.43	105.70	158.30	166.47	105.35	0.07	-0.03	0.35	0.36
4	142.41	199.95	10.75	142.54	199.68	11.15	-0.13	0.27	-0.40	0.50
							0.11	0.22	0.27	0.36

Rotation matrix			Translation vector
0.054947	0.998108	-0.027599	-56.867543
-0.652676	0.056822	0.755504	51.565672
0.755642	-0.023499	0.654563	46.516789

Fiducial registration error: 0.3618

calculation (labeled Fiducials 2), the position of the physical space fiducials transformed by the registration matrix (labeled Fiducials 1->2), and the distance between these locations (labeled

Fid reg error (2 - 1->2). The Euclidean distance between the image fiducials and the transformed physical fiducials is shown in the last column of the FRE. The bottom of the table contains the rotation matrix and translation vector that comprise the registration matrix and the overall fiducial registration error.

The surface registration errors for the contour-derived surface is shown in part a of Figure 4.10. The registration errors were computed for speed of sound in gelatin values of 1400 to 1750 in increments of 1m/s. The minimum surface registration error was 0.283 mm and occurred at

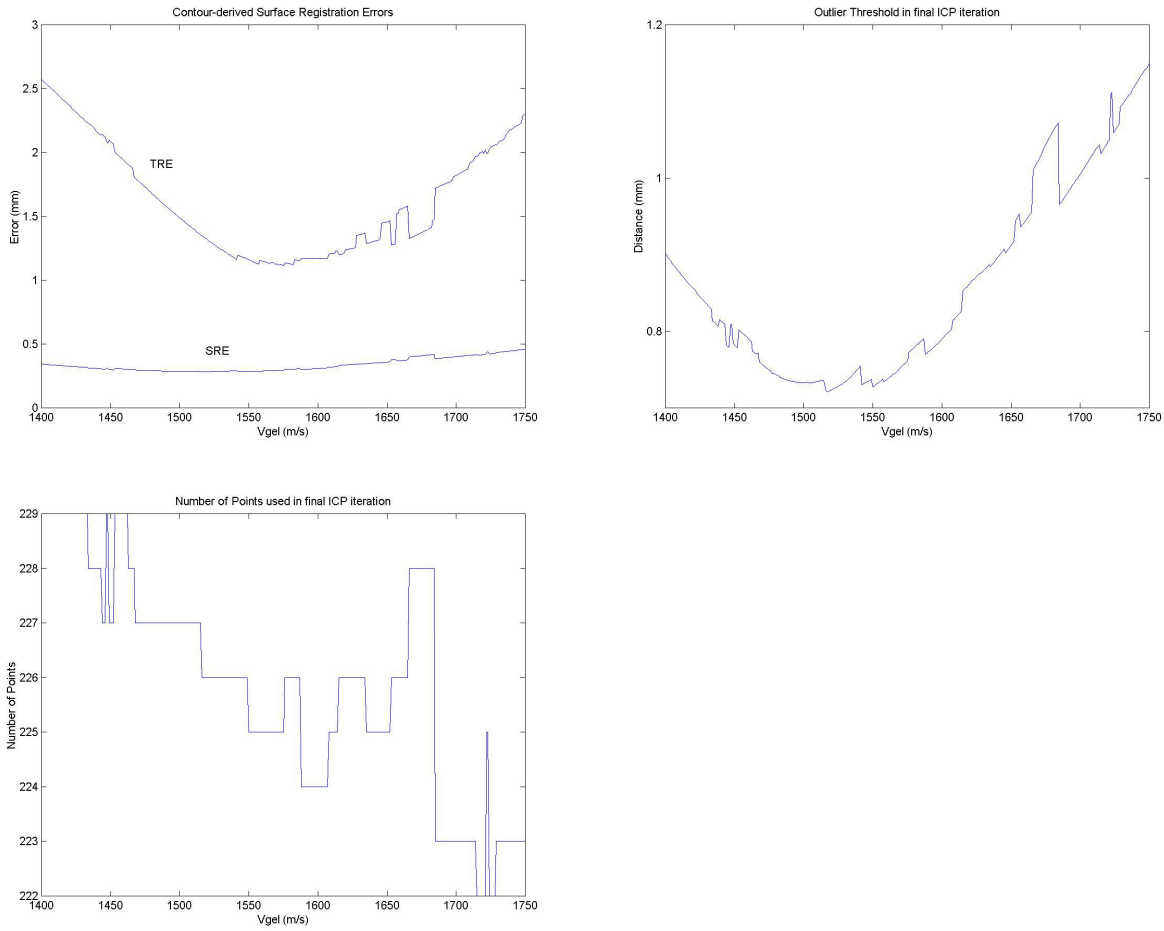

Figure 4.10 Model A surface registration results: (a) surface and target registration errors. The minimum SRE occurs at 1516 m/s and the minimum TRE occurs at 1575 m/s, (b) the outlier threshold (mean + three standard deviations of the distance between points and the surface) used in the final iteration of the ICP algorithm. (c) number of ultrasound points used in the final iteration of the ICP algorithm. Of the 238 points used in the first iteration, this is the number of points that passed the outlier threshold and were used in the final iteration of the ICP algorithm.

Vgel = 1516m/s. The rms statistic of the target points, hereafter the TRE, at the minimum SRE was 1.350 mm. The minimum value of the TRE was 1.115 mm and occurred at 1575 m/s.

The outlier threshold used in the final iteration of the registration algorithm is shown in part b of Figure 4.10. Also, the number of points (out of a total of 238) that fall within the outlier threshold is shown in part c of the figure.

The surface registration errors for the unsimplified isointensity surfaces are shown in parts a and b of Figure 4.11. As in the last figure, the errors have units of mm and the figures span a speed of sound in gelatin range of 1400 m/s to 1750 m/s and an isointensity range of 300 to 800 CT units.

The surface registration errors for the isointensity surfaces that have been passed through the surface simplification algorithm 50 times are shown in parts a and b of Figure 4.12. The figures show error in mm for ranges in the speed of sound in gelatin of 1400 m/s to 1750 m/s and ranges of isointensity value from 300 to 800 CT units.

In order to determine the effect of a larger slice thickness on the registration errors, contour-derived and isointensity surfaces were generated from the CT4 volume. For the isointensity surfaces, the isovalue parameter range was reduced to 300-650 to reduce the amount of artifacts near the top of the phantom.

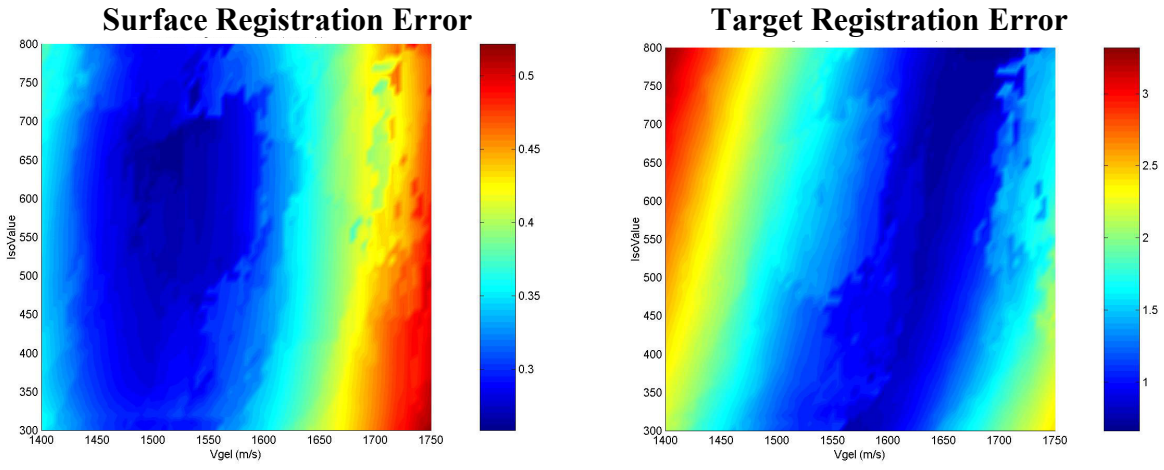

Figure 4.11 Model B registration results: (a) surface registration error vs. isointensity parameter and speed of sound in gelatin, (b) target registration error vs. isointensity parameter and speed of sound in gelatin. All registration errors have units of mm.

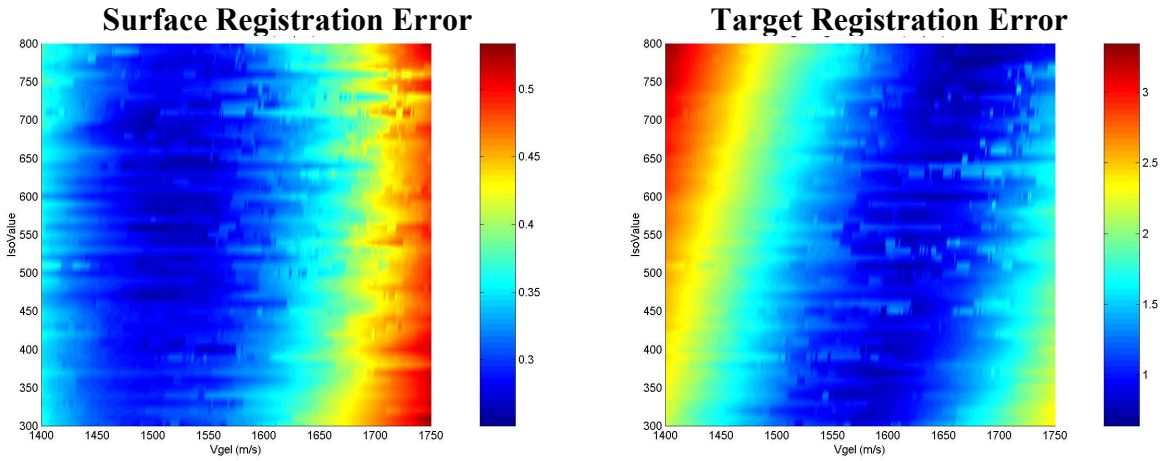

Figure 4.12 Model C registration results: (a) surface registration error vs. isointensity parameter and speed of sound in gelatin, (b) target registration error vs. isointensity parameter and speed of sound in gelatin. All registration errors have units of mm.

The surface registration errors for the contour-derived surface based on the CT4 volume are shown in part a of Figure 4.13. The registration errors were computed for speed of sound in gelatin values of 1400 to 1750 in increments of 1m/s. The minimum surface registration error was 0.314 mm and occurred at Vgel = 1502m/s. The rms statistic of the TRE, at the minimum SRE was 1.495 mm. The minimum value of the TRE was 0.899 mm and occurred at 1584 m/s.

The outlier threshold used in the final iteration of the registration algorithm is shown in part b of Figure 4.13. Also, the number of points (out of a total of 238) that fall within the outlier threshold is shown in part c of the figure.

The surface registration errors for the unsimplified isointensity surfaces are shown in parts a and b of Figure 4.14. As in the last figure, the errors have units of mm and the figures span a speed of sound in gelatin range of 1400 m/s to 1750 m/s and an isointensity range of 300 to 650 CT units.

The surface registration errors for the CT4 isointensity surfaces that have been passed through the surface simplification algorithm 50 times are shown in parts a and b of Figure 4.15. The figures show error in mm for ranges in the speed of sound in gelatin of 1400 m/s to 1750 m/s and ranges of isointensity value from 300 to 650 CT units.

To test the sensitivity of this registration process to initial alignment, the SRE value was computed for initial transformations that varied in translation and rotation from the marker

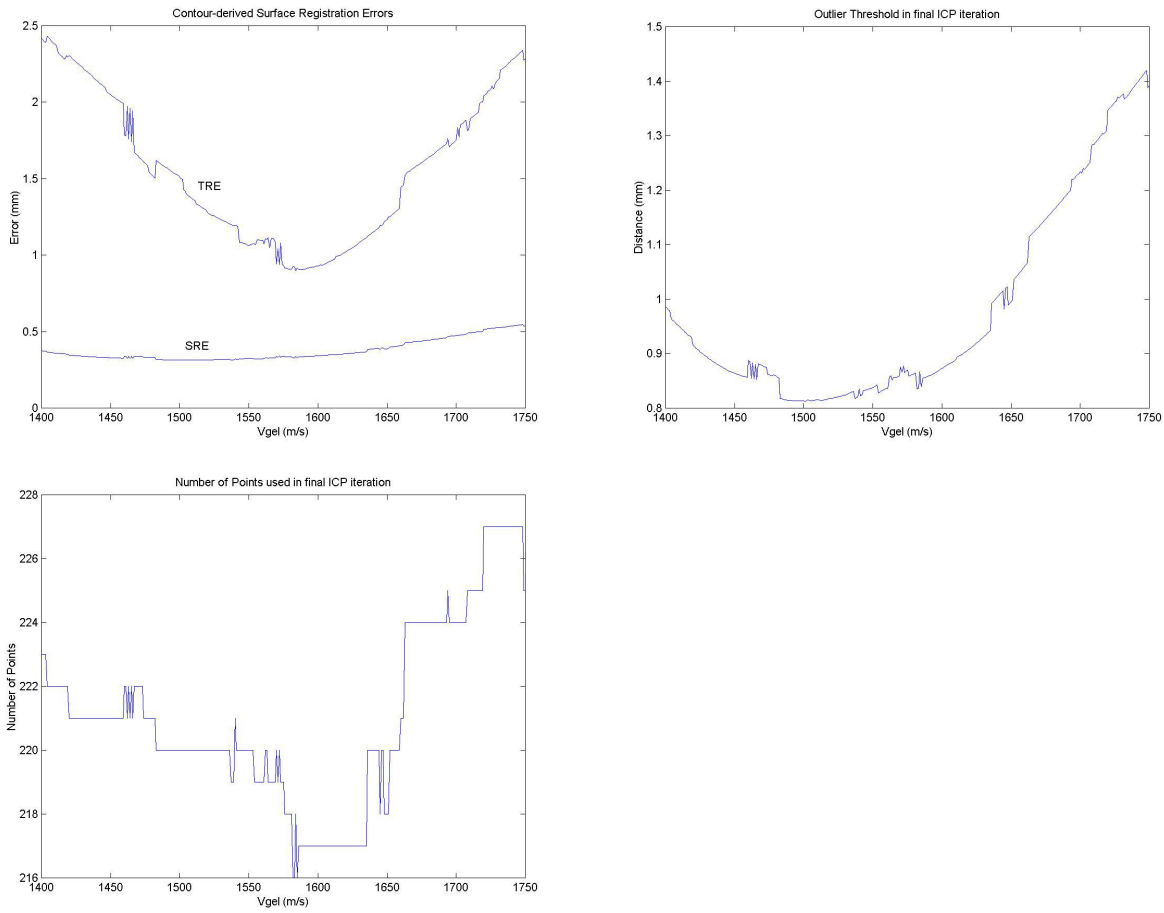

Figure 4.13 Model D registration results: (a) surface and target registration errors. The minimum SRE occurs at 1502 m/s and the minimum TRE occurs at 1584 m/s, (b) the outlier threshold (mean + three standard deviations of the distance between points and the surface) used in the final iteration of the ICP algorithm. (c) number of ultrasound points used in the final iteration of the ICP algorithm. Of the 238 points used in the first iteration, this is the number of points that passed the outlier threshold and were used in the final iteration of the ICP algorithm.

solution. Rather than test all possible combinations of models and parameters, a single model and set of parameters was chosen. Model C was chosen with a speed of sound value of 1550 m/s and an isovalue of 400. These values represent a point within both the TRE and SRE valleys in Figure 4.12.

Translation was varied +/- 5 mm in each Euclidean direction and the resulting error values varied smoothly from a minimum point near the marker solution throughout the translation values. To test rotation sensitivity, an ellipsoid was fit to the ultrasound surface data using an iterative optimization algorithm that minimized least squared error. Then SRE values

were computed for initial transformations that started at the fiducial marker solution and then were rotated around the axes of the ellipsoid. Graphs of the rotational SRE errors are shown in Figure 4.16.

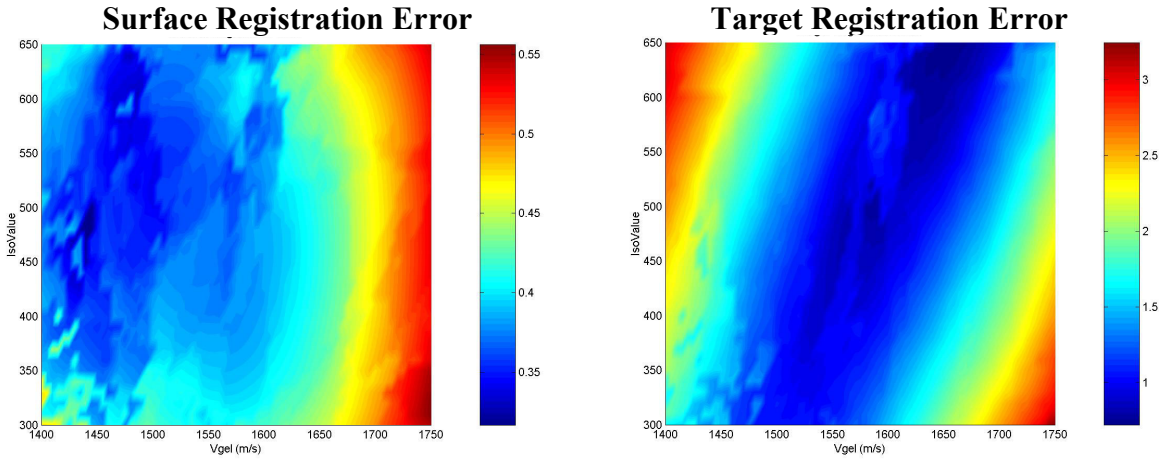

Figure 4.14 Model E registration results: (a) surface registration error vs. isointensity parameter and speed of sound in gelatin, (b) target registration error vs. isointensity parameter and speed of sound in gelatin. All registration errors have units of mm.

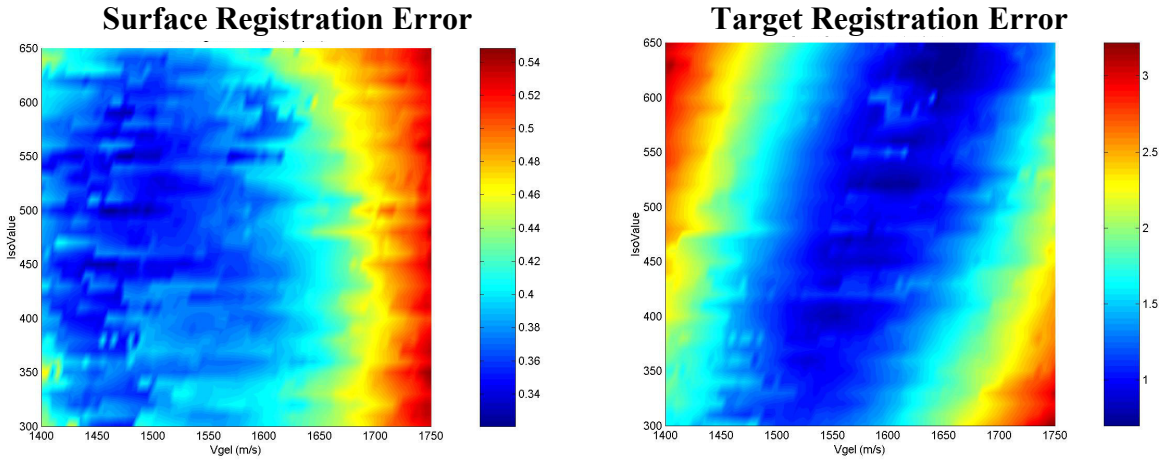

Figure 4.15 Model F registration results: (a) surface registration error vs. isointensity parameter and speed of sound in gelatin, (b) target registration error vs. isointensity parameter and speed of sound in gelatin. All registration errors have units of mm.

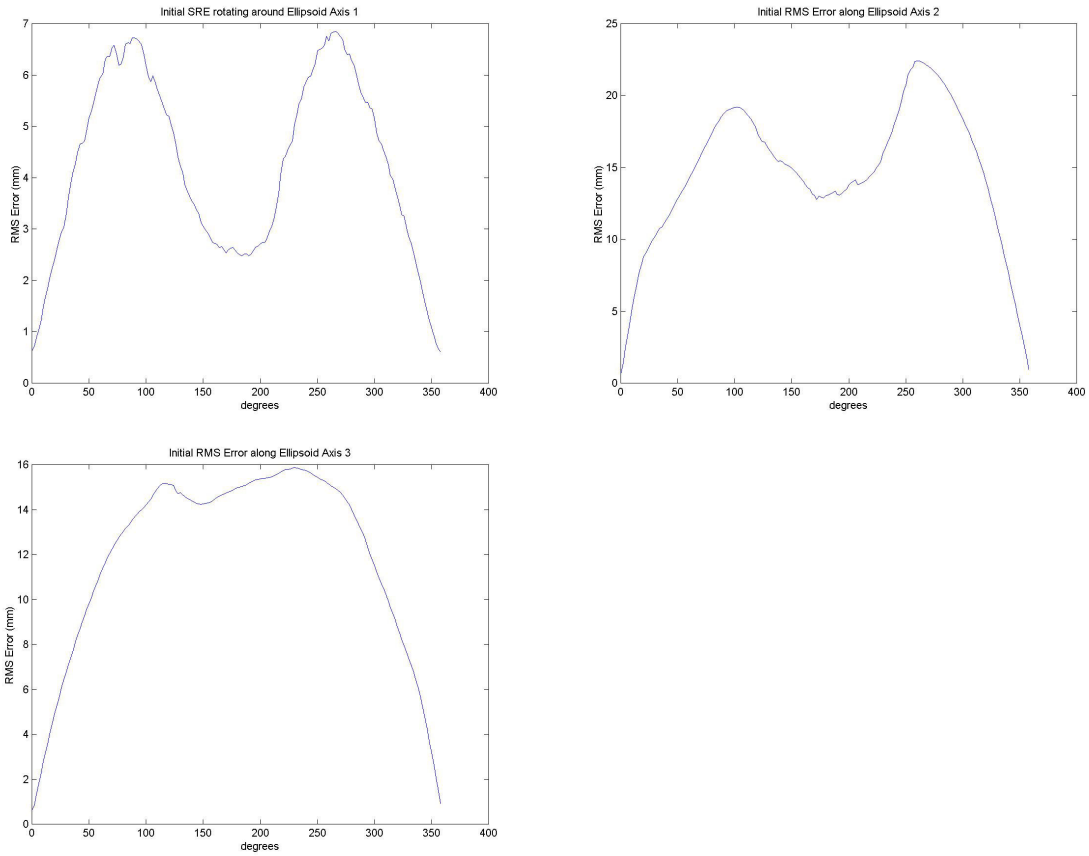

Figure 4.16 Initial SRE errors for misregistrations along the axes of the ellipsoid model.

Discussion

The contour-derived models A and D have similar registration results. Both the SRE and the TRE have a general concave shape with their minimums within the range of speed of sounds tested. However, in several places on these curves the values are discontinuous. This is due to the exclusion of individual data points based on the outlier threshold. The discontinuities in the graphs occur when the number of points used by the registration algorithm differs. In areas where the number of points used and by extension the actual points comprising the set used in the registration is constant, the graphs are smooth. The use of a standard deviation based outlier threshold is clearly a trade-off. While it can help eliminate true outliers it will also eliminate valid data points. For example, see Figure 4.13 between 1655 m/s and 1700 m/s. As the speed of sound is increased in this region 5 points are excluded from the point set which decreases the SRE and the outlier threshold but also decreases the TRE.

There are some differences between 4 mm and 2 mm CT slices. The 2 mm CT slices generates smoother SRE and TRE curves. Although the minimum TRE over all speed of sound values was smaller in 4 mm slices, the TRE value at the SRE minimum was smaller in 2 mm slices. In both cases the minimum SRE occurred at slightly more than 1500 m/s.

The isovalue models (B, C, E, and F) also have similar traits. The TRE plots of these models display a similar pattern. The region of minimum TRE is in a valley that follows a constant slope--as both the isovalue and speed of sound increase the TRE remains low. This can be explained simply. As the isovalue is increased the image model of the skull shrinks inwardly along its normal due to partial volume effects. Similarly as the speed of sound increases the echo points get further away from the transducer. Since the transducer must be approximately normal to the surface of the skull to record strong echoes, the direction of the echo point's motion is also approximately normal to the surface of the skull and therefore compensates for the image model shrinking along the slope of the valley.

The SRE plots of the isovalue models also display a common pattern although not as pronounced as the TRE plots. The minimum SRE values all have a much stronger dependence on speed of sound than on isovalue. The minimum SRE valley is broad and centered at approximately 1500 m/s. There appears to be a slight curve associated with this valley so that the relationship is not linear.

To help determine the registration effects of the simplification algorithm, the registration results of the models B and C and models E and F were compared. Figure 4.17 shows the errors of model B subtracted from model C. In these plots positive values represent a greater rms error statistic value in model B and negative values represent a greater rms error statistic value in model C. The TRE differences are all less than 0.6 mm with no definitive pattern. Over all of the range of isovalue and speed of sound values in the TRE plot, the average difference is -1.453×10^{-3} mm, and the standard deviation is 0.1165 mm. This indicates that the unsimplified model did slightly better overall, however, the difference in error level is not large enough to be meaningful.

Another effect the simplification algorithm has on registration is in execution time. Although the registration process execution time for the simplified surface is approximately 2.5 to 3 times faster than the execution time for the unsimplified surface, the execution time requirement for the simplification algorithm more than makes up for this advantage.

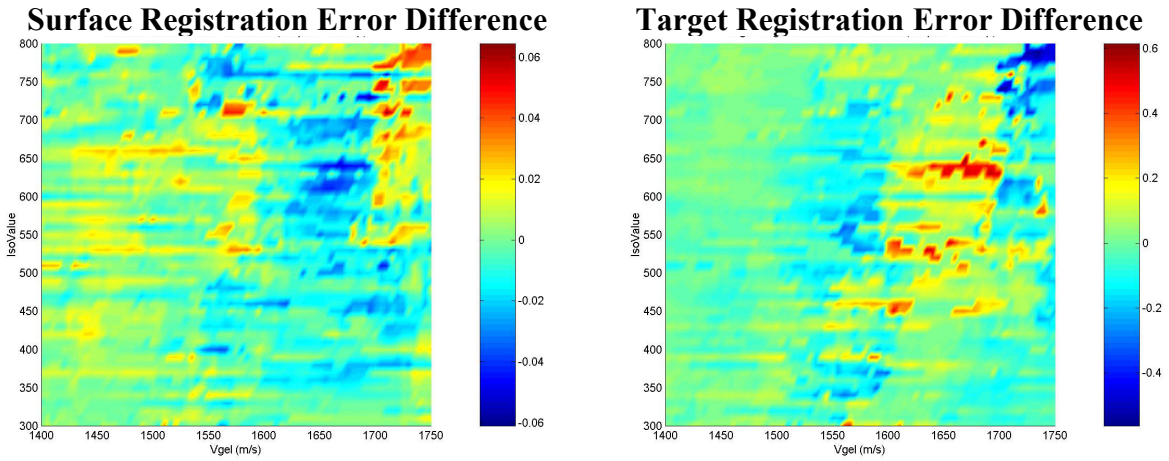

Figure 4.17 Differences in the registration errors between Model C (simplified) and Model B (unsimplified). Both models are formed from the original CT volume. (a) surface registration error difference between simplified and unsimplified models vs. isointensity parameter and speed of sound in gelatin, (b) target registration error difference between simplified and unsimplified models vs. isointensity parameter and speed of sound in gelatin. All registration errors have units of mm.

Similar to the previous figure, Figure 4.18 shows the errors of model E subtracted from model F. Positive values indicate that the rms error statistic has a greater value in model E, the

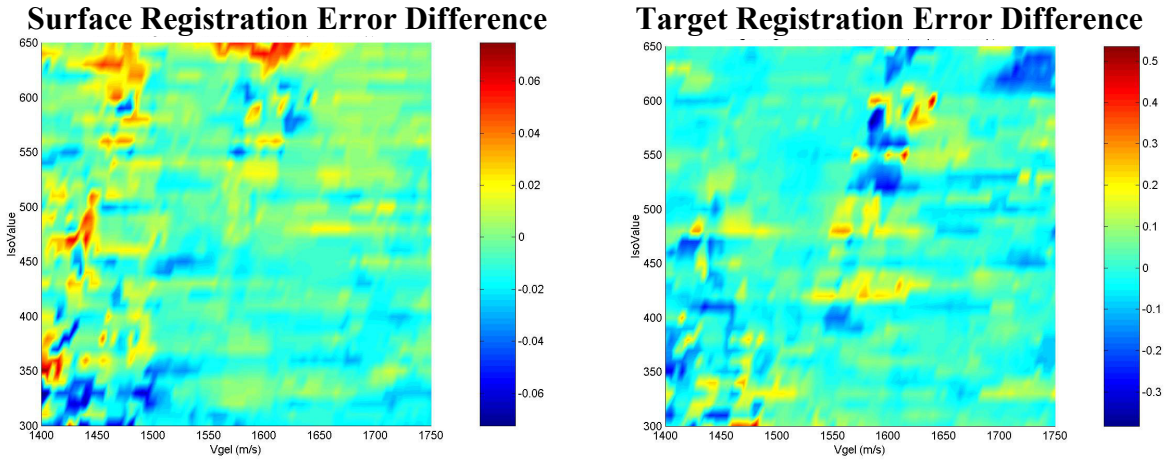

Figure 4.18 Differences in the registration errors between Model F (simplified) and Model E (unsimplified). Both models are formed from the CT4 volume. (a) surface registration error difference between simplified and unsimplified models vs. isointensity parameter and speed of sound in gelatin, (b) target registration error difference between simplified and unsimplified models vs. isointensity parameter and speed of sound in gelatin. All registration errors have units of mm.

unsimplified model, and negative values indicate that the rms error statistic has a greater value in model F which was processed by the simplification algorithm. In this case the TRE differences are all less than 0.5 mm with no definitive pattern. Over all of the range of isovalue and speed of sound values in the TRE plot, the average difference is 7.110×10^{-3} mm, and the standard deviation is 0.0860 mm. This indicates that the simplified model did slightly better overall, however, the difference is still not large enough to be relevant.

To determine the effect of doubling the slice resolution on registration errors models B and E and models C and F are compared. Figure 4.19 shows the errors of model B subtracted from model E. Positive values indicate that the rms error statistic has a greater value in model E, derived from 4 mm CT slices, and negative values indicate that the rms error statistic has a greater value in model B. In this case the TRE differences are all less than 0.8 mm but there are some overall patterns. In the SRE values, in the area of parameter space corresponding to the SRE minimum valley the 2 mm model has smaller errors and conversely elsewhere, the 4 mm model has smaller errors. This indicates that the SRE surface for the 2 mm model has a lower peak and rises faster than the surface corresponding to the 4 mm model. Also in the TRE plot the 2 mm model performs better to the right side of the TRE minimum valley and the 4 mm

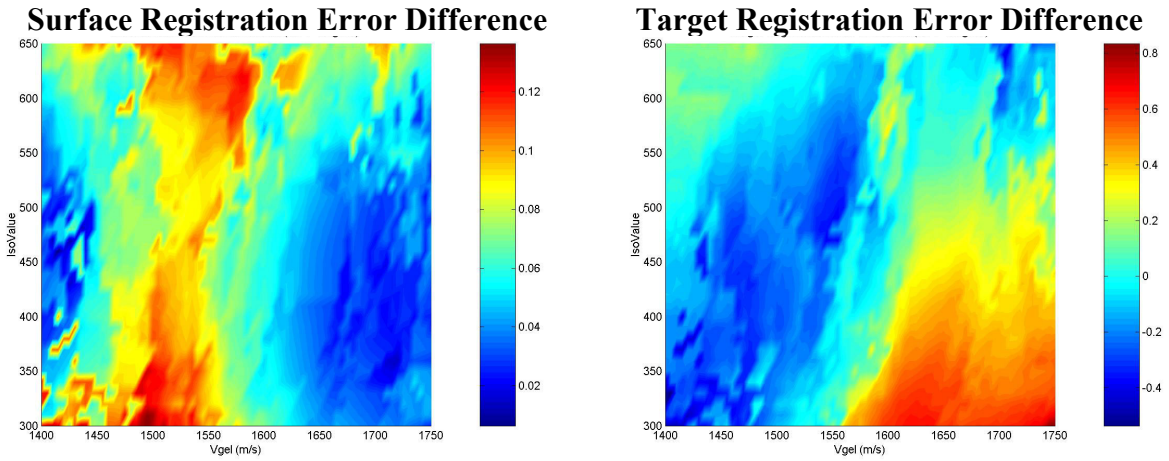

Figure 4.19 Differences in the registration errors between Model B (based on the original CT volume) and Model E (based on the CT4 volume). (a) surface registration error difference between a model created from 2 mm slices and a model created from 4mm slices vs. isointensity parameter and speed of sound in gelatin, (b) target registration error difference vs. isointensity parameter and speed of sound in gelatin. All registration errors have units of mm.

model performs better on the left side of the valley. Over all of the range of isovalue and speed of sound values in the TRE plot, the average difference is 0.0499 mm and the standard deviation is 0.2634 mm.

Similar to the previous figure, Figure 4.20 shows the errors of model C subtracted from model F. Positive values indicate that the rms error statistic has a greater value in model F, derived from 4 mm CT slices, and negative values indicate that the rms error statistic has a greater value in model C. Although the patterns are not as sharply defined for the simplified models as they are for the unsimplified models in the previous figure they are largely consistent. SRE has a lower minimum for the 2 mm model and higher values elsewhere and TRE statistics are lower for the 2 mm model to the right of the TRE valley and higher to the left of the valley. The TRE differences are all less than 0.8 mm and over all isovalues and speed of sound values the average difference is 0.05633 mm and the standard deviation is 0.2825 mm.

This investigation extends our preliminary findings [10] and builds on the independent implementation of the technique by Maurer et al. [11] by examining the effects of different segmentation algorithms, surface simplification, CT slice resolution, variation in the speed of sound, and a preliminary examination of sensitivity of the technique to initial misalignment.

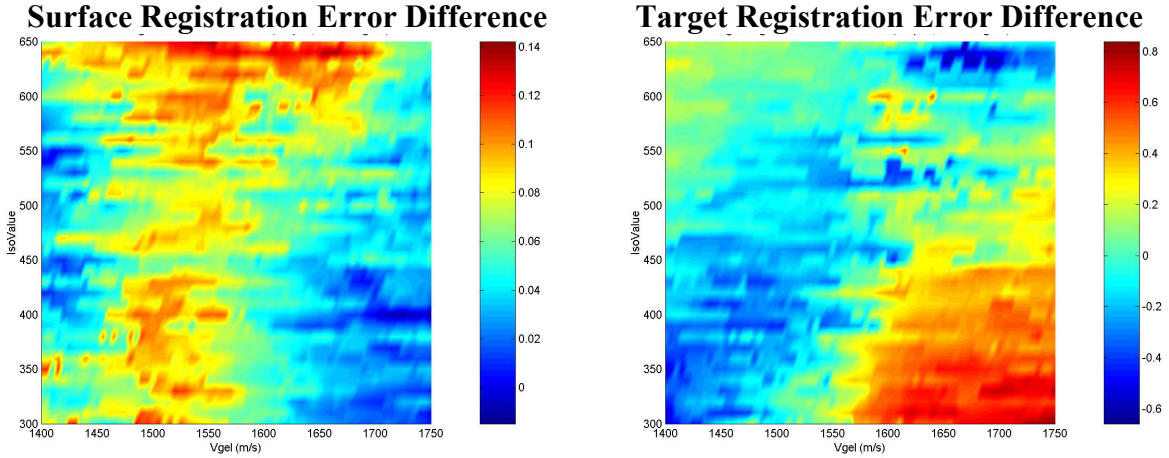

Figure 4.20 Differences in the registration errors between simplified surfaces Model C (based on the original CT volume) and Model F (based on the CT4 volume). (a) surface registration error difference between a model created from 2 mm slices and a model created from 4mm slices vs. isointensity parameter and speed of sound in gelatin, (b) target registration error difference vs. isointensity parameter and speed of sound in gelatin. All registration errors have units of mm.

Conclusions

This study has shown that it is possible to perform physical space to image space registration using the outer surface of the skull as identified in CT imaging and localized using a spatially tracked A-mode ultrasound transducer. Two algorithms for model generation were used, one using a deformable model-based segmentation algorithm [3] and the other using a tetrahedral decomposition [7] to create an isovalue surface. Although differing greatly in triangle count, the surfaces produced by the two algorithms performed equivalently. The minimum SRE occurs at roughly 1500 m/s in both algorithms and the TRE statistics display similar shapes and values (between 1 and 3.5 mm) over the range of parameters tested. There are subtle differences between isointensity surfaces that have been simplified by an edge deletion algorithm and generally speaking simplification up to 90% does not affect registration error levels, but the execution time required to simplify the surface outweighs any execution time advantage gained by the registration algorithm. Decreasing the resolution of the CT slices from 2 mm to 4 mm has little effect on the overall registration performance, although there are some regions of parameter space where the effects are more significant.

Finally, the sensitivity measures reported in this paper give some information about the shape of portions of the six dimensional SRE surface. Specific conclusions about the level of initial misregistration that the algorithm can accept and still converge to an acceptable solution can only be inferred from this data. Further investigation is needed to more concretely determine these ranges of values.

Acknowledgements

This work was supported in part by NIH grant GM 52798 and the department of neurosurgery at Vanderbilt University Medical Center. The authors would also like to acknowledge the invaluable help of Dr. Steve Schreiner and Dr. Judy Lewis.

References

[1] R. L. Galloway, Jr., R. J. Maciunas, W. A. Bass, and W. J. Carpini, “Optical localization for interactive, image-guided neurosurgery”, *Medical Imaging*, Y. Kim, Ed., Vol. 2164, pp. 137-145, SPIE, Newport Beach, CA, 1994.

[2] S. Schreiner, R. L. Galloway, Jr., J. T. Lewis, W. A. Bass, and D. M. Muratore, “An Ultrasonic Approach to Localization of Fiducial Markers for Interactive, Image-Guided Neurosurgery—Part II: Implementation and Automation”, *IEEE Transactions on Biomedical Engineering*. vol. 45, pp. 631-641, 1998.

[3] G. B. Aboutanos, "Image-Based Deformable Models for 3-D Automatic Segmentation of the Brain", Ph.D. dissertation, Vanderbilt University, 1996.

[4] P. J. Besl, and N. D. McKay, “A method for registration of 3D shapes”, *IEEE Transactions on Pattern Analysis and Machine Intelligence*, Vol. 14, No**.** pp. 239-256, 1992.

[5] M. Y. Wang, C. R. Maurer, Jr., J. M. Fitzpatrick, and R. J. Maciunas, “An Automatic Technique for Finding and Localizing Externally Attached Markers in CT and MR Volume Images of the Head”, *IEEE Transactions on Biomedical Engineering*. Vol. 43, No**.** 6, pp. 627-637, 1996.

[6] C. R. Maurer, Jr. (Nashville, TN, 1996).

[7] A. Gueziec, and R. Hummel, “Exploiting Triangulated Surface Extraction Using Tetrahedral Decomposition”, *IEEE Transactions on Visualization and Computer Graphics*. vol. 1, pp. 328-342, 1995.

[8] K. S. Arun, T. S. Huang, and S. D. Blostein, “Least-Squares Fitting of Two 3-D Point Sets”, *IEEE Transactions on Pattern Analysis and Machine Intelligence*, Vol. 9, No**.** 5, pp. 698-700, 1987.

[9] C. R. Maurer, Jr. (Nashville, TN, 1997).

[10] W. A. Bass, R. L. Galloway, Jr., C. R. Maurer, Jr., “Surface-based registration of physical space with CT images using A-mode ultrasound localization of the skull,” *Medical Imaging 1998: Image Display, Proc. SPIE*, vol. 3335, pp. 228-238, 1998.

[11] C. R. Maurer, Jr., R. P. Gaston, D. L. G. Hill, M. .J. Gleeson, M. G. Taylor, M. R. Fenlon, P. J. Edwards and D. J. Hawkes, "AcouStick: A Tracked A-Mode Ultrasonography System for Registration in Image-Guided Surgery", *MICCAI 1999*, pp. 953-962, 1999.

CHAPTER V

APPLICATION OF SURFACE-BASED REGISTRATION OF PHYSICAL SPACE WITH CT IMAGES USING A-MODE ULTRASOUND LOCALIZATION OF THE SKULL TO HUMAN PATIENTS

W. Andrew Bass[a], Robert L. Galloway, Jr.[a,b]

[a]Department of Biomedical Engineering, Vanderbilt University, Nashville, TN.
[b]Department of Neurological Surgery, Vanderbilt University Medical Center, Nashville, TN.

Abstract

This study describes the preliminary results of a method for performing physical space to image space registration using the outer surface of the skull as identified in CT imaging and localized using a spatially tracked A-mode ultrasound transducer in a patient population. Ultrasound point sets were collected from 12 patients scheduled for neurosurgical procedures. Two algorithms [1, 2] were used to generate five image models that were registered with three point sets generated from the ultrasound data using different speed of sound values. The point sets were registered to the image models using the iterative closest point algorithm [3]. Validation was performed by comparing the surface registrations to a gold standard point based registration over a set of target points. Similar to a previous study using this registration technique on a phantom [4] no large differences between the target registration errors (TREs) of the image models and point sets was observed. The TRE errors ranged from 0.7 mm to 4.1 mm when compared to the gold standard registration. However, since the point based registration used as the gold standard was measured, it has its own estimated error that must be taken into account. No relationship was observed between the number of points used in the registration algorithm and the TRE over the range of points collected in this study.

Introduction and Background

Stereotactic neurosurgery is a precise method of accessing deep-seated brain pathologies located by three-dimensional coordinates. Today, most stereotactic neurosurgical procedures use some form of computer-aided surgical guidance which minimizes surgical exposure and increases the accuracy of biopsies. In interactive image-guided neurosurgery (IIGN), the surgical guidance system provides real time display of diagnostic images corresponding to tissue located at the current position of the surgeon's probe. This reduces the surgical risks and increases the likelihood of surgical success. One of the key components of stereotactic procedure is the method used to accurately match or register the diagnostic images of the patient with the position of the patient during the surgical procedure. Both invasive (stereotactic frames, bone implanted fiducial markers) and noninvasive methods (anatomical landmarks, scalp attached fiducial markers) have been used to solve the registration problem. The objective of this research is to characterize the performance of a novel method for noninvasive registration. The proposed method uses a spatially tracked, 10 MHz A-mode ultrasound transducer to

accurately measure the location of the patient's skull. The patient's skull is then matched with a mathematical model of the patient's skull derived from the diagnostic images. The research will be performed in two phases. Phase I will refine the signal processing algorithm parameters used to detect the location of the skull using a subject population of normal volunteers. In phase II a subject population of volunteers from patients undergoing a stereotactic neurosurgical procedure will be used to access the accuracy of this registration technique against a known standard.

Methods

A. Hardware changes

A previously described [5] spatially tracked ultrasound measuring device was used in both phase I and phase II of this research. However, to account for any temporal discrepancy between the ultrasound measurement and the optical measurement the acquisition method was modified. The optical digitizer was configured to capture data in a triggered mode rather than the normal free running mode. When triggered, two frames of data are acquired and the device returns the interpolated position at the center of the time period. A delay circuit was added between the PC, which initiates the data capture, and the ultrasound pulser so that the pulser is fired at the center of the optical data collection window.

For phase II, two of the four posts on a CRW stereotactic frame (Radionics, Inc) are modified by attaching two fiducial marker posts [6] to each of the frame posts. This will allow the attachment of imaging markers [6] during CT acquisition and physical localization caps [6] prior to the operation. These fiducial markers will be used to compute a reference point based registration using the method of Arun et al. [7].

B. Data Acquisition

In phase I, ultrasound signals were recorded from the scalp of 6 volunteers (min 32 signals, max 37 signals). The ultrasound transducer was placed at arbitrary points on the volunteer's scalp and signals were acquired individually. No attempt was made to continuously acquire data while translating the probe across the scalp. Signals were collected with an approximately uniform density from different areas of the scalp. This data was used to verify the

operation of the echo detection algorithm on humans and to set a realistic value for the echo power threshold.

During phase II data was collected from a total of 12 patients. A typical case starts with the attachment of the stereotactic frame to a patient. Four frame posts are used to secure the base ring to the patient. Fiducial marker posts have been affixed to two of these frame posts. The marker posts protrude in opposite direction from each other and the two modified frame posts are placed on opposite sides of the patient to increase the spatial spread of the fiducial markers. Figure 5.1 shows the location of the fiducial markers on the CRW frame with the patient present and with the patient's skull segmented out of the image.

After frame attachment, the patient is taken immediately to the CT scanning suite where the imaging caps would be attached to the marker posts and the patient would be positioned on

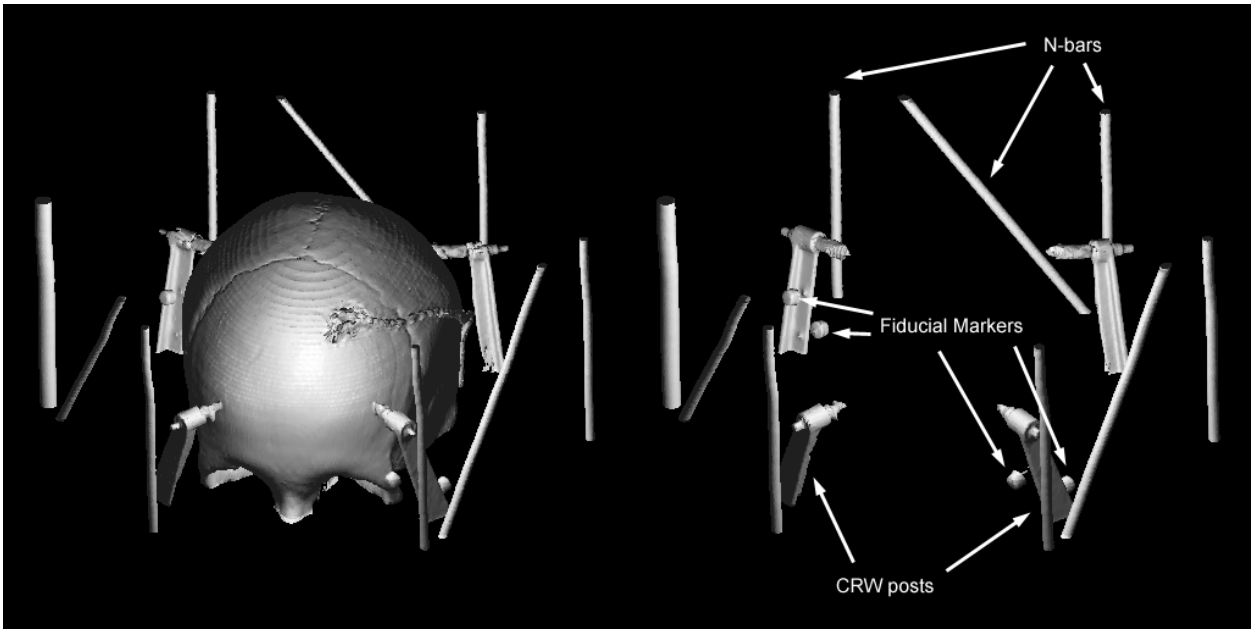

Figure 5.1 Fiducial marker placement on the CRW stereotactic frame. Two fiducial markers are placed on the opposing sides of two of the four CRW posts. The right pane has the skull removed to better visualize the fiducial marker placement.

the scanning table. A CT volume (Siemens Somatom Plus, FOV: 320 mm, 512x512 matrix, Slice thickness 3 mm, gantry angle 0 degrees) would then be acquired. (The CT data for case 11 was acquired with 2 mm thick slices.) Afterwards the imaging caps would be removed and the patient would be transported to the operating room. Upon arrival in the operating room the staff

would start preparing the patient for the operation while the surgeons planned the procedure using the newly acquired images. As part of the normal preparation the patient's head would be immobilized in a Mayfield head clamp (Ohio Medical Instruments, Cincinnati, OH.). A biopsy guide clamp was used to temporarily attach an optical reference emitter to the CRW frame base ring and localization caps were attached to the fiducial marker posts. An Optotrak 3020 (Northern Digital, Inc, Waterloo, Ontario, Canada) probe instrumented with a 3 mm ball tip was used to measure the fiducial locations. 100 data points were collected for each fiducial and the average value used as the estimate of the fiducial location. After fiducial measurement, the localization caps were removed and ultrasonic transmission gel was applied to the patient's scalp. Data was continuously acquired as the ultrasound acquisition device was moved across the patient's scalp. Hair on the patient's head did not prevent data collection but it did slow down the procedure. The data collection application displayed the raw and filtered ultrasound waveforms and current power and time thresholds. This visual feedback helps the operator interactively align the orientation of the transducer normal to the skull. An audible beep was generated for each valid point collected. The data collection process could be paused simply by obstructing the Optotrak camera's view of either the reference emitter or the transducer probe. After the data collection was finished the reference emitter was removed.

Table 4.3 from Christensen's Ultrasonic Bioinstrumentation [8] lists the speed of sound in various tissues. Blood is listed as 1580 m/s, striated muscle as 1566 m/s, and fat at 1479 m/s. The concentrations of muscle and fat in the scalp will not be known a-priori and may vary both between patients and within different regions of a single patient. Since the average speed of sound in scalp is not known 3 speed of sound values, 1480 m/s, 1525 m/s and 1570 m/s, were applied to the ultrasound data to generate sets of points to fit to the image based models.

While visually inspecting the ultrasound point sets it was noticed that there were a small number of points that seemed to be located above the point defined surface. The presence of outliers was not unexpected since they were present in the phantom study described previously [4]. To eliminate outlier points a distance filter was applied to the data. The distance threshold used to classify points as outliers was computed by transforming the ultrasound point sets by the fiducial marker registrations and looking at the distances between each point and the model. Looking across all of the data revealed that a threshold value of 5.0 mm excluded most of the outliers while preserving the majority of data points.

C. Image Model Generation

The CT data was transferred to a workstation and the imaging fiducial points were extracted using the method of Wang et al. [6] and the reference registration was computed. In visually reviewing the image data it was evident that in 3 cases (5, 6, 12) patient motion in the CT scanner was contributing to image artifacts and if the images were combined into a three dimensional volume without compensating for the motion large geometrical distortions would be present. To quantify and compensate for the patient motion a model of the N bar device attached to the CRW frame during imaging was constructed from a reference CT scan. This model was used to reformat the images and to partially compensate for patient motion between CT slices. In the case where severe artifacts due to patient motion were observed within a single image that image was discarded. None of the CT slices containing imaging fiducial marker caps contained this type of artifact. Figure 5.2 shows an example of the effect of patient motion on the original image and the results of the rectification.

Figure 5.2 (a) Image distortion caused by patient motion (b) reformatted image.

Although the rectified image has been corrected for inter-slice motion, it is not free of artifacts. In several places on the Nbars, CRW frame posts, and patient there are discontinuities. While unfortunate, this is to be expected. Since the patient was moving in the scanner, some areas of patient space were sampled more than once and others were not sampled at all. The voids represent regions of patient space where no imaging data is available.

In addition to the motion compensation it was helpful to mask out the tips of the CRW frame pins where they touched the skull to prevent the isointensity-based algorithm from including portions of the CRW frame in the model.

Both surface generation algorithms used in the phantom study [4] were used to create models of the outer skull surface. Guided trial and error was used to come up with a set of parameters that consistently produced a reasonable segmentation of the skull across the cases. The final parameters used in the Aboutanos method [1] are Threshold 1700, Intensity –1, Gradient +1, Window 20, Number of Points 200, and Displacement 8.0. The surface generated using this algorithm will be referred to as model A. For the Gueziec and Hummel isointensity-based algorithm [2] the values 1400, 1600, 1800 and 2000 were used to generate surfaces and will be referred to as models B, C, D, and E respectively.

Since the previous study on phantoms [4] suggested that simplification of the isosurface derived from tetrahedral decomposition has no detectable effect on registration accuracy, 30 iterations of the simplification algorithm were performed on each isosurface. Table 5.1 lists the image models by generation algorithm and model parameters.

Table 5.1 Image model descriptions

Model	Algorithm	Simplification
A	Aboutanos	0
B	G&H - 1400	30
C	G&H - 1600	30
D	G&H - 1800	30
E	G&H - 2000	30

D. Surface Registration

One of the first things that must be chosen in the ICP registration process [3] is an initializing transformation. Similarly to the previous experiment [4], the transformation chosen is the fiducial marker registration. Using this initial transformation should reveal to what degree the surface data through minimization of the surface registration error (SRE) pulls the registration away from its ideal value. This should give a good indication of the upper boundary of the method's performance. The registration solution in these cases will be a local minimum of SRE but may not be the global SRE minimum.

To further identify potential outliers, the mean μ, and standard deviation σ, of the distance between each data point and model are calculated at each iteration. The data points that

are greater than $\mu + 3\sigma$ away from the model are discarded from future iterations of the algorithm.

E. Validation

To validate the registrations, a set of target points was constructed by sampling the volume inside the skull. First the inner surface of the skull was segmented on the CT images of the individual patients. Then to reduce the total number of target points and taking account of the voxel dimensions only every fourth point in the in-plane dimensions of each segmented area was used to create the final set of about 113,000 target points (min 93664, max 157648). The target registration error at each of these points is computed by transforming the image point into physical space using the inverse of the fiducial marker registration and then transforming that point back to image space using the surface based registration. The Euclidean distance between the original image space point and the final image space point is computed. This distance is referred to as TREi and the root mean square statistic of the distances from all of the target points is referred to as the TRE.

Results and Discussion

A. Phase I

A total of 158 echoes were recorded from 6 volunteers. A sample signal is shown in Figure 5.3. Although this signal is noisier than those from the phantom, the scalp/skull interface can be clearly seen as the first major echo at approximately 13 μs. Also visible is a second echo at approximately 23 μs which represents a reverberation artifact.

The average TOF for the scalp/skull echo in the volunteer signals was 8.869 μs and the range was 5.81 μs to 12.81 μs. The average speed of sound should be somewhere between pure muscle, 1566 m/s, and pure fat, 1479 m/s. Using a speed of sound of 1566 m/s gives a scalp thickness range (via the TOF equation) of 4.549 mm to 10.03 mm with an average of 7.944 mm. Using a speed of sound equal to 1479 m/s gives a scalp thickness range of 4.296 mm to 9.473 mm with an average of 6.559 mm.

A minimum power threshold for detected echoes was desired to reject echoes from less echogenic sources than the scalp/skull interface. The power of the echoes in the volunteer data was examined and it was determined that a standard deviation filter threshold of 0.02250 Volts^2 was appropriate. This value represents an acceptable balance between rejecting too many echoes and therefore requiring a time consuming process of positioning of the transducer near perfectly and rejecting too few echoes.

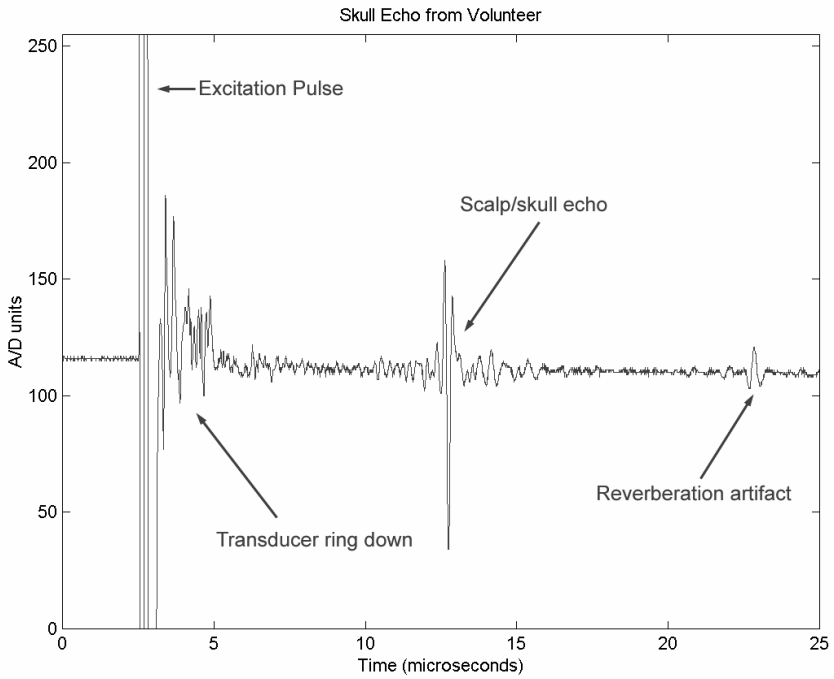

Figure 5.3 Sample ultrasound signal from a volunteer containing an echo from the interface between the scalp and outer surface of the skull.

B. Phase II

The fiducial registration errors reported as the rms statistic are shown in Table 5.2. The range is from 0.2402 (case 11) to 0.7271 (case 5). Based on previous experience with the fiducial marker system [9] these results indicate that the target registration error within the clinically relevant volume should be submillimetric.

Table 5.3 lists the number of data points collected for each case and the number of points remaining after the 5.0 mm outlier threshold was applied. Cases number 1, 4, and 7 have a smaller number of collected ultrasound points than the others. In the process of collecting data

for case number 1 it was realized that the echo power threshold, set from phase I data, was too high. This resulted in only 147 points being collected for this case. The echo power threshold was reduced for all subsequent cases. In case 4 the patient had a panic attack in the OR during

Table 5.2 Fiducial Registration Results

Case	FRE (mm)
1	0.4948
2	0.4282
3	0.3085
4	0.4860
5	0.7271
6	0.5614
7	0.5128
8	0.6556
9	0.3538
10	0.2402
11	0.4382
12	0.4528

Table 5.3 Number of data points used for registration

Case	Number of points collected	Points within outlier threshold
1	147	143
2	566	562
3	1086	1066
4	220	220
5	946	926
6	953	946
7	0	0
8	1301	1301
9	1280	1260
10	780	780
11	432	429
12	994	994

the surgical planning and data collection period and the procedure was canceled. This resulted in a decreased number of points collected and less coverage of the scalp than desired. Finally, during case 7 all of the surgical planning and data collection time was taken for patient setup and no ultrasound data was able to be collected.

Tables 5.4, 5.5, and 5.6 show the surface registration results for model A for speeds of sound equal to 1480 m/s, 1525 m/s and 1570 m/s respectively. The average TRE increases with speed of sound indicating that 1480 m/s is closest approximation to the true average speed of sound in scalp. This pattern holds true for all cases except numbers 4 and 12 where the relationship is reversed and cases 9 and 11 where the highest TRE statistics occur at 1525m/s.

Table 5.4 SRE and TRE results for model A with speed of sound equal 1480 m/s.

Case	SRE	max(TREi)	TRE		Case	SRE	max(TREi)	TRE
1	0.141	1.50118	1.14054		8	0.229049	2.12587	1.15897
2	0.284289	5.44524	2.74189		9	0.255352	3.52313	1.81345
3	0.214287	1.31353	0.86651		10	0.127927	3.32875	2.18639
4	0.153424	1.8745	1.24924		11	0.310479	2.36687	1.39584
5	0.266527	4.55468	2.17191		12	0.338103	1.69776	1.20041
6	0.359095	3.38895	1.76325					
					Mean	0.243594	2.829133	1.608036

Table 5.5 SRE and TRE results for model A with speed of sound equal 1525 m/s.

Case	SRE	max(TREi)	TRE		Case	SRE	max(TREi)	TRE
1	0.144545	1.50312	1.1881		8	0.268081	2.51003	1.42671
2	0.299967	5.77262	2.87111		9	0.230385	3.63315	1.92341
3	0.211799	1.3794	0.97910		10	0.131953	3.56182	2.33348
4	0.160094	1.68035	1.14229		11	0.204454	1.95553	1.4023
5	0.264424	4.95866	2.39968		12	0.342743	1.53418	1.06448
6	0.351564	3.49026	1.83708					
					Mean	0.237274	2.907193	1.687977

Table 5.6 SRE and TRE results for model A with speed of sound equal 1570 m/s.

Case	SRE	max(TREi)	TRE		Case	SRE	max(TREi)	TRE
1	0.160033	1.33457	1.22031		8	0.308058	3.96545	2.11146
2	0.314666	6.04384	2.99063		9	0.293056	3.20524	1.87078
3	0.181471	1.45766	1.13845		10	0.148073	4.06485	2.52506
4	0.170647	1.42009	1.01227		11	0.149746	2.12966	1.27365
5	0.270405	5.13965	2.53746		12	0.364456	1.45688	0.95419
6	0.357799	3.58776	1.93918					
					Mean	0.247128	3.073241	1.779404

Case 2 performed relatively poorly on this model regardless of speed of sound used for calculations.

Tables 5.7, 5.8, and 5.9 show the surface registration results for model B for speeds of sound equal to 1480 m/s, 1525 m/s and 1570 m/s respectively. As in model A, the average TRE increases with speed of sound further indicating that 1480 m/s is closest approximation to the

Table 5.7 SRE and TRE results for model B with speed of sound equal 1480 m/s.

Case	SRE	max(TREi)	TRE		Case	SRE	max(TREi)	TRE
1	0.171906	3.71384	2.38269		8	0.340796	5.36504	3.1453
2	0.369624	5.50563	3.04148		9	0.398944	4.19971	2.92395
3	0.228233	3.14828	2.42309		10	0.164015	4.20099	2.95272
4	0.271336	1.7001	1.40738		11	0.267417	2.15981	1.10854
5	0.318398	7.14788	3.3769		12	0.429803	3.04378	1.48944
6	0.373573	4.91551	3.02409					
					Mean	0.303095	4.100052	2.479598

Table 5.8 SRE and TRE results for model B with speed of sound equal 1525 m/s.

Case	SRE	max(TREi)	TRE		Case	SRE	max(TREi)	TRE
1	0.127425	3.97006	2.59876		8	0.389242	5.98596	3.51001
2	0.372421	7.72061	3.88687		9	0.501032	4.42737	3.13997
3	0.239959	3.18248	2.58703		10	0.191382	4.34564	3.09723
4	0.296366	1.91685	1.54893		11	0.253672	2.5857	1.27414
5	0.34518	7.83815	3.71133		12	0.468283	3.78628	1.91337
6	0.410323	5.29693	3.24712					
					Mean	0.326844	4.641457	2.774069

Table 5.9 SRE and TRE results for model B with speed of sound equal 1570 m/s.

Case	SRE	max(TREi)	TRE		Case	SRE	max(TREi)	TRE
1	0.144141	4.7719	2.86605		8	0.438853	6.78059	3.94653
2	0.344403	8.04408	4.10331		9	0.576954	4.71849	3.25707
3	0.222309	4.47218	2.91936		10	0.184209	4.78528	3.36285
4	0.337463	2.19179	1.74227		11	0.264494	2.945	1.48398
5	0.383765	8.1542	3.86298		12	0.586913	5.29017	2.50747
6	0.475962	5.35833	3.42665					
					Mean	0.359951	5.228365	3.043502

true average speed of sound in scalp. Case numbers 11 and 4 performed relatively well on this model. The average and all of the individual case TREs except case 11 at 1480m/s and 1525 m/s for model B are higher than their corresponding TREs for model A.

Tables 5.10, 5.11, and 5.12 show the surface registration results for model C for speeds of sound equal to 1480 m/s, 1525 m/s and 1570 m/s respectively. As in models A and B, the

Table 5.10 SRE and TRE results for model C with speed of sound equal 1480 m/s.

Case	SRE	max(TREi)	TRE		Case	SRE	max(TREi)	TRE
1	0.17877	1.96033	1.57413		8	0.275337	3.91378	2.18545
2	0.222222	4.7788	2.50518		9	0.266371	4.02418	2.30754
3	0.213452	2.38423	1.69624		10	0.118442	3.57449	2.47612
4	0.173694	1.89738	1.12147		11	0.31752	1.89632	1.03288
5	0.271707	4.89075	2.35975		12	0.322807	1.37841	0.71809
6	0.326575	2.35053	1.92702					
					Mean	0.244263	3.004473	1.809443

Table 5.11 SRE and TRE results for model C with speed of sound equal 1525 m/s.

Case	SRE	max(TREi)	TRE		Case	SRE	max(TREi)	TRE
1	0.167003	2.39244	1.83371		8	0.334422	4.69721	2.5833
2	0.30610	4.84314	2.59348		9	0.353313	4.3502	2.53901
3	0.231881	2.14714	1.8046		10	0.122374	3.84668	2.66255
4	0.194382	2.17579	1.23846		11	0.26137	1.95019	1.06238
5	0.302735	5.36717	2.5737		12	0.348241	1.70194	0.884225
6	0.344942	2.83541	2.14877					
					Mean	0.269706	3.300665	1.993108

Table 5.12 SRE and TRE results for model C with speed of sound equal 1570 m/s.

Case	SRE	max(TREi)	TRE		Case	SRE	max(TREi)	TRE
1	0.140525	3.27116	2.08617		8	0.354841	6.05358	3.21196
2	0.366709	6.21839	3.1466		9	0.454109	4.62488	2.75026
3	0.234037	2.65541	2.03889		10	0.167578	3.98896	2.74582
4	0.220171	2.20566	1.28257		11	0.244883	2.14138	1.10764
5	0.325739	6.26559	2.98863		12	0.388311	1.87626	1.02532
6	0.399497	3.6034	2.4402					
					Mean	0.299673	3.900425	2.256733

average TRE increases with speed of sound. Case 2 did relatively poorly on this model and cases 11 and 12 did relatively well. The average TREs were lower than in model B, but still higher than model A.

Tables 5.13, 5.14, and 5.15 show the surface registration results for model D for speeds of sound equal to 1480 m/s, 1525 m/s and 1570 m/s respectively. Unlike models A, B, and C the

Table 5.13 SRE and TRE results for model D with speed of sound equal 1480 m/s.

Case	SRE	max(TREi)	TRE		Case	SRE	max(TREi)	TRE
1	0.153476	1.94072	1.26904		8	0.201947	3.49866	1.74151
2	0.232083	3.9988	2.08476		9	0.268394	3.63936	1.92706
3	0.219466	2.8105	1.44962		10	0.132304	2.7545	1.97549
4	0.149392	1.99316	1.21659		11	0.22622	3.89244	2.09774
5	0.269106	3.44192	1.71102		12	0.287902	1.85809	0.96074
6	0.380598	1.90928	1.43744					
					Mean	0.229172	2.885221	1.624638

Table 5.14 SRE and TRE results for model D with speed of sound equal 1525 m/s.

Case	SRE	max(TREi)	TRE		Case	SRE	max(TREi)	TRE
1	0.150582	1.67391	1.24293		8	0.231546	4.55545	2.24582
2	0.291983	3.90068	2.09183		9	0.300444	2.73828	1.62287
3	0.20465	1.75181	1.1956		10	0.132432	3.27485	2.23819
4	0.189235	0.89902	0.75894		11	0.233018	3.7536	1.95473
5	0.304934	2.84804	1.41343		12	0.32158	1.92202	0.95800
6	0.359903	1.87881	1.55515					
					Mean	0.247301	2.654225	1.570682

Table 5.15 SRE and TRE results for model D with speed of sound equal 1570 m/s.

Case	SRE	max(TREi)	TRE		Case	SRE	max(TREi)	TRE
1	0.157795	2.34864	1.47589		8	0.282595	5.25507	2.62302
2	0.333618	4.16339	2.23748		9	0.363389	3.12652	1.85118
3	0.196565	1.89855	1.36222		10	0.144503	3.51154	2.40105
4	0.214286	1.51849	0.90111		11	0.214354	3.74132	1.77025
5	0.29667	4.65046	2.28859		12	0.365185	1.90245	0.96315
6	0.380942	2.3263	1.74752					
					Mean	0.268173	3.131157	1.78377

minimum average TRE was found at a speed of sound of 1525 m/s. Cases 4 and 12 did relatively well across the range of speed of sound tested for this model. The average TREs were approximately the same as model A and lower than models B and C.

Tables 5.16, 5.17, and 5.18 show the surface registration results for model E for speeds of sound equal to 1480 m/s, 1525 m/s and 1570 m/s respectively. Similarly to model D, the

Table 5.16 SRE and TRE results for model E with speed of sound equal 1480 m/s.

Case	SRE	max(TREi)	TRE		Case	SRE	max(TREi)	TRE
1	0.233982	1.71659	1.02258		8	0.169847	2.70106	1.28594
2	0.176848	3.33376	1.87128		9	0.366042	1.13859	0.77643
3	0.26525	2.03994	1.06369		10	0.158321	2.75118	1.86047
4	0.164858	2.41196	1.42924		11	0.368078	5.36227	2.54959
5	0.318661	1.4524	0.83570		12	0.28197	2.06946	1.3054
6	0.34721	3.49944	1.82547					
					Mean	0.259188	2.588786	1.438709

Table 5.17 SRE and TRE results for model E with speed of sound equal 1525 m/s.

Case	SRE	max(TREi)	TRE		Case	SRE	max(TREi)	TRE
1	0.161042	2.89349	1.7618		8	0.219543	2.92862	1.42421
2	0.311708	2.41488	1.23483		9	0.310298	1.67909	1.08877
3	0.230632	2.32095	1.21175		10	0.165848	3.0255	1.97872
4	0.16135	2.33077	1.38231		11	0.299253	2.95224	1.80395
5	0.311679	1.88101	0.914902		12	0.284349	1.72629	1.14301
6	0.36495	1.37218	1.12457					
					Mean	0.256423	2.320456	1.369893

Table 5.18 SRE and TRE results for model E with speed of sound equal 1570 m/s.

Case	SRE	max(TREi)	TRE		Case	SRE	max(TREi)	TRE
1	0.20089	1.9024	1.20067		8	0.27686	3.47832	1.72455
2	0.413992	3.04337	1.50316		9	0.321915	2.04443	1.36949
3	0.228159	2.40808	1.29176		10	0.175472	3.52959	2.22671
4	0.16458	2.30451	1.37839		11	0.293308	2.96207	1.66688
5	0.316454	2.40432	1.08437		12	0.30477	1.61183	1.02651
6	0.358295	1.52517	1.27084					
					Mean	0.2777	2.474008	1.431212

minimum average TRE occurs at a speed of sound equal to 1525 m/s. Case 5 did relatively well across speed of sounds for this model. The average TREs were lower than the other models.

Figure 5.4 shows the relative performance of all of the models at all values of the speed of sound. The figure includes the 95% confidence intervals for the mean value of TRE.

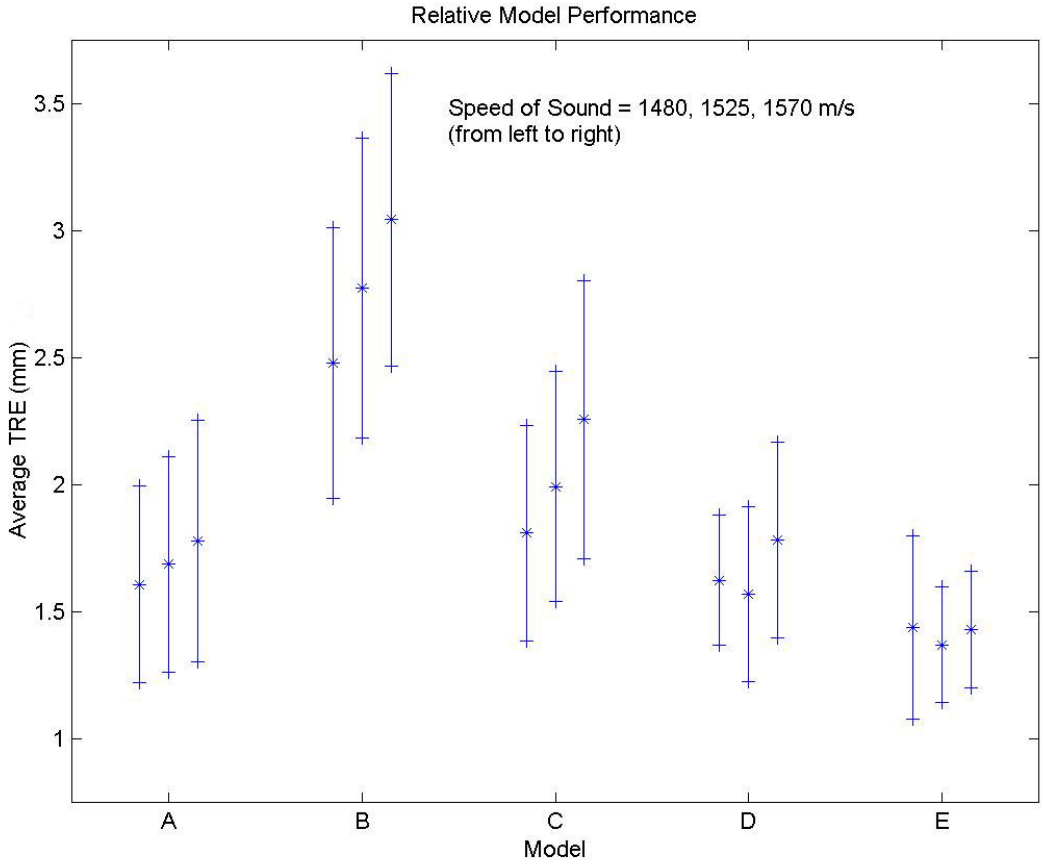

Figure 5.4 Average target registration error for model A (deformable model based) and models B-E (isointensity based) for all values of speed of sound in scalp. Also shown are the 95% confidence limits of the mean.

In the phantom experiment [4] a clear relationship was demonstrated between the value of the intensity parameter used to generate the isointensity surface and the speed of sound. That is, as the intensity was increased (effectively eroding the surface) and the speed of sound was increased (pushing the data point set into the head) the TRE stayed consistently low. In this work the sampling of the intensity and speed of sound parameters were not as fine and only

minimal evidence of this pattern exists. As the intensity value is increased from model B to model E the minimum average TRE within the model transitions from 1480 m/s to 1525 m/s.

Also, at all values of speed of sound an increase in the intensity parameter (moving from model B to model E) lead to a decrease in average TRE.

Looking across all of the models and at all of the speed of sound values, cases 4 and 12 did relatively well. As previously stated, it is somewhat surprising to see case 4 perform this well given the complication during data collection. Conversely, across all models and at all speed of sound values cases 2, 8, and 10 performed relatively poorly. There does not appear to be an obvious reason for the differences in relative performance.

Figure 5.5 shows the average residual error for all of the models at all values of the speed of sound. The figure includes the 95% confidence intervals for the mean value of SRE. Similarly to Figure 5.4, model B appears to have higher errors than the other models. The combination of high SRE and high TRE indicates that the intensity parameter used to generate the isointensity surface may have been too low to produce accurate registrations.

In a previous study [4] it was shown that the minimum value of SRE when graphed against variations in speed of sound does not coincide with the minimum value of TRE when graphed against speed of sound. While the coincidence of the two minima may not be exact it may still be possible to realize TRE improvement by constructing a modified version of the ICP algorithm that includes a constrained optimization of speed of sound. Comparing the speed of sound value at which the minimum TRE occurs (in Figure 5.4) with the speed of sound value at which the minimum SRE occurs (in Figure 5.5) we see that the minima occur at the same speed of sound in three of the five models (at 1480m/s for models B and C, 1525 for model E). The speed of sound sampling was not granular enough to draw conclusions from this study and the affect on TRE of including speed of sound in the optimization algorithm remains an open question.

To determine what effect, if any, the number of ultrasound data points used in the surface registration has on TRE, the correlation coefficients between TRE and number of data points were computed and are listed in Table 5.19. The values range from 0.519113 to -0.51014 which indicates a lack of a significant relationship between the number of points used over the range 143-1301 used in this experiment.

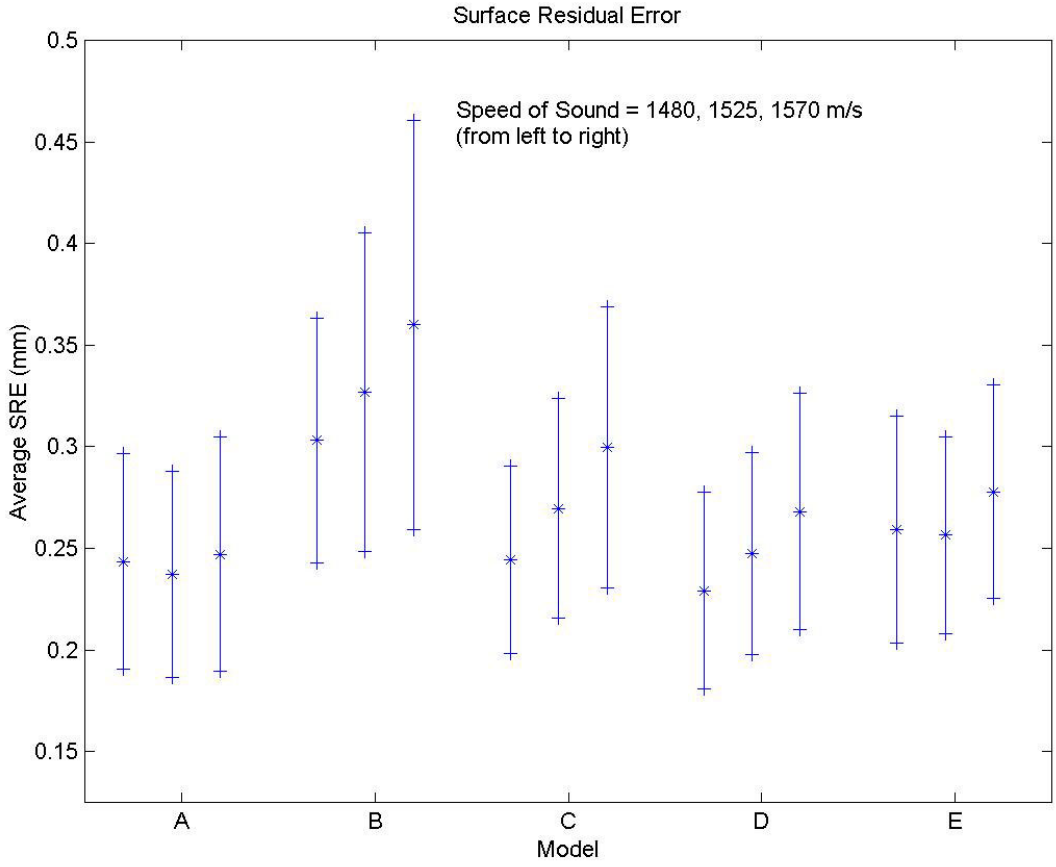

Figure 5.5 Average surface registration error for all models and values of speed of sound in scalp. Shown in brackets are the 95% confidence limits.

Table 5.19 Correlation coefficients between TRE and number of data points.

Model / Speed of Sound	**A**	**B**	**C**	**D**	**E**
1480 m/s	-0.00025	0.500718	0.370703	0.121241	-0.36115
1525 m/s	0.094248	0.466403	0.415456	0.25987	-0.51014
1570 m/s	0.247849	0.519113	0.437521	0.369376	-0.00186

The ultrasound points collected for each case in this study have similar areas of coverage. It is expected that TRE would increase if the area of coverage were significantly decreased or limited to highly symmetric areas of the skull.

Given the lack of variation of TRE between 2 mm and 4 mm CT slice thickness in the previous phantom experiment [4] it is expected that there would not be a significant difference in the results from case 11, in which 2 mm CT slices were acquired. This expectation holds true in the patient data where the relative results of case 11 are mixed. Case 11 preformed relatively well on all speeds of sound in the lower values of the intensity parameter (models B and C), but performed relatively poorly on some speed of sound values in higher intensity parameter surfaces (model D at 1480 m/s and model E at 1480 m/s and 1525 m/s).

In this study TREs ranged between 0.7 mm and 4.1 mm when compared to the gold standard registration. Although this level of error is suitable for some applications, e.g. the removal of a meningioma, an increased level of accuracy is desired for procedures that target deeper structures, such as thalamic stimulator implantation. Bucholz et al. [10] report a mean error of 2.0 mm with standard deviation of 0.6 mm for point based registration using scalp attached fiducials and a mean error of 3.2 mm with standard deviation of 1.2 mm for scalp based surface registration in a cadaver. Similarly, Sipos et al. [11] report a mean error of 2.51 mm for point based registration using scalp attached fiducials and a mean error of 3.03 mm for surface registration using the scalp. These results indicate that surface registration using the outer surface of the skull can be more accurate than both point based registration using scalp markers and surface registration using the scalp.

The registration errors presented in Tables 5.4 through 5.18 are only one component of the total error in a surgical navigation system. Other sources of error that contribute to overall application error include motion of the patient with respect to the localization system and motion of the brain with respect to the skull. For cases involving stereotactic frames this would be motion of the patient with respect to the frame between imaging and the procedure. For frameless navigation systems this error would be represented by motion of the patient with respect to a sensor or reference object. Additionally, studies have shown that the brain pulsates [12] and may shift due to gravity, pharmaceuticals, and removal of tissue or CSF [13]. Brain shift has been measured with both surgical guidance system [14] and an intraventional MRI system [15]. Correction of preoperative images for brain motion using intraoperative imaging remains an active research topic.

Conclusion

This study has shown that it is possible to perform physical space to image space registration using the outer surface of the skull as identified in CT imaging and localized using a spatially tracked A-mode ultrasound transducer. Similar to a previous study using this registration technique on a phantom [4] no large differences between the TRE of the image models and point sets was observed. The TREs ranged from 0.7 mm to 4.1 mm when compared to the fiducial marker based gold standard registration. However, since the gold standard was measured, it has its own estimated error of approximately 0.7 mm [9] that must be taken into account.

No strong correlations were observed between the number of data points used in the registration algorithm and the TRE over the range of points collected in this study. However, it is expected that TRE will correlate negatively with the range of surface area over which ultrasonic points are collected. That is the TRE is expected to increase as the area from which ultrasound points are acquired is decreased.

Initializing the surface registration algorithm with the fiducial marker solution, i.e. the ideal initializing transformation, will not be possible in practice. Further work remains to be completed to determine how registration performance decreases as the misalignment in the initializing transformation increases.

Acknowledgement

The authors would like to acknowledge the invaluable help and support provided by Dr. Peter E. Konrad.

References

[1] G. B. Aboutanos, *Image-Based Deformable Models for 3-D Automatic Segmentation of the Brain*, Ph.D. dissertation, Vanderbilt University, 1996.

[2] A. Gueziec and R. Hummel, "Exploiting Triangulated Surface Extraction Using Tetrahedral Decomposition", *IEEE Transactions on Visualization and Computer Graphics*, vol. 1, no. 4, pp. 328-342, 1995.

[3] P. J. Besl, and N. D. McKay, “A method for registration of 3D shapes”, *IEEE Transactions on Pattern Analysis and Machine Intelligence*, vol. 14, no**.** pp. 239-256, 1992.

[4] W. A. Bass, *Patient-Image Registration using A-mode ultrasound localization of features*, Ph.D. dissertation, Vanderbilt University, Nashville, TN, 2003.

[5] S. Schreiner, R. L. Galloway, Jr., W. A. Bass, and D. M. Muratore "An Ultrasonic Approach to Localization of Fiducial Markers for Interactive, Image-Guided Neurosurgery--Part II: Implementation and Automation," *IEEE Transactions on Biomedical Engineering*, vol. 45, pp. 631-641, 1998.

[6] M. Y. Wang, C. R. Maurer, Jr., J. M. Fitzpatrick, and R. J. Maciunas, “An Automatic Technique for Finding and Localizing Externally Attached Markers in CT and MR Volume Images of the Head,” *IEEE Transactions on Biomedical Engineering*, vol. 43, pp. 627-637, 1996.

[7] K. S. Arun, T. S. Huang, and S. D. Blostein, “Least-Squares Fitting of Two 3-D Point Sets,” *IEEE Transaction on Pattern Analysis and Machine Intelligence*, vol. 9, pp. 698-700, 1987.

[8] D. Christensen, *Ultrasonic Bioinstrumentation*. New York, NY: John Wiley & Sons, 1988.

[9] C. R. Maurer, Jr., J. M. Fitzpatrick, M. Y. Wang, R. L. Galloway, Jr., R. J. Maciunas, and G. S. Allen, “Registration of Head Volume Images Using Implantable Fiducial Markers”, *IEEE Transactions on Medical Imaging*, vol. 16, pp 447-462, 1997.

[10] R. D. Bucholz, T. Forget, W. R. Macneil, J. N. Duff, S. A. Berger, L. L. McDurmont, C. Baumann and J. Standeven, “A Cadaver Study of the Effects of Skin Flexibility on the Accuracy of Stereotactic Registrations Performed with Scalp Mounted Fiducials and Contour Matching,” *AANS National Conference*, New Orleans, LA, 1999.

[11] E. P. Sipos, S. A. Tebo, S. J. Zinreich, D. M. Long, H. Brem, “In vivo accuracy testing and clinical experience with the ISG Viewing Wand,” Neurosurgery, vol. 39, pp. 194-204, 1996.

[12] B. P. Poncelet, V. J. Wedeen, R. M. Weisskoff, and M. S. Cohen, “Brain parenchyma motion: Measurement with cine echoplanar MR imaging,” *Radiology*, vol. 185, pp. 645–651, 1992.

[13] J. G. Golfinos, B. C. Fitzpatrick, L. R. Smith, and R. F. Spetzler, “Clinical use of a frameless stereotactic arm: Results of 325 cases,” *Journal of Neurosurgery*, vol. 83, pp. 197–205, 1995.

[14] D. L. G. Hill, C. R. Maurer, Jr., R. J. Maciunas, J. A. Barwise, J. M. Fitzpatrick, and M. Y. Wang, "Measurement of intraoperative brain surface deformation under a craniotomy," *Neurosurgery*, vol. 43, pp. 514–526, 1998.

[15] C. R. Maurer, Jr., D. L. G. Hill, A. J. Martin, H. Liu, M. McCue, D. Rueckert, D. Lloret, W. A. Hall, R. E. Maxwell, D. J. Hawkes, and C. L. Truwit, "Investigation of Intraoperative Brain Deformation Using a 1.5-T Interventional MR System: Preliminary Results", *IEEE Transactions on Medical Imaging*, vol. 17, pp. 817-825, 1998.

CHAPTER VI

SUMMARY

The objective of this dissertation is to investigate the accuracy of point and surface based image to physical space registration performed using a spatially tracked A-mode ultrasound transducer to localize features and the applicability of these techniques for use in IIGS. This objective was accomplished by several means. An optically tracked A-mode ultrasound localization system was constructed and calibrated.

In the first experiment the ultrasonic system's accuracy was examined when used to transcutaneously localize simulated bone implanted fiducial markers. The relationship between the number of candidate signals used to localize the fiducial markers and localization accuracy was determined. Using ten candidate signals the ultrasonic system is capable of localizing transcutaneous fiducials with an error of 0.5 mm when compared to the computed localization of the transcutaneous fiducial calculated from direct localization of two surrounding external fiducials. The ultrasonic system was judged to be clinically acceptable based on this level of transcutaneous fiducial marker localization accuracy, the time requirements for transcutaneous fiducial marker localization, and the ease of operation.

The ultrasonic localization system was modified for use in localizing the outer surface of the skull. A second experiment was performed with a phantom to investigate the feasibility of using a surface based registration to match the ultrasonic data to a CT based model of the outer surface of the skull. Two segmentation techniques were used, one based on deformable models and the other on isointensity surfaces and six image models were examined. The effect on registration errors from changes in the intensity parameter of the isointensity segmentation algorithm and variations in the speed of sound in gelatin were examined. Target registration error was found to depend on both the speed of sound in gelatin and the intensity parameter and varied between approximately 1 mm and 3.5 mm. Surface registration error was found to depend primarily on the speed of sound in gelatin and varied between 0.2 and 0.6 mm. The ramifications of surface simplification (performed on the isointensity surfaces) and the slice resolution of the CT volumes were examined and found not to substantially affect registration errors. Surface registration errors were computed for translational and rotational deviations from

the gold standard registration and the results indicate that the registration technique should be able to successfully accommodate moderate levels of misalignment. These results justified the expansion of this investigation to human subjects.

A third experiment was performed on a population of patients undergoing a neurosurgical procedure. The ultrasonic localization system was reconfigured and enhanced to synchronize the acquisition of ultrasonic and optical information. Ultrasonic data and CT images were acquired from twelve patients. When detected, patient motion in the CT images was corrected using the Nbar system of the CRW stereotactic frame. The surface registration and target registration results were evaluated for five image models using three different speed of sound values corresponding to the speed of sound in the tissue components of human scalp. The target registration errors varied from 0.7 mm to 4.1 mm when compared to the gold standard, fiducial marker registration. The correlation between the number of ultrasonic points used in the surface registration algorithm and the surface registration error was evaluated and found to be not significant for the range of data points collected.

These three experiments have demonstrated that a spatially tracked A-mode ultrasound transducer is capable of localizing both point and surface features that can be matched with corresponding point and surface features derived from CT images and used for registration in IIGS applications.

Future Work

The research described in this dissertation can be enhanced and extended in a number of directions. Although it is not anticipated, should the development of permanently implantable fiducial markers continue to the point of human trials, it is likely that the software of the ultrasonic localization system will need to be refined to accommodate the differences between fiducial marker analogs and the actual fiducial markers and similarly the differences between scalp analog and actual human scalp.

Work remains to be done to fully characterize the expected accuracy of the surface registration technique described in this research. Specifically the effect of misalignment of the initializing transformation on the registration error is not well known. Qualitative knowledge of the technique's sensitivity to initial misalignment will help determine the technique best suited for initializing the registration (e.g. interactive, anatomic point-based, other).

The image and physical space data sets collected may be used to investigate additional image models and registration techniques including level-set segmentation techniques, optimization of the speed of sound in scalp in the registration algorithm, the effects of further restricting the number of ultrasonic points, and the level of accuracy deterioration from reducing the area of scalp coverage of the ultrasonic points.

Automation of the registration techniques described within this research and integration within an IIGS system would increase the usefulness of the system for further researchers. Integration within such a system would allow the techniques to be used in conjunction with other methods (such as intraoperative updates to registrations and image volumes to account for brain motion) to lower the total application error of the system.

Finally, further improvements to the ultrasonic localization device itself may prove useful. Revising the design to place IREDs closer to the transducer will increase the point localization accuracy of the device and may lead to more accurate feature localizations. Also, coupling the ultrasonic transducer with other spatial tracking systems may be useful in the future.

Research Considerations

A. Protection of Research Subjects.

Since human subjects were used in this research, all techniques were documented and approved by the Institutional Review Board (IRB) of the Vanderbilt University Medical Center. Informed consent was obtained from all volunteers and patients prior to the respective procedures and their confidentiality has been protected. Patient identification was removed from all medical images used in this research.

B. Societal Implication.

Permanently implantable fiducial markers provide advantages over temporary bone implanted markers including their use in serial image registration in the monitoring of therapy efficacy and patient comfort. The ultrasonic localization technique developed in this research provides the capability needed for image space to physical space registrations. This capability allows the markers to be used in image guided procedures and therapies such as stereotactic biopsy and fractionated radiotherapy.

Surface registration based on the outer surface of the skull is less accurate than point based registration using bone implanted fiducial markers. However, this technique may provide an alternative to bone implanted fiducial markers when such markers are not available or when the specific application accuracy requirements do not warrant the use of invasive registration techniques.

BIBLIOGRAPHY

G. B. Aboutanos, "Image-Based Deformable Models for 3-D Automatic Segmentation of the Brain," Ph.D. dissertation, Vanderbilt University, Nashville, TN, 1996.

K. S. Arun, T. S. Huang, and S. D. Blostein, "Least-Squares Fitting of Two 3-D Point Sets," *IEEE Transactions on Pattern Analysis and Machine Intelligence*, vol. 9, pp. 698-700, 1987.

N. Ayache, P. Cinquin, I. Cohen, L. Cohen, F. Leitner, and O. Monga, "Segmentation of Complex Three-Dimensional Medical Objects: A Challenge and a Requirement for Computer-Assisted Surgery Planning and Performance," in *Computer-Integrated Surgery: Technology and Clinical Applications*, R. H. Taylor, S. Lavallee, G. Burdea, C., and R. Mosges, Eds. Cambridge, Massachusetts: The MIT Press, 1996, pp. 59-74.

J. M. Balter, C. A. Pelizzari, and G. T. Y. Chen, "Correlation of projection radiographs in radiation therapy using open curve segments and points," *Medical Physics*, vol. 19, pp. 329-334, 1992.

W. A. Bass, "Integration of angiographic data into an interactive, image-guided neurosurgical system," M.S. thesis, Vanderbilt University, Nashville, TN, 1996.

W. A. Bass, "Patient-Image Registration using A-mode ultrasound localization of features", Ph.D. dissertation, Vanderbilt University, Nashville, TN, 2003.

W. A. Bass, R. L. Galloway, Jr., C. R. Maurer, Jr., "Surface-based registration of physical space with CT images using A-mode ultrasound localization of the skull," *Medical Imaging 1998: Image Display, Proc. SPIE*, vol. 3335, pp. 228-238, 1998.

P. J. Besl and N. D. McKay, "A method for registration of 3D shapes," *IEEE Transactions on Pattern Analysis and Machine Intelligence*, vol. 14, pp. 239-256, 1992.

B. K. Brodwater, D. W. Roberts, T. Nakajima, E. M. Friets, and J. W. Strohbehn, "Extracranial application of the frameless stereotactic operating microscope: experience with lumbar spine," *Neurosurgery*, vol. 32, pp. 209-213, 1993.

R. D. Bucholz, T. Forget, W. R. Macneil, J. N. Duff, S. A. Berger, L. L. McDurmont, C. Baumann and J. Standeven, "A Cadaver Study of the Effects of Skin Flexibility on the Accuracy of Stereotactic Registrations Performed with Scalp Mounted Fiducials and Contour Matching," *AANS National Conference*, New Orleans, LA, 1999.

R. D. Bucholz and K. R. Smith, "A comparison of Sonic Digitizers Versus Light Emitting Diode-Based Localization," in *Interactive Image-Guided Neurosurgery*, R. J. Maciunas, Ed.: AANS, 1993, pp. 179-200.

R. L. Carrau, C. H. Snyderman, H. B. Curtin, and J. L. Weissman, “Computer assisted frontal sinusotomy,” *Otolaryngology*, vol. 111, pp. 727-732, 1994.

H. Chang and J. M. Fitzpatrick, “A Technique for Accurate Magnetic Resonance Imaging in the Presence of Field Inhomogeneities,” *IEEE Transactions on Medical Imaging*, vol. 11, pp. 319-329, 1992.

D. Christensen, *Ultrasonic Bioinstrumentation*. New York, NY: John Wiley & Sons, 1988.

A. C. F. Colchester, J. Zhao, N. Dorward, G. Subsol, and D. G. T. Thomas, “Comparison of Phantom Target Localisation by Frame-Based Stereotaxy and by the VISLAN System,” presented at CVRMed-MRCAS, Grenoble, France, 1997.

R. O. Duda and P. E. Hart, *Pattern Classification and Scene Analysi*s. New York: Wiley, 1973.

C. A. Edwards, “A real-time, interactive stereotactic system,” Ph.D. dissertation, Vanderbilt University, Nashville, TN, 1991.

P. A. van den Elsen, “Multimodality Matching of Brain Images,” in *Department of Radiology and Nuclear Medicine*. Utrecht, the Netherlands: Utrecht University, 1993, pp. 168.

J. L. Farrell and J. C. Stuelpnagel, "Problem 65-1: A least squares estimate of satellite attitude," SIAM Reviews, vol. 8, pp. 384-386, 1966.

O. D. Faugeras and M. Hebert, “The representation, recognition, and locating of 3D objects,” *The International Journal of Robotics Research*, vol. 5, pp. 27–52, 1986.

J. M. Fitzpatrick, D. L. G. Hill, and C. R. Maurer, Jr. Image Registration. In: *Handbook of Medical Imaging, Volume 2: Medical Image Processing and Analysis*, eds. M. Sonka and J. M. Fitzpatrick. Bellingham WA: SPIE Press, 2000. pp. 447-513.

J. M. Fitzpatrick and J. B. West, “The distribution of Target Registration Error in Rigid-Body Point-Based Registration,” *IEEE Transactions on Medical Imaging*, vol. 20, pp. 917-927, 2001.

W. Freysinger, A. R. Gunkel, A. Martin, R. J. Bale, M. Vogele, and W. F. Thumfart, “Advancing ear, nose, and throat computer-assisted surgery with the arm-based ISG viewing wand: the stereotactic suction tube,” *Laryngoscope*, vol. 107, pp. 690-693, 1997.

E. M. Friets, J. W. Strohbehn, J. F. Hatch, and D. W. Roberts, “A frameless stereotactic microscope for neurosurgery,” *IEEE Transactions on Biomedical Engineering*, vol. 36, pp. 608-617, 1989.

R. L. Galloway, W. A. Bass, J. D. Stefansic, and R. J. Maciunas, “Incorporation of vascular information into interactive, image-guided surgery,” in *Proc. SPIE Medical Imaging 199*6, vol. 2707, Feb. 1996.

R. L. Galloway, C. A. Edwards, J. G. Thomas, and R. J. Maciunas, “Image display and surgical visualization in interactive, image-guided neurosurgery,” *Optical Engineerin*g, vol. 32, pp. 1955–1962, 1993.

R. L. Galloway, C. A. Edwards, J. G. Thomas, S. Schreiner, and R.J. Maciunas, “A new device for interactive, image-guided surgery,” in *Proc. SPIE Medical Imaging* V, vol. 1444, Feb. 1991, pp. 9–18.

R. L. Galloway, J. T. Lewis, S. Schreiner, T. Stanley, and R. Maciunas, “A new interactive image-guided surgical device,” in *Proceedings of the Annual International Conference of the IEEE Engineering and Biology Society*, Oct. 1992.

R. L. Galloway, Jr., R. J. Maciunas, W. A. Bass, and W. J. Carpini, “Optical localization for interactive, image-guided neurosurgery”, *Medical Imaging*, Y. Kim, Ed., vol. 2164, pp. 137-145, 1994.

R. L. Galloway, Jr., R. J. Maciunas, and C. A. Edwards, “Interactive Image-Guided Neurosurgery,” *IEEE Transactions on Biomedical Engineering*, vol. 39, pp. 1226-1231, 1992.

J. M. Galvin, K. Han, M. E. Noz, T. Vaccaro, J. Cooper, D. P. Reddy, and G. Q. Maguire, Jr., “Warping CT scans from nontreatment to treatment position,” *Radiation Oncology Investigations*, vol. 5, pp. 206-12, 1997.

P. L. Gleason, R. Kikinis, D. Altobelli, W. Wells, E. Alexander, III, P. M. Black, and F. Jolesz, “Video registration virtual reality for nonlinkage stereotactic surgery,” *Stereotactic & Functional Neurosurgery*, vol. 63, pp. 139-143, 1994.

J. G. Golfinos, B. C. Fitzpatrick, L. R. Smith, and R. F. Spetzler, “Clinical use of a frameless stereotactic arm: results of 325 cases,” *Journal of Neurosurgery*, vol. 83, pp. 197-205, 1995.

G. Golub and C. van Loan, *Matrix Computations*. Baltimore, MD: Johns Hopkins Univ. Press, 1983.

B. L. Guthrie and J. R. Adler, Jr., “Computer assisted preoperative planning, interactive surgery, and frameless stereotaxy,” *Clinical Neurosurgery*, vol. 38, pp. 112-131, 1992.

A. Gueziec, and R. Hummel, “Exploiting Triangulated Surface Extraction Using Tetrahedral Decomposition”, *IEEE Transactions on Visualization and Computer Graphics*. Vol. 1, No. 4, pp. 328-342, 1995.

J. V. Hajnal, D. L. G Hill, and D. J. Hawkes. *Medical Image Registration*, CRC Press: 2001.

A. Hamadeh, P. Sautot, S. Lavallee, and P. Cinquin, “Towards automatic registration between CT and X-ray images: cooperation between 3D/2D registration and 2D edge detection,” presented at Medical Robotics and Computer Assisted Surgery, Baltimore, MD, 1995.

D. Haynor, A. W. Borning, B. A. Griffin, J. P. Jacky, I. J. Kalet, and W. P. Shuman, "Radiotherapy Planning: Direct Tumor Location on Simulation and Port Films Using CT," *Radiology*, vol. 158, pp. 537-540, 1986.

M. P. Heilbrun, S. Koehler, P. McDonald, W. Peters, V. Sieminov, and C. Wiker, "Implementation of a machine vision method for stereotactic localization and guidance," in *Interactive Image-Guided Neurosurgery*, R. J. Maciunas, Ed.: AANS, 1993, pp. 169-177.

J. L. Herring and B. M. Dawant, "Automatic Lumbar Vertebral Identification Using Surface-Based Registration," *Journal of Biomedical Informatics*, vol. 34, pp. 74-84, 2001.

C. R. Hill, *Physical Principles of Medical Ultrasonic*s. New York: Wiley, 1986.
D. L. G. Hill, C. R. Maurer, Jr., R. J. Maciunas, J. A. Barwise, J. M. Fitzpatrick, and M. Y. Wang, "Measurement of intraoperative brain surface deformation under a craniotomy," *Neurosurgery*, vol. 43, pp. 514–526, 1998.

H. Hirschberg, "Implementation of a stereotactic microscope using an optically coupled tracking system," *Stereotactic & Functional Neurosurgery*, vol. 66, pp. 96-101, 1996.

B. K. P. Horn, "Closed-form solution of absolute orientation using orthonormal matrices," *Journal of the Optical Society of America A.*, vol. 5, pp. 1127-1135, 1987.

B. K. P. Horn, "Closed-form solution of absolute orientation using unit quaternions," *Journal of the Optical Society of America A.*, vol. 4, pp. 629-642, 1987.

J. R. Hurley and R. B. Cattell, "The procrustes program: Producing direct rotation to test a hypothesized factor structure," *Behavioral Science*, vol. 7, pp. 258–262, 1962.

P. Jannin, J. M. Fitzpatrick, D. J. Hawkws, X. Pennec, R. Shahidl, M. W. Vannier, "Validation of medical image processing in image-guided therapy", *IEEE Transactions on Medical Imaging*, vol. 21, pp. 1445-1449, 2002.

A. Kato, T. Yoshimine, T. Hayakawa, Y. Tomita, T. Ikeda, M. Mitomo, K. Harada, and H. Mogami, "A frameless, armless navigation system for computer-assisted neurosurgery," *Journal of Neurosurgery*, vol. 74, pp. 845-849, 1991.

J. Koivukangas, Y. Louhisalmi, J. Alakuijala, and J. Oikarinen, "Ultrasound controlled neuronavigator-guided brain surgery," *Journal of Neurosurgery*, vol. 79, pp. 36-42, 1993.

Y. Kosugi, E. Watanabe, J. Goto, T. Watanabe, S. Yoshimoto, K. Takakura, and J. Ikebe, "An articulated neurosurgical navigation system using MRI and CT images," *IEEE Transactions on Biomedical Engineering*, vol. 35, pp. 147-152, 1988.

S. Lavallee, "A New System for Computer Assisted Neurosurgery," *Proceedings of the Annual International Conference of the IEEE Engineering and Biology Society*, vol. 3, pp. 926-927, 1989.

S. Lavallee, J. Troccaz, P. Sautot, B. Mazier, P. Cinquin, P. Merloz, and J. P. Chirossel, "Computer-Assisted Spinal Surgery Using Anatomy-Based Registration," in *Computer-Integrated Surgery: Technology and Clinical Applications*, R. H. Taylor, S. Lavallee, G. C. Burdea, and R. Mosges, Eds. Cambridge, Massachusetts: The MIT Press, 1996, pp. 425-449.

J. T. Lewis, "Ultrasonic detection of subcutaneous fiducial markers for interactive, image-guided neurosurgery," Ph.D. dissertation, Vanderbilt University, Nashville, TN, 1992.

J. T. Lewis, R. L. Galloway, Jr., and S. Schreiner, "An Ultrasonic Approach to Localization of Fiducial Markers for Interactive, Image-Guided Neurosurgery--Part I: Principles," *IEEE Transactions on Biomedical Engineering*, vol. 45, pp. 620-630, 1998.

J. T. Lewis and R. L. Galloway, "A-mode ultrasonic detection of subcutaneous fiducial markers for image-physical space registration," *Proceedings of the Annual International Conference of the IEEE Engineering in Medicine and Biology Society*, vol.3, pp1061-1062, 1992.

J. T. Lewis and R. L. Galloway, "Three-dimensional localization of implanted fiducial markers for interactive, image-guided surgery," *Proceedings of the Annual International Conference of the IEEE Engineering in Medicine and Biology Society*, pp. 952-953, 1993.

J. B. A. Maintz and M. A. Viergever, "A survey of medical image registration", *Medical Image Analysis*, vol. 2, pp1-36, 1998.

V. R. Mandava, J. M. Fitzpatrick, C. R. Maurer, R. J. Maciunas, and G. S. Allen, "Registration of multimodal volume head images via attached fiducials," in *Proc. SPIE Medical Imaging V*I, vol. 1652, Feb. 1992.

C. R. Maurer, Jr., G. B. Aboutanos, B. M. Dawant, R. J. Maciunas, and J. M. Fitzpatrick, "Registration of 3-D Images Using Weighted Geometrical Features," *IEEE Transactions on Medical Imaging*, vol. 15, pp. 836-849, 1996.

C. R. Maurer, Jr., J. M. Fitzpatrick, M. Y. Wang, R. L. Galloway, Jr., R. J. Maciunas, and G. S. Allen, "Registration of Head Volume Images Using Implantable Fiducial Markers", *IEEE Transactions on Medical Imaging*, vol. 16, pp 447-462, 1997.

C. R. Maurer, J. M. Fitzpatrick, M. Y. Wang, R. L. Galloway, R. J. Maciunas, and G. S. Allen, "Registration of head volume images using implantable fiducial markers," in *Image Processin*g, K. M. Hanson, Ed., SPIE 3034, pp. 561–579, 1997.

C. R. Maurer, Jr., J. M. Fitzpatrick, M. Y. Wang, and R. J. Maciunas, "Estimation of Localization Accuracy for Markers in Multimodal Volume Images," *Proceedings of the 15th Annual International Conference of the IEEE Engineering in Medicine and Biology Society*, pp. 124-125, 1993.

C. R. Maurer, Jr., R. P. Gaston, D. L. G. Hill, M. J. Gleeson, M. G. Taylor, M. R. Fenlon, P. J. Edwards and D. J. Hawkes, "AcouStick: A Tracked A-Mode Ultrasonography System for Registration in Image-Guided Surgery", *MICCAI 1999*, pp. 953-962, 1999.

C. R. Maurer, Jr., D. L. G. Hill, A. J. Martin, H. Liu, M. McCue, D. Rueckert, D. Lloret, W. A. Hall, R. E. Maxwell, D. J. Hawkes, and C. L. Truwit, "Investigation of Intraoperative Brain Deformation Using a 1.5-T Interventional MR System: Preliminary Results", *IEEE Transactions on Medical Imaging*, vol. 17, pp. 817-825, 1998.

R. Mosges and G. Schlondorff, "A new imaging method for intraoperative therapy control in skull-base surgery," *Neurosurg. Rev*., vol. 11, pp. 245–247, 1988.

J. Oikarinen, J. Alakuijala, Y. Louhialmi, S. Sallinie, H. Helminen, and J. Koivukangas, "The Oulu Neuronavigator System: Intraoperative Ultrasonography in the Verification of Neurosurgical Localization and Visualization," in *Interactive Image-Guided Neurosurgery*, R. J. Maciunas, Ed.: AANS, 1993, pp. 233-246.

OPTOTRAK®. Rigmaker Guide, Northern Digital Inc., Waterloo, Ont., Canada, 1994.

C. Pelizzari, D. N. Levin, G. T. C. Chen, and C. T. Chen, "Image Registration Based on Anatomic Surface Matching," in *Interactive Image-Guided Neurosurgery*, R. J. Maciunas, Ed.: AANS, 1993, pp. 47-62.

T. M. Peters, J. A. Clark, G. B. Pike, and C. J. Henri, "Stereotactic neurosurgery planning on a PC-based workstation," *Journal of Digital Imaging*, vol. 2, 1991.

P. K. Pillay, "Image-guided stereotactic neurosurgery with the multicoordinate manipulator microscope," *Surgical Neurology*, vol. 47, pp. 171-177, 1997.

B. P. Poncelet, V. J. Wedeen, R. M. Weisskoff, and M. S. Cohen, "Brain parenchyma motion: Measurement with cine echoplanar MR imaging," *Radiology*, vol. 185, pp. 645–651, 1992.

M. J. D. Powell, "An efficient method for finding the minimum of a function of several variables without calculating derivatives," *The Computer Journal*, vol. 7, pp. 155-162, 1964.

W. H. Press, B. P. Flannery, S. A. Teukolsky, and W. T. Vetterling, *Numerical Recipes in C: The Art of Scientific Computing*, Second Edition ed. New York, NY: Cambridge University Press, 1992.

Quantum Inspection and Testing Limited, "Calibration Certificate," , Burlington, Ontario, Canada 1994.

D. W. Roberts, E. M. Friets, J. W. Strohbehn, and T. Nakajima, "The sonic digitizing microscope," in *Interactive Image-Guided Neurosurgery*, R. J. Maciunas, Ed.: AANS, 1993, pp. 105-111.

D. W. Roberts, J. W. Strohbehn, J. F. Hatch, W. Murray, and H. Kettenberger, “A frameless stereotaxic integration of computerized tomographic imaging and the operating microscope,” *Journal of Neurosurgery*, vol. 65, pp. 545-549, 1986.

G. Schlondorff, R. Moesges, and L. Klimek, “An articulated Localizing Arm for Otolaryngology,” in *Interactive Image-Guided Neurosurgery*, R. J. Maciunas, Ed.: AANS, 1993, pp. 149-157.

P. H. Schönemann, “A generalized solution of the orthogonal procrustes problem,” *Psychometrika*, vol. 31, pp. 1–10, 1966.

S. Schreiner, J. H. Anderson, R. H. Taylor, J. Funda, A. Bzostek, and A. C. Barnes, “A System for Percutaneous Delivery of Treatment with a Fluoroscopically-Guided Robot,” presented at CVRMed-MRCAS, Grenoble, France, 1997.

S. Schreiner, R. L. Galloway, Jr., W. A. Bass, and D. M. Muratore "An Ultrasonic Approach to Localization of Fiducial Markers for Interactive, Image-Guided Neurosurgery--Part II: Implementation and Automation," *IEEE Transactions on Biomedical Engineering*, vol. 45, pp. 631-641, 1998.

R. L. Siddon, “Prism representation: a 3D ray-tracing algorithm for radiotherapy applications,” *Physics in Medicine and Biology*, vol. 30, pp. 817-824, 1985.

D. A. Simon, “Fast and Accurate Shape-Based Registration,” in *Robotics*. Pittsburgh, Pennslyvania: Carnegie Mellon University, 1996, pp. 196.

D. A. Simon, B. Jaramaz, M. Blackwell, F. Morgan, A. M. DiGioia, E. Kischell, B. Colgan, and T. Kanade, “Development and Validation of a Navigational Guidance System for Acetabular Implant Placement,” presented at CVRMed-MRCAS, Grenoble, France, 1997.

T. K. Sinha, D. M. Cash, R. J. Weil, R. L. Galloway, Jr., and M. I. Miga, “Cortical Surface Registration Using Texture Mapped Point Clouds and Mutual Information”, *MICCAI 2002*, pp. 533-540, 2002.

E. P. Sipos, S. A. Tebo, S. J. Zinreich, D. M. Long, H. Brem, “In vivo accuracy testing and clinical experience with the ISG Viewing Wand,” Neurosurgery, vol. 39, pp. 194-204, 1996.

Specification sheet for Acquasonic Ultrasonic Transmission Gel, Parker Laboratories, Orange, NJ.

C. Studholme, D. L. G. Hill, and D. J. Hawkes, "An overlap invariant entropy measure of 3d medical image alignment," *Pattern Recognition*, vol. 32, pp. 71-86, 1999.

T. Takizawa, S. Soto, A. Sanou, and Y. Murakami, “Frameless isocentric stereotactic laser beam guide for image-directed microsurgery,” *Acta Neurochirurgica*, vol. 125, pp. 177-180, 1993.

S. Umeyama, “Least-Squares Estimation of Transformation Parameters Between Two Point Patterns,” *IEEE Transactions on Pattern Analysis and Machine Intelligence*, vol. 13, pp. 376-380, 1991.

A. Wagner, O. Ploder, G. Enislidis, M. Truppe, and R. Ewers, “Image-guided surgery,” *International Journal of Oral & Maxillofacial Surgery*, vol. 25, pp. 147-151, 1996.

M. Y. Wang, C. R. Maurer, Jr., J. M. Fitzpatrick, and R. J. Maciunas, “An Automatic Technique for Finding and Localizing Externally Attached Markers in CT and MR Volume Images of the Head,” *IEEE Transactions on Biomedical Engineering*, vol. 43, pp. 627-637, 1996.

E. Watanabe, “The neuronavigator: A potentiometer-based localizing arm system,” in *Interactive Image-Guided Neurosurgery*, R. J. Maciunas, Ed.: AANS, 1993, pp. 135-147.

E. Wantanabe, J. Mayanagi, Y. Kosugi, S. Manaka, and K. Takakura, “Open surgery by the neuronavigator, a stereotactic, articulated, sensitive arm,” *Neurosurgery*, vol. 28, pp. 792–799, 1991.

E. Watanabe, T. Watanabe, S. Manaka, Y. Mayanagi, and K. Takakura, “Three dimensional digitizer (neuronavigator): new equipment for computed tomography-guided stereotaxic surgery,” *Surgical Neurology*, vol. 27, pp. 543-547, 1987.

J. West, J. M. Fitzpatrick, B. M. Dawant, Kessler, R. Maciunas, Ayache, Pennec, Barillot, Lemoine, Collignon, V. D. Elsen, Hemler, Napel, Sumanaweera, Evans, Fahey, Harkness, Hill, Kapouleas, Maintz, Noz, Rusinek, Pelizzari, Robb, and Woods, “Comparison and evaluation of retrospective intermodality,” in *Proc. SPIE Medical Imaging 199*6, vol. 2710, Feb. 1996.